MARCKO-Dampfturbine - Erarbeitung und langzeitige Absicherung von Auslegungsdaten für 600 bis 625/700°C Dampfturbinen

Teilvorhaben: Mikrostruktur

Abschlussbericht

W. Blum, H. Chilukuru

21. März 2006

Projektnummer:	0327055A
Laufzeit:	01.09.2002 bis 31.08.2005
Durchführung:	Friedrich-Alexander-Universität Erlangen-Nürnberg Institut für Werkstoffwissenschaften I Martensstr. 5, 91058, Erlangen
Projektleitung:	Prof. Dr.-Ing. Wolfgang Blum

Inhaltsverzeichnis

1 Kurzdarstellung

1.1 Aufgabenstellung

In pursuit of materials that sustain high temperatures in steam power plants seven alloys (Table. 1) were designed for this project. This project is a continuation of MARCKO DT1/2-Projekt (project period 01.06.1997 - 31.03.2002). Tungsten based steels 1A and 2A, Tungsten free steels 3A and 4A were developed for use at 600 °C, Boron and Cobalt based steels 5A and 6A were developed for use at 625 °C and for future use at 700 °C a Nickel based Alloy 617 was developed.

Focus of the present part of the cooperative project is to understand the evolution of microstructure in these alloys. Deformation resistance in the 9-12 % Cr steels depends on dislocation and precipitate strengthening, whereas the Nickel based Alloy 617 (7A) is mainly dependent on dislocation and solid solution strengthening. Dislocation and particle structure evolutions were characterized with the aid of TEM. Results were used to predict, understand and model (MIKORA) the deformation behavior of these alloys. Thermodynamic databases can be updated with these experimental results.

1.2 Voraussetzungen des Vorhabens

In den letzten 20 Jahren wurden in internationaler Zusammenarbeit ferritisch-martensitische 9-12 % CrMo(W)VNbN-Stähle entwickelt, mit denen fossil befeuerte Dampfkraftwerke mit 600 °C Dampfeintrittstemperatur und bei gleichzeitiger Steigerung des Dampfdrucks auf 300 bar realisierbar sind. Um das volle Potential dieser Werkstoffe ausnutzen zu können, ist die Kenntnis der langzeitigen Gebrauchseigenschaften unumgänglich. Mit dem Ziel die werkstofflichen Voraussetzungen für das CO2-arme Kohlekraftwerk zu schaffen, wurde das BMBF-/BMWA-Forschungsprogramm MARCKO (Materialrealisierung CO2-armes Kohlekraftwerk) gestartet. In einem vorangegangenen Forschungsvorhaben, das ein Teilprojekt des Verbundvorhabens Dampfturbine (DT1/2) des MARCKO-Programms ist, wurden ferritisch-martensitische 600 °C-Stähle vom Typ (G)X10CrMoWVNbN10-1-1 intensiv untersucht und deren Eigenschaften unter betriebsnahen Beanspruchungen ermittelt und beschrieben. Neue Entwicklungen in der Kraftwerkstechnik sehen eine weitere deutliche Anhebung des Wirkungsgrads von Dampfkraftwerken auf über 55% mit der Erhöhung der Frischdampftemperatur auf 700 °C vor. Dazu sind neue verbesserte Werkstoffe sowohl von martensitisch/ferritischen Stahlsorten als auch von Nickelbasislegierungen erforderlich.

Das Vorhaben greift daher die neuen Werkstoffentwicklungen aus den COST-Vorhaben auf, in denen Kobalt-legierte martensitische Cr-Stähle für Einsatztemperaturen bis 625 °C entwickelt wurden. Für Betriebstemperaturen von 700 °C ist der Einsatz von Nickelbasislegierungen erforderlich, die für den Einsatz in massiven Dampfurbinenkomponenten optimiert werden müssen.

Neben den COST-Forschungsprogrammen wurden eine Reihe weiterer Forschungsvorhaben wie Z. B. MARCKO 700 und Thermie AD700 gestartet (siehe Fig. 1), in denen Werkstoffentwicklungen und -qualifizierungen für den Temperatureinsatzbereich 600 bis 700 °C durchgeführt werden.

1.3 Planung und Ablauf

Personal cost of this project has been utilized at 50 % BAT IIA for the investigations to be carried out through out the project period. Scientific coworkers H. Chilukuru, X. H. Zeng, and guest scientists from Babha Atomic Research Centre, Mumbai (India), J. S. Dubey and Dr. S. Wadekar were involved in this project.

Research plan was to investigate 12 conditions with in the resolution of TEM and use the results in MIKORA. In total $\approx$ 20 conditions were investigated in the project, including initial, cycled and crept conditions. The extended investigations on cyclically deformed specimens provided greater insight into subgrain hardening and creep-fatigue interaction. Additional creep experiments, ageing treatments, modeling of cyclic subgrain evolution and re-evaluation of the volume fraction of precipitates were carried out apart from the planned investigations of dislocation and precipitated structure.

1.4 Wissenschaftlicher Stand des Wissens

Research on 9-12 % Cr steels is carried out primarily in Europe, Japan and USA. Microstructure in these steels with respect to the dislocation structure and the particle structure should be evaluated differently. The evolution of dislocation structure is primarily dependent on stress and strain, whereas the particle structure evolution is primarily dependent on temperature and time. The evolution of the complete microstructure must be taken into account to understand deterioration in creep resistance. Frequently in 9-12 % Cr steels, improved short-term creep properties do not persist in long-term service [1, 2, 3, 4, 5, 6].

An overview of microstructural development in tempered martensite steels with focus on the differences in stability of different precipitate phases, their consequences on creep resistance and measures to avoid instable phases leading to drastic breakdown of creep resistance is given in [7] (see Appendix F).

In the initial state depending upon the heat treatment $M_{23}C_6$, M_2X and MX (M: metallic element, X: C. N) types of precipitates are found. In the course of deformation at creep temperature Laves phase and Z-phase are precipitated. $M_{23}C_6$ and Laves phase stabilize the subgrain boundaries by precipitating on them. M_2X and MX contribute significantly to the deformation resistance by hindering the motion of free dislocations inside the subgrain interior. M_2X is considered to be less stable than MX. Z-phase is mainly precipitated on the prior austenite grain boundaries (PAGBs), Z-phase precipitation degrades creep resistance by dissolution of MX and M_2X type of precipitates [1, 2, 3, 4, 5, 6, 8]. The type of phases

precipitated, their coarsening and dissolution depends on the alloying elements and the heat treatment [5].

Nickel based super alloy (NiCr22Co12Mo9) has good high temperature creep properties. Its hardening contributions mainly come from the solid solution and dislocation structure. Subgrain structure in this alloy forms in the course of deformation.

1.5 Zusammenarbeit mit anderen Stellen

Work in this project has been carried out in cooperation with the project partners and from other institutes. The specimens investigated in this project along with the heat treatments and mechanical test data were provided by the project partner IfW Darmstadt. A visit to the partner MPA Stuttgart was arranged to discuss the microstructural investigations. Suggestions from microstructural aspect have been provided to IWM Freiberg where they were used to explain the racheting effect. Industry and institute partners were updated on microstructural findings and interpretations of the mechanical behavior of the alloys regularly in the half yearly meetings involving discussions of the results and exchange of views on future tasks. Points of uncertainty were rechecked and updated to the partners.

As part of Indo-German scientific cooperation, guest scientists from Babha Atomic Research Centre, Mumbai (India), J. S. Dubey and Dr. S. Wadekar were involved in this project. Insitu transmission electron microscopic experiments were carried out in cooperation with Prof. U. Messerschmidt, Max-Planck-Institut für Mikrostrukturphysik, Halle.

2 Eingehende Darstellung

2.1 Untersucht Werkstoffe

Following are the alloys investigated in this project (Table. 1).

Alloys		**1A**	**2A**	**3A**	**4A**	**5A**	**6A**	**7A**
C		0.12	0.13	0.14	0.115	0.13	0.11	0.06
Si		0.10	0.29	0.8	0.41	0.05	0.29	0.075
Mn		0.42	0.82	0.55	0.54	0.82	0.87	0.03
Ni		0.76	0.52	0.56	0.12	0.16	0.22	rest
Cr		10.7	9.51	9.99	9.04	9.32	9.13	22.9
Mo		1.07	1.02	1.40	0.86	1.47	1.46	8.7
W		1.04	1.02					< 0.05
Co						0.96	0.99	12.8
V		0.16	0.19	0.17	0.20	0.20	0.19	
Nb		0.05	0.059	0.059	0.10	0.05	0.061	0.08
B			0.0005			0.0085	0.0117	
N		0.056	0.041	0.041	0.058	0.019	0.021	0.0032
Al					0.021			1.03
Ti								0.53
Fe								0.94
Austenitisation	$T/\,°\mathrm{C}$	1050	1070	1070	1050	1050	1100	1100
	$t/\,\mathrm{h}$	7	12	20	10	10	9	5
	cooling	oil	air	oil	blower	water	air	water
Tempering 1	$T/\,°\mathrm{C}$	570	730	570	740	570	740	
	$t/\,\mathrm{h}$	10.25	10	27	14	22	10	
Tempering 2	$T/\,°\mathrm{C}$	690	730	675	730	700	730	
	$t/\,\mathrm{h}$	10	10	25	10	22	12	
Tempering 3	$T/\,°\mathrm{C}$			645	720		730	
	$t/\,\mathrm{h}$			13	8		12	
d_{aust} / μ**m**		57	1107	362	62	329	523	95
ASTM No.		5	-3	0	5	0	-1	4

Tabelle 1: Alloys investigated in the project, their compositions in mass-%, their heat treatments and grain sizes

2.2 Ergebnisse für Cr-Stähle (Werkstoffe 1 - 6)

2.2.1 Influence of prior austenite grain size

The prior austenite grain size d_{aust} in 9-12 % Cr steels, depends on the austenitisation treatment. Table. 1, shows that d_{aust} increases with increase in austenitisation temperature, time and decrease of cooling rate. Differences in d_{aust} do not affect the long-term deformation behavior significantly. For instance, d_{aust} of 2A is larger than that of 1A by a factor 20, but the long-term deformation behavior of 2A is better than 1A (Fig. 10). This makes clear that long-term deformation behavior is significantly dependent on strengthening contributions from other microstructural parameters such as dislocations, subgrains and precipitates.

2.2.2 Creep-fatigue interaction

Cyclically deformed specimens of 1A and 2A were investigated. The results are described in [9] (Section A), [10] (Section B), and [11] (Section D) and are briefly addressed here. Cyclic deformation was performed by IfW Darmstadt under conditions of stress and elevated temperature which are relevant for power stations. It leads to significant subgrain coarsening (by a factor up to 5). The presence of hold periods with stress relaxation within the cycles enhances the coarsening of subgrains. The evolution of subgrain size w during cycling was successfully calculated by extending the established expression for the rate of change of subgrain size with unidirectional strain in creep to the case of cyclic straining, by replacing the inelastic creep strain by the cumulative inelastic cyclic strain.

The coarsening of the subgrain structure due to cyclic deformation at elevated temperature is consistent with the drastic reduction of creep resistance observed after cyclic deformation, confirming the idea of strengthening by subgrains and explaining the so-called creep-fatigue interaction, i.e. the strong reduction in creep life due to prior or concurrent cyclic deformation.

2.2.3 Dislocation structure

Dislocation structure evolution and its effects on the deformation behavior are reported in [9] (Section A), [10] (Section B) and [11] (Section D). Fig. 2 shows typical TEM micrographs of the initial structure after heat treatment. One sees that subgrain structures are present in all cases. The effect of quantitative differences in the dislocation structure on the creep resistance in the investigated alloys is addressed in section 2.2.7 below.

2.2.4 Precipitates

An essential contribution to the deformation resistance comes from particle hardening. Particle type, size and volume fraction have been quantified and are provided in Section G. The

initial state may not necessarily provide an insight into the mechanical stability of the alloy, which is more dependent on the coarsening of phases, formation of new and dissolution of existing phases in the course of deformation.

The method of extracting the precipitates from the matrix has been found successful for analyzing the precipitate structure [12, 13, 14]. Besides the precipitate size, the volume fraction f_{p} of precipitates is a most important parameter, not only for estimating precipitation hardening, but also as input for thermodynamic data bases.

In the past an empirical formula has been used to provide a rough estimate of f_{p} has been used. As described in Section E, this formula needs to be modified on the basis of our scanning electron microscopic (FEG-SEM) investigations of the etched steel surface. In all cases, where the particle structure found in the replica resembles the structure seen by SEM observation of the (etched) steel surface (Fig. 3), one has to assume that the loose precipitate particles have been removed from the surface. In this case the information depth, characterizing the sampling volume, is well approximated by the size of the precipitates (see formula (1). This means that the information depth is different for large (like $M_{23}C_6$) and small (like MX) precipitates. Compared to the previous data for the volume fraction, the volume fractions now become higher for small precipitates and somewhat lower for large precipitates. For each precipitate phase k the volume fraction $f_{\mathrm{p,k}}$ is estimated as

$$f_{\mathrm{p,k}} = \frac{N_{\mathrm{p,k}} \cdot V_{\mathrm{p,k}}}{A \cdot d_{\mathrm{p,k}}} \tag{1}$$

$N_{\mathrm{p,k}}$: number of phase k precipitates, $V_{\mathrm{p,k}}$: mean volume of phase k precipitates, A: investigated area, $d_{\mathrm{p,k}}$: mean particle size of precipitate phase k.

In 9-12 % Cr steels, M_2X and MX are important contributors to deformation resistance as they precipitate in large numbers within the subgrain interior restricting the dislocation motion there (see Fig. 9). Z-phase has been proposed [15, 5, 16, 6, 17] to exert a deleterious effect by dissolution of VX and M_2X being thermodynamically less stable than Z-phase. This leads to loss of subgrain strengthening in the subgrain interior which is not compensated by hardening by Z-phase, because Z-phase precipitate on the subgrain boundaries (Fig. 4).

In their initial state 1A and 3A have M_2X as a result of tempering below 700 °C in agreement with [5] findings. In the course of deformation Z-phase precipitation was observed in these alloys. Even after Z-phase precipitation, a decrease in M_2X volume fraction f_{p}, indicating dissolution was not observed (Fig. 5). In this case Z-phase is not accountable for the degradation in deformation resistance as it does not precipitate at the expense of other phases. Fig. 5 shows that M_2X coarsens rapidly, which is by a factor 10 faster than VX.

Therefore there must be another reason for degradation. It lies in M_2X. Fig. 5 shows that M_2X coarsens rapidly, by a factor 10 faster than VX.

Large M_2X particles were found especially on the subgrain boundaries. These particles were confirmed by EDAX chemical analysis and the crystal structure. The chemical composition of M_2X is distinctly different from that of Z-phase; this excludes the possibility of mixup. The

chemical composition is independent of the particle size (Fig. 6), excluding the possibility of phase change with the increase of particle size. The crystal structure was identified to be hexagonal and the lattice constant agrees well with literature data for M_2X [18].

Why does M_2X coarsen rapidly? Investigations on the shape of M_2X might provide the answer. In the initial state (Fig. 7), M_2X are small, coherent, needle-shaped particles, in the course of deformation they are plate shaped particles which may be semi-coherent, and finally large rod shaped particle are found on the subgrain boundaries which are incoherent. This loss in coherency increases the interfacial energy and therefore increases the coarsening rate.

Coarsening of different precipitates has different consequences on the deformation resistance. For instance, coarsening of $M_{23}C_6$ will destabilize the subgrain boundaries (lower resistance against migration). But, coarsened M_2X particles which precipitate at subgrain boundaries at the expense of fine M_2X precipitates in the subgrain interior (Fig. 8) reduce the precipitation hardening of the subgrain interior and thereby deteriorate the deformation resistance. MIKORA [19] predicts a factor of 10 increase in the minimum creep rate with the loss of precipitation hardening in the subgrain interior.

Fig. 10 shows the creep rupture curves for 1A and 2A. 1A has better creep resistance in the initial period, but the creep resistance degrades rapidly in 1A in comparison to 2A. Z-phase was detected in 1A, but the major cause for the degradation of creep resistance is rapid coarsening of M_2X.

If the phase M_2X is responsible for enhanced degradation of creep resistance, the question arises why Z phase is usually found under conditions of anomalously fast degradation of creep resistance. The answer may lie in a correlation between M_2X and Z. Large, incoherent M_2X particles at the subgrain boundaries with high interfacial energy, large interface and high V-content constitute favorable nucleation sites for Z-phase. Thus M_2X may not only cause the anomalous degradation of creep resistance, but also cause nucleation of stable Z at the subgrain boundaries which will then enhance the degradation because Z phase also leads to dissolution of precipitation hardening in the subgrain interior by V-containing phases. Thus M_2X may be a clue in the understanding of enhanced degradation of the creep resistance of 9-12%Cr-steels.

The technological consequence of these considerations is that the thermal treatment of steels designed for long term use at high temperature should be such as to avoid precipitation of V in the form of M_2X. This means in particular that low temper temperatures must be avoided.

2.2.5 In situ-observations

In situ TEM-experiments were carried out with the equipment and support kindly provided by Prof. Messerschmidt at MPI für Mikrostrukturforschung, Halle. To our knowledge this is the first time that in situ investigations were done on 9-12 % Cr steels. Microstructural changes taking place during deformation at 650 °C in 2A were investigated. These investigation provide evidence for strong interaction between dislocations and particles given by the distinct

bowing of dislocations between particles in Fig. 9 during deformation.

There is also evidence of glide of dislocations through subgrain boundaries evidenced by their bowing and indication of dissolution of subgrain boundaries at places where the density of particles deposited at the boundaries is low (Fig. 9).

These in-situ findings support the basic assumptions in the model MIKORA.

2.2.6 Microstructural modeling with MIKORA

Our previous efforts to provide a model of creep based on microstructure (dislocations and precipitates) have been continued in this project [19] (Section C).

The model MIKORA has meanwhile been accepted by Ågren and coworkers [20] as a reasonable basis for modeling creep in conjunction with a thermodynamic model of the evolution of the phase structure. The detailed equations of Mikora are given in the Section H. The basics of the model are:

- The evolution of the dislocation structure on the basis of the rates by which the steady state values (subscript ∞) of the characteristic dislocation spacings (spacing of free dislocations (δ), of subgrain boundaries (w), and of dislocations within the subgrain boundaries (s) are approached. δ_∞ and w_∞ are unique functions of applied stress σ normalized by shear modulus G. This appears to be a reasonable approximation which greatly simplifies the model. s is taken to be constant.
- The influence of subgrain boundaries on the creep rate is modeled by the composite approach, assuming the subgrain boundaries to be relatively hard due to high local densities of dislocations and precipitates.
- The evolution of the precipitates structure leads to continuous shift of the steady state creep rate as the stress components for precipitation hardening change.

The effect of coarsening/dissolution of small precipitates in the subgrain interior could well be modelled reference to Fig. 5 in paper [19] (Section C). This paper also shows a good agreement between the modeled curves and the experimental data over a large range of stresses and temperatures.

2.2.7 Microstructural interpretation of the creep-rupture behavior

This section provides the microstructural interpretation for the experimental creep rupture curves from IfW Darmstadt displayed in Figs. 11 and 12.

The W-based steels 1A, 2A and W-free 3A, 4A are designed for operation at 600°C. The forged steels 1A and 3A show better initial creep resistance due to their small initial subgrain

size w_0 and numerous fine M_2X-particles in comparison to larger w_0 and MX-particles in the cast steels 2A and 4A. As evident from the creep rupture curves, the deterioration of creep resistance with increasing rupture time is faster in 1A and 3A in comparison to 2A. This is primarily due to the relatively rapid coarsening of M_2X (section 2.2.4). According to the Ostwald ripening law, the coarsening of precipitates occurs at a certain constant rate of increase of precipitate volume with time. This coarsening becomes relevant only at times where the increase of volume is significant relative to the initial volume of the precipitates. This time decreases when the initial size of precipitates $d_{\mathrm{p},0}$ is small and the coarsening rate is high. Smaller $d_{\mathrm{p},0}$ and higher coarsening rate of M_2X in comparison to MX explain why the creep resistance of 1A and 3A degrades faster than that of 2A and 4A. Consistent with the thermal activation of coarsening the degradation by coarsening of M_2X sets in at lower times for higher temperature. This explains why the point of intersection of the curves for 1A (with M_2X) and 2A (with MX) shifts to smaller times with increasing temperature.

The initial subgrain sizes in 1A and 3A are similar giving no reason for a difference in creep rupture behavior. Yet the creep rupture strength of the W-free 3A is better than that of W-based 1A. Laves phase in the W-bearing steels is expected to stabilize the subgrain boundaries and increase the creep life of 1A. Obviously, this effect is not dominant here, but is masked by other changes in the microstructure probably related to carbonitride precipitates.

In the case of the cast steels the expectation of a positive effect of W is fulfilled. However, the W-free steel 4A shows abnormal fracture behavior with low fracture strain. E.g. the investigated 4A specimen crept at 90 MPa at 600 °C has only 4.04 % fracture strain whereas a 3A specimen crept at 125 MPa at 600 °C has 17.5 % fracture strain. This embrittlement may have to do with grain boundaries, e.g. in relation with localized strain at grain boundaries due to locally coarsened microstructure or to impurity segregation at the boundaries. However, there are no data to clarify this view.

The Co and B based 5A and 6A were developed for operation at 625 °C. Preliminary creep test data show that 5A is the most promising of the investigated steels. In the initial state 5A has the largest mean subgrain size, but the highest density of free dislocations (see Appendix Fig. 19) as a result of water quenching after austenitisation. Particle structure investigations showed $M_{23}C_6$ and small (V,Nb)X type of precipitates in both 5A and 6A. No long-term specimens of 5A and 6A were available to carry out meaningful investigations.

2.3 Ergebnisse für Ni-Basislegierung (Werkstoff 7A - Alloy 617)

7A has a twinned microstructure with an initial dislocation spacing of 200 nm with ≈ 1 μm large $M_{23}C_6$ on the grain boundaries (Fig. 13). A crept specimen (Fig. 14) at 650 °C, 380 MPa, 590 h shows a high dislocation density (not quantified (see Fig. 21. No substructure formation was observed. Large $M_{23}C_6$ particles were present on the grain boundaries. Their chemical composition Fig. 15 agrees with that found in the literature. No precipitates were found in the grain boundary interior. Long-term specimens were not available in order to investigate the evolution of the microstructure.

2.4 Nutzen und Verwertbarkeit

Die (elektronen-) mikroskospische Untersuchung von 20 Ausgangs- und beanspruchten Zuständen der Werkstoffe des Vorhabens in diesem Teilvorhaben hat wesentliche Fortschritte im Verständnis des Zusammenhangs zwischen Mikrostruktur und Gebrauchseigenschaften erbracht:

- Die sogenannte Kriech-Ermüdungswechselwirkung der Cr-Stähle, das heißt die Beeinträchtigung des Kriechwiderstandes durch vorangehende oder überlagerte zyklische Beanspruchung konnte auf die Vergröberung der Subkornstruktur zurückgeführt werden. Es gelang, diese durch einen einheitlichen Ausdruck zu beschreiben. Dieser kann in Zukunft benutzt werden, um die Entwicklung der Subkorngröße bei kombinierter Kriech-Ermüdungs-Beanspruchung numerisch (durch Integration der Änderungsrate der Subkorngröße) zu berechnen. Damit ist es möglich, die Wirkung unterschiedlicher Kombinationen von Kriech- und Ermüdungsbeanspruchung auf die Lebensdauer der Werkstoffe abzuschätzen.

- Der erhebliche Unterschied in der Vergröberungsrate der beiden V-haltigen, das Subkorninnere härtenden Ausscheidungen MX und M_2X in den Stählen wurde quantitativ dargestellt. Dadurch, dass die metastabilere Phase M_2X zwar feiner ausscheidet, aber rascher vergröbert, ergibt sich, dass M_2X hinsichtlich des Kriechwiderstandes einen Anfangsvorteil erbringt, der mit zunehmender Temperatur zunehmend rascher aufgebraucht wird und sich bei langen Zeiten in einen Nachteil umwandelt. Die Ergebnisse dieses Vorhabens lassen vermuten, dass M_2X auch die Keimbildung von Z-Phase befördert, was die Degradation des Kriechwiderstandes weiter reduziert. Die Konsequenz ist, dass Ausscheidung von V in Form von M_2X vermieden werden sollte. Das kann durch Änderung der Wärmebehandlung (Vermeiden niedriger Temperatemperaturen) geschehen.

Soweit der Kriechwiderstand durch die Volumen-Mittelwerte der mikrostrukturellen Parameter bestimmt wird, kann er durch das Modell MIKORA im Prinzip abgebildet werden. MIKORA arbeitet wie andere phänomenologischen Modelle numerisch mit Integration von Ratengleichungen, unterscheidet sich von diesen aber durch die Nutzung mikrostruktureller Parameter. Wenngleich die Modellentwicklung nicht Hauptgegenstand dieses Vorhabens war, konnte gezeigt werden, dass das Modell nach begrenzter Anpassung an experimentelle Daten in der Lage ist, das Verhalten der Kriechrate mit Dehnung bzw. Zeit qualitativ richtig nachzubilden. Das gilt insbesondere für den Verlust an Kriechfestigkeit durch Verschwinden relativ feiner Ausscheidungen im Subkorninneren. Das Modell MIKORA ist für weitere Verwertung und Verbesserung verfügbar.

Das Teilvorhaben Mikrostruktur trägt durch die Verbesserung des Werlstoffverständnisses zu den Zielen des Gesamtvorhabens bei, die langzeitigen zeit- und temperaturabhängige Kennwerte der wolframhaltigen und wolframfreien 600 °C-Stähle für moderne Dampfturbinen langzeitig abzusichern und anwendungsnah zu beschreiben, die Werkstoffausnutzung und die Effizienz moderner fossiler Dampfkraftwerke durch besserer Lebensdauervorhersagen zu

verbessern sowie einen Beitrag zur Auslegung und Betrieb von Turbinenbauteilen der neuen Generation hocheffizienter Kraftwerke zu leisten. Auf diese Weise wird ein Knowhow- und Wettbewerbsvorteil der Industriepartner gegenüber der internationalen Konkurrenz erzielt. Im Hinblick auf die angestrebte Reduzierung der Schadstoffemissionen bei der Energieerzeugung tragen die Ergebnisse dieses Vorhabens zur Bereitstellung zukünftiger hocheffizienter und ressourcenschonender Kraftwerke bei. Dadurch lassen sich auf Dauer Wettbewerbsvorteile für den gesamten Industriestandort Deutschland ableiten. Auch die klein- und mittelständische Industrie profitiert sehr stark von den Ergebnissen, da bei der Herstellung dieser meist großtechnischen Anlagen auch viele kleine und mittlere Unternehmen beteiligt sind. Sie gewinnen diese auf kostensparende Weise ebenfalls einen Leistungs- und Wettbewerbsvorsprung.

2.5 Während des Vorhabens bekannt gewordene Ergebnisse anderer Stellen

Low carbon, 9-12 % Cr steels were developed by Japanese researchers to avoid $M_{23}C_6$. These steels showed good initial creep properties. Boron based steels showed good creep resistance. Balance between boron and nitrogen is necessary to prevent boron precipitating as large BN particles. The model MIKORA has meanwhile been accepted by Ågren and his coworkers [20] as a reasonable basis for modeling creep in conjunction with a thermodynamic model of the evolution of the phase structure. The thermodynamic software programmes are being upgraded to predict the precipitation behavior especially with regard to the Z-phase [16].

2.6 Erfolgte und geplante Veröffentlichungen der Ergebnisse

Aus dem Vorhaben resultierten sechs Publikationen, die Teil dieses Berichts sind: [9] (Abschnitt A), [10] (Abschnitt B), [19] (Abschnitt C), [11] (Abschnitt D), [13] (Abschnitt E), [7] (Abschnitt F)

In Planung: H. Chilukuru. *Hardening contributions in 9-12% Cr steels* (Dissertation Universität Erlangen-Nürnberg)

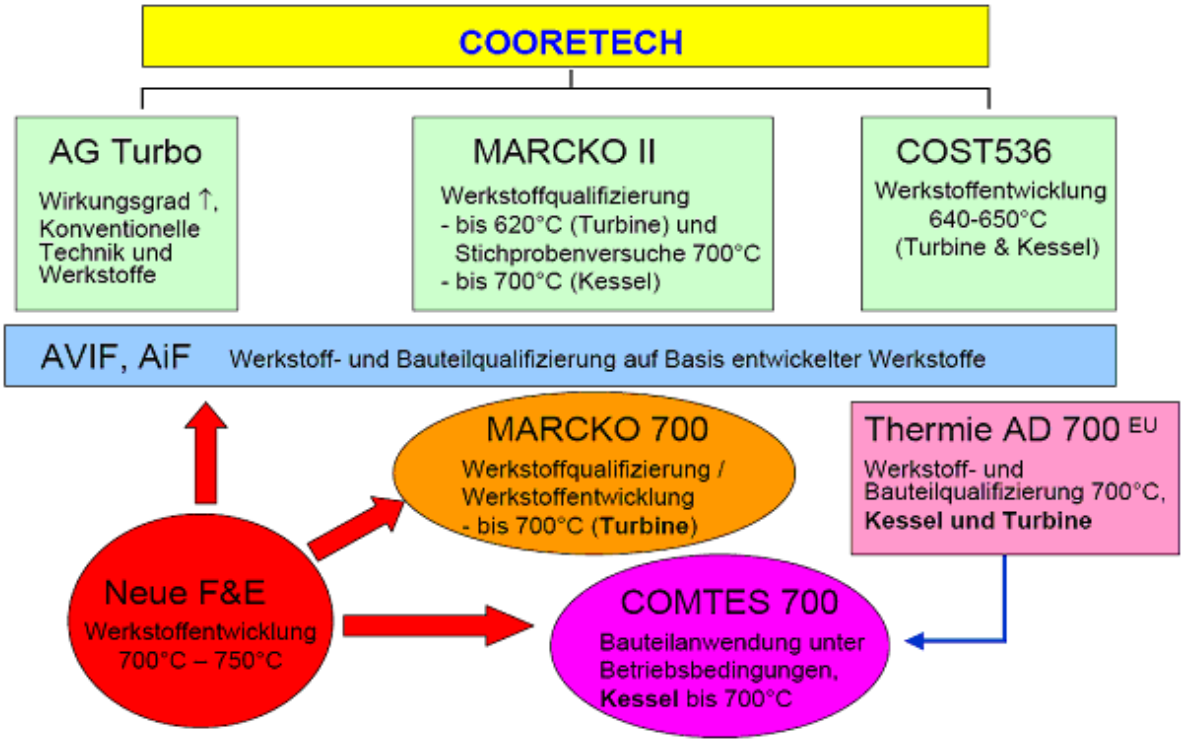

Abbildung 1: Strategische Kraftwerksprogramme

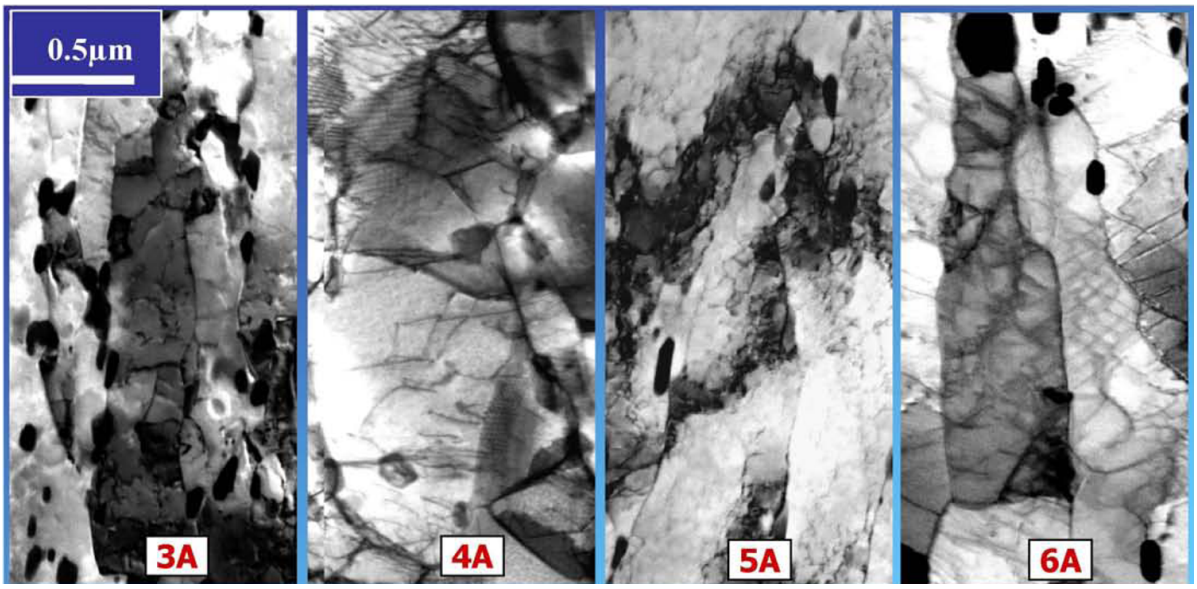

Abbildung 2: Representative micrographs of the investigated steels in their initial state

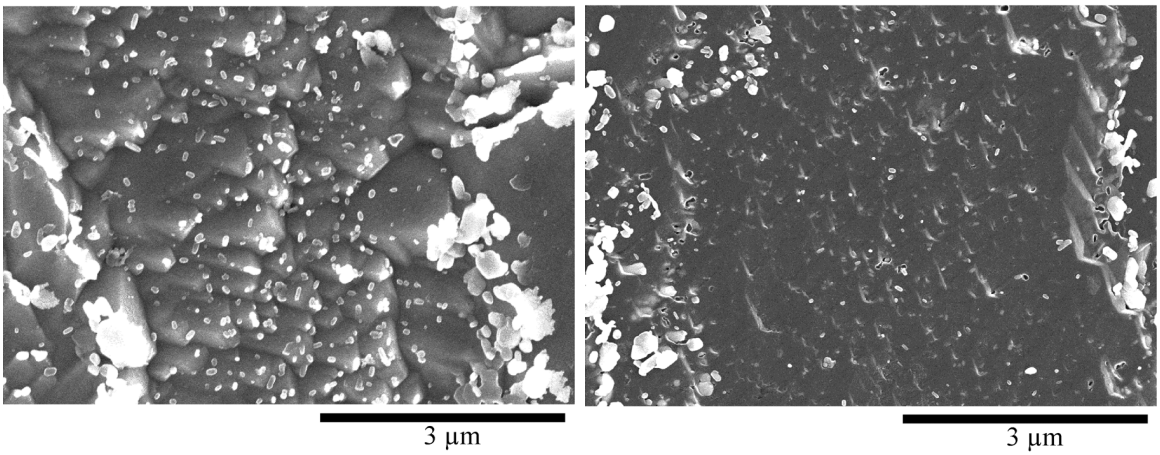

Abbildung 3: Microstructure (high resolution SEM) of 1A in initial state after heat treatment; left: surface after etching and washing with precipitates on top of peaks, right: replica [13].

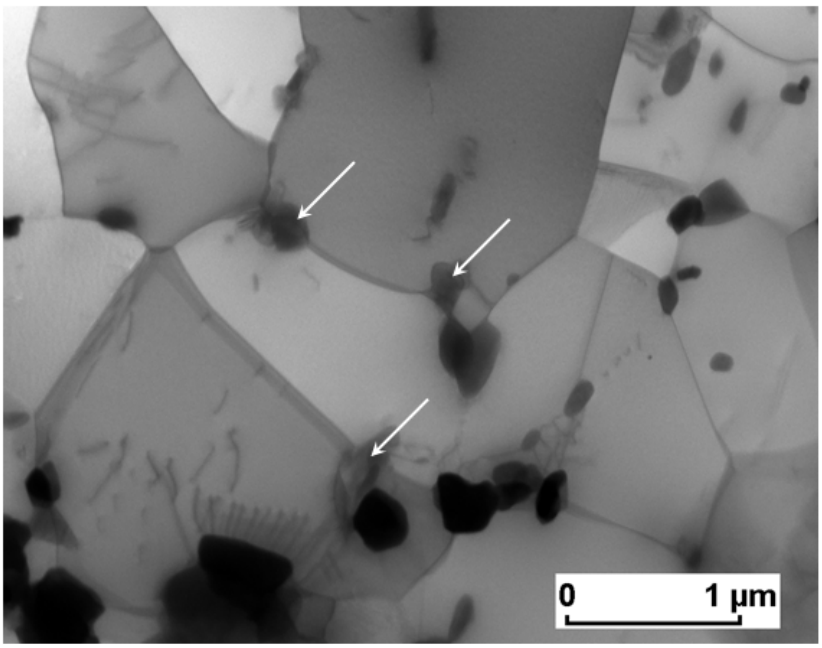

Abbildung 4: Z-phase particles located on the subgrain boundaries [14]

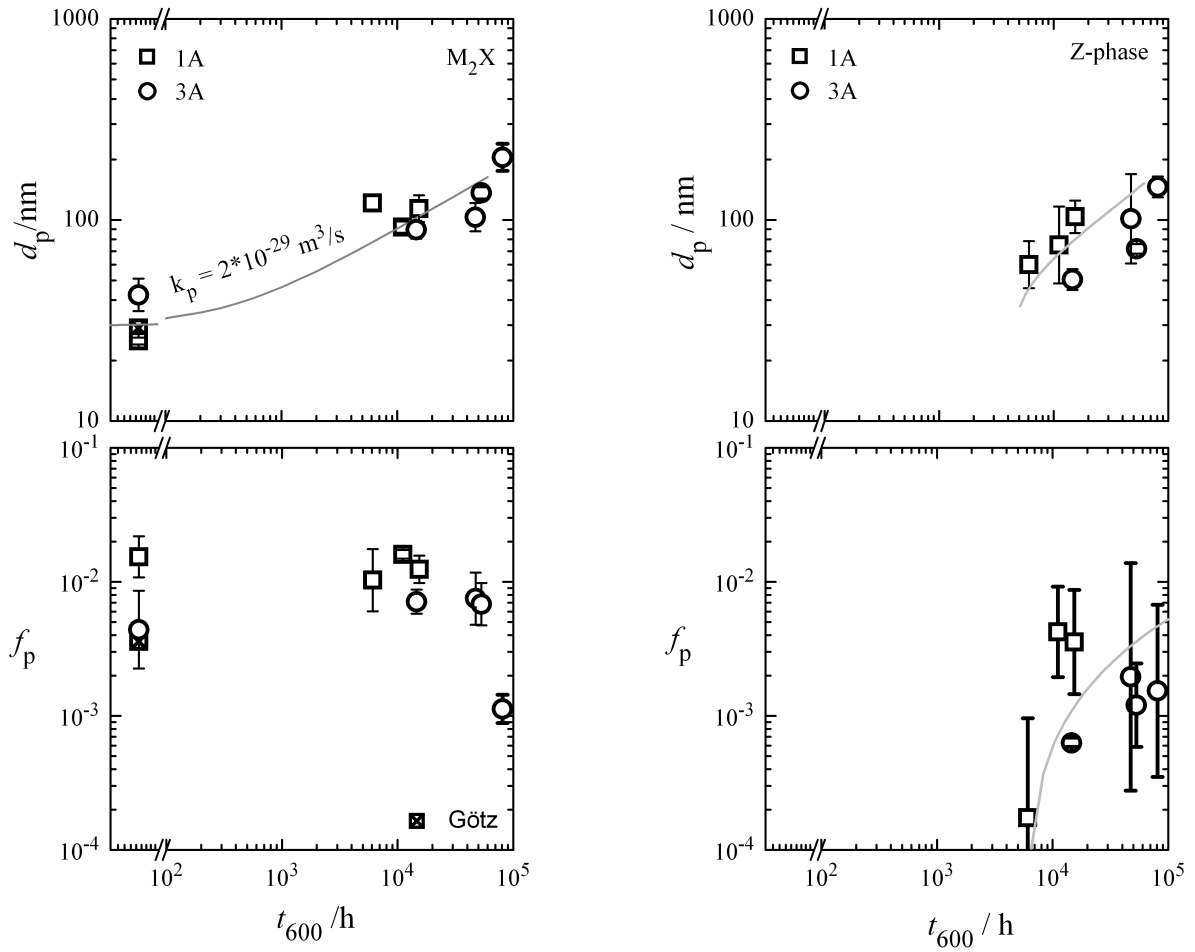

Abbildung 5: left: evolution of M_2X; right: evolution of Z-phase. Coarsening but no dissolution of M_2X by in the presence of Z-phase in 1A and 3A

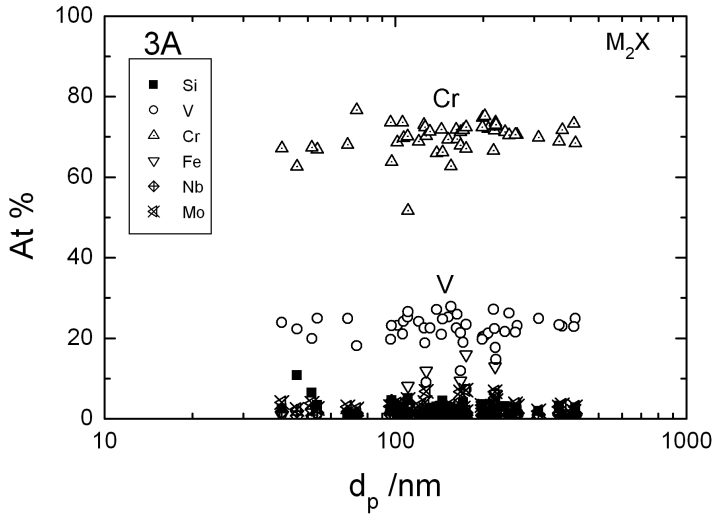

Abbildung 6: M_2X chemical composition independent of particle size

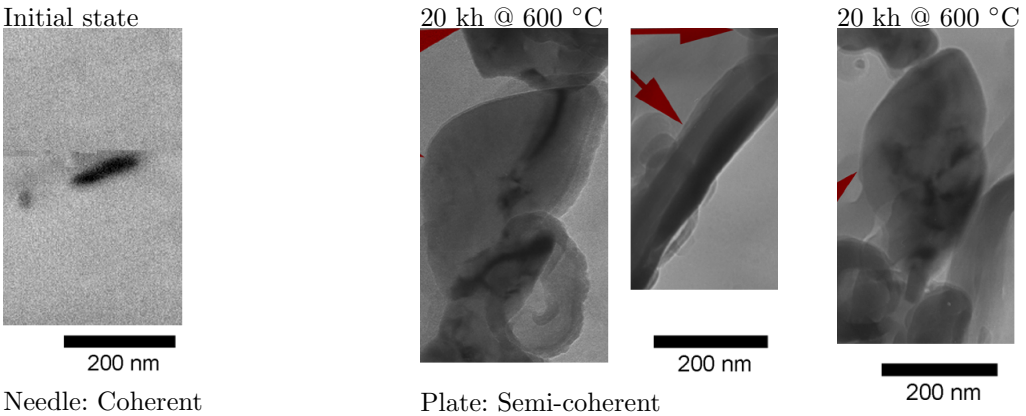

Abbildung 7: Evolution of M_2X particle size and shapes, suggesting a change in coherency

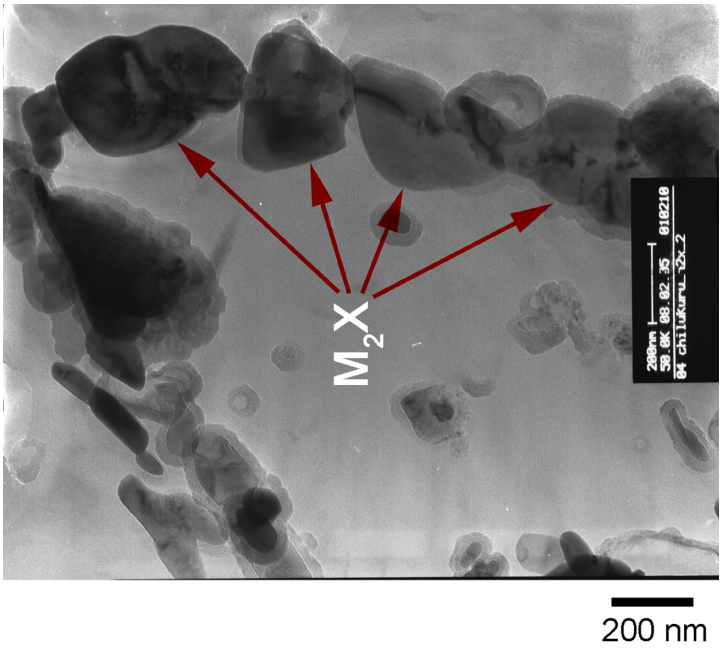

Abbildung 8: 1A after 20 kh @ 600 °C, subgrain boundary decorated with few large M_2X particles precipitated at the expense of small M_2X particles that were present inside the subgrain

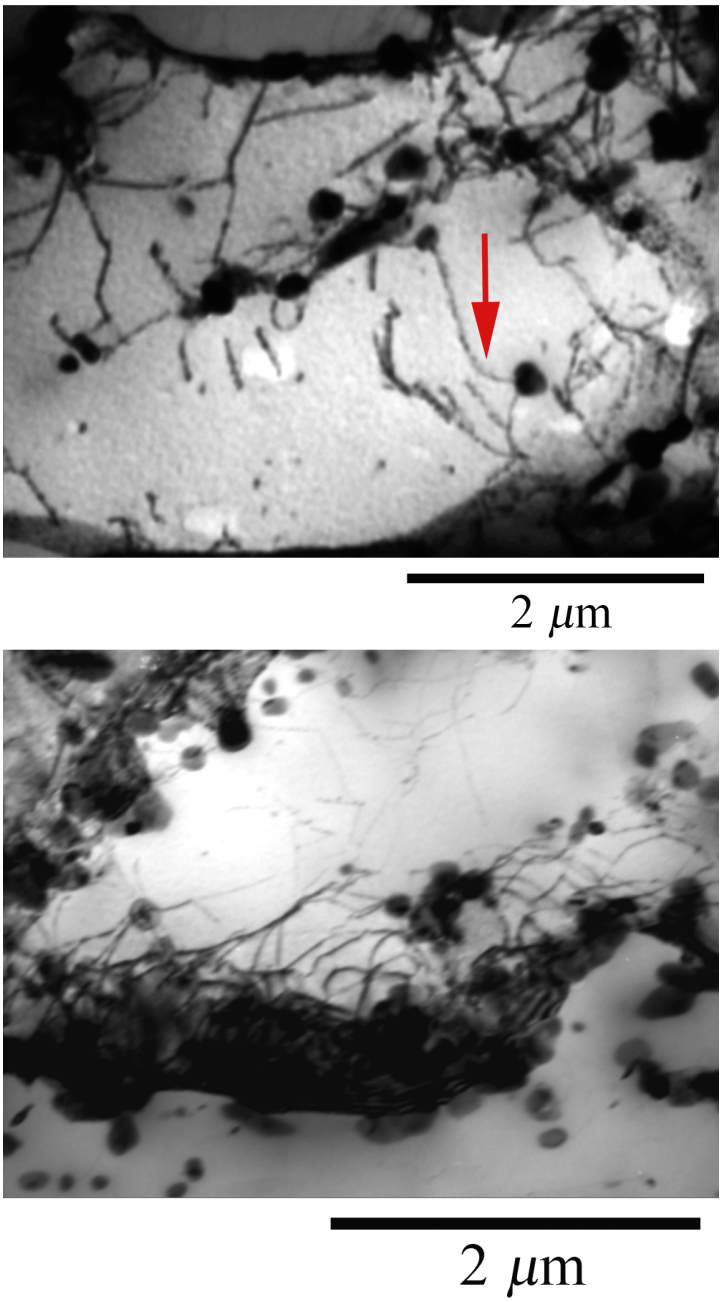

Abbildung 9: In situ images of 2A. top: dislocations pinned and bowing between the particles. bottom: dislocations bowing out from the subgrain boundaries.

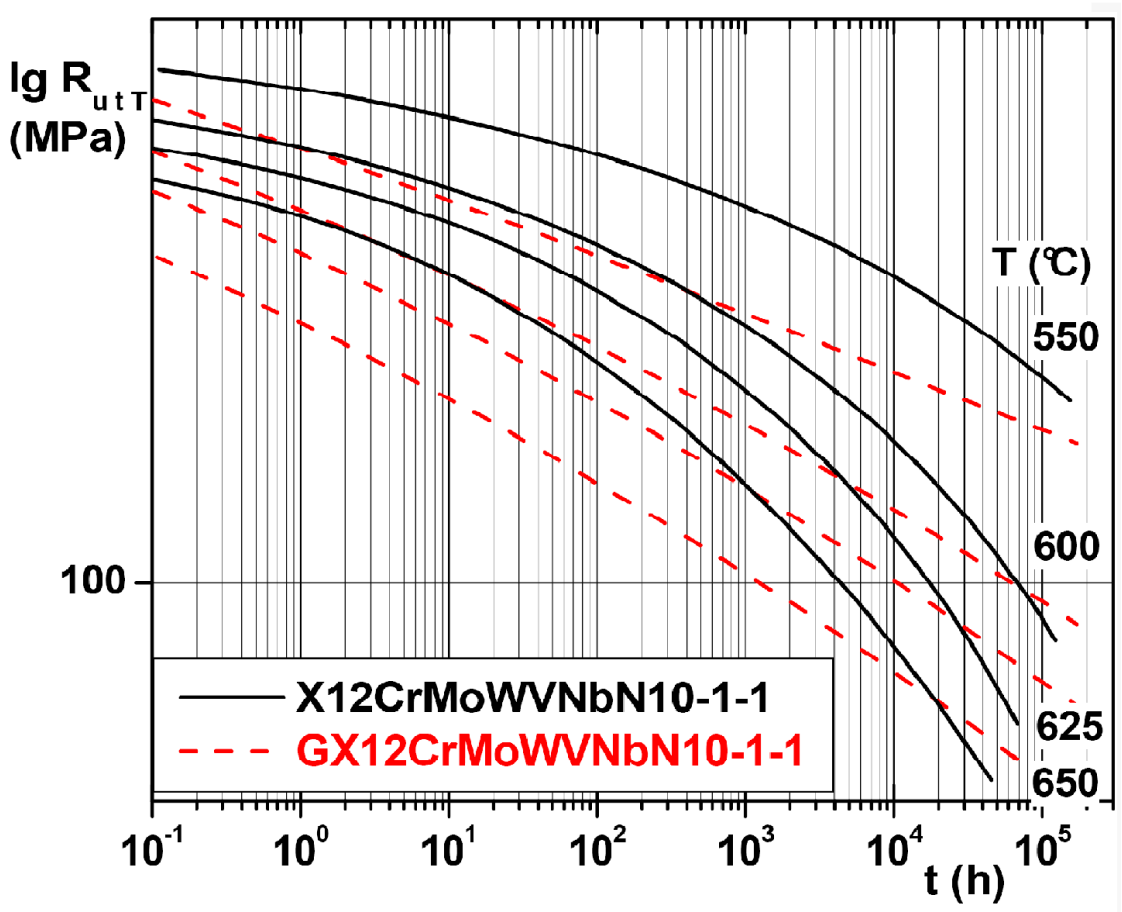

Abbildung 10: Creep rupture curves from IfW Darmstadt, showing rapid degradation of creep resistance in 1A (X12CrMoWVNbN10-1-1) by coarsening of M_2X , compared to MX hardened 2A (GX12CrMoWVNbN10-1-1)

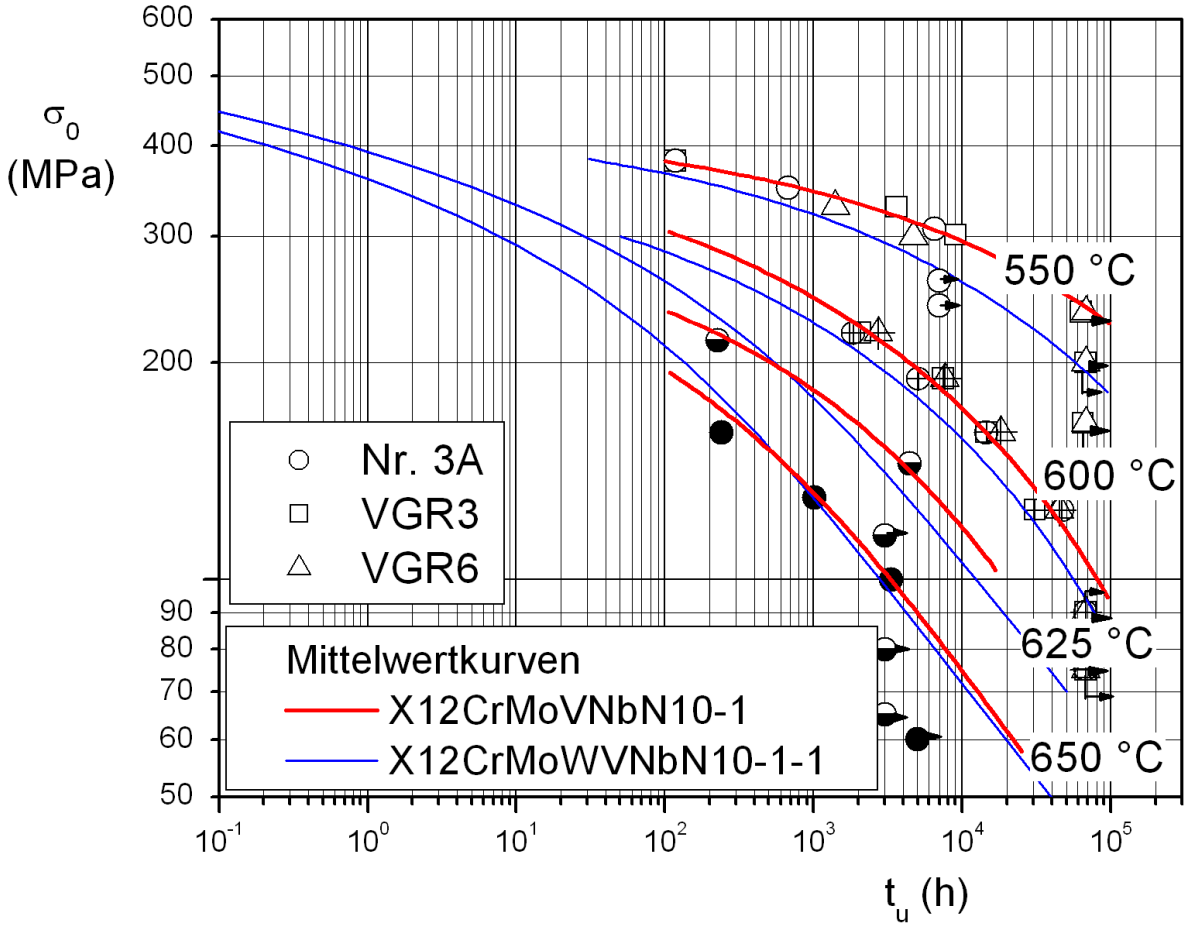

Abbildung 11: 1A (X12CrMoWVNbN10-1-1) and 3A (X12CrMoVNbN10-1) creep rupture curves from IfW Darmstadt.

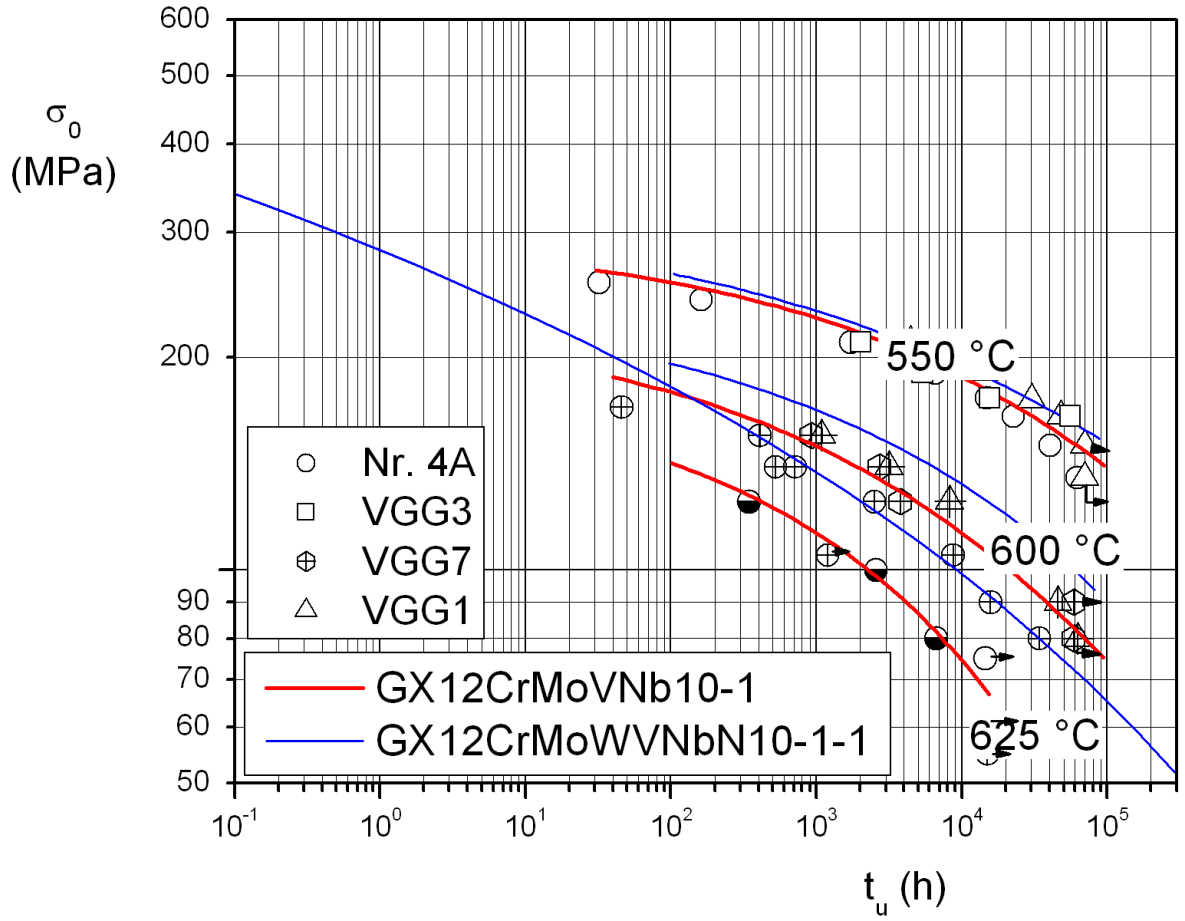

Abbildung 12: 2A (GX12CrMoWVNbN10-1-1) and 4A (GX12CrMoVNbN10-1) creep rupture curves from IfW Darmstadt.

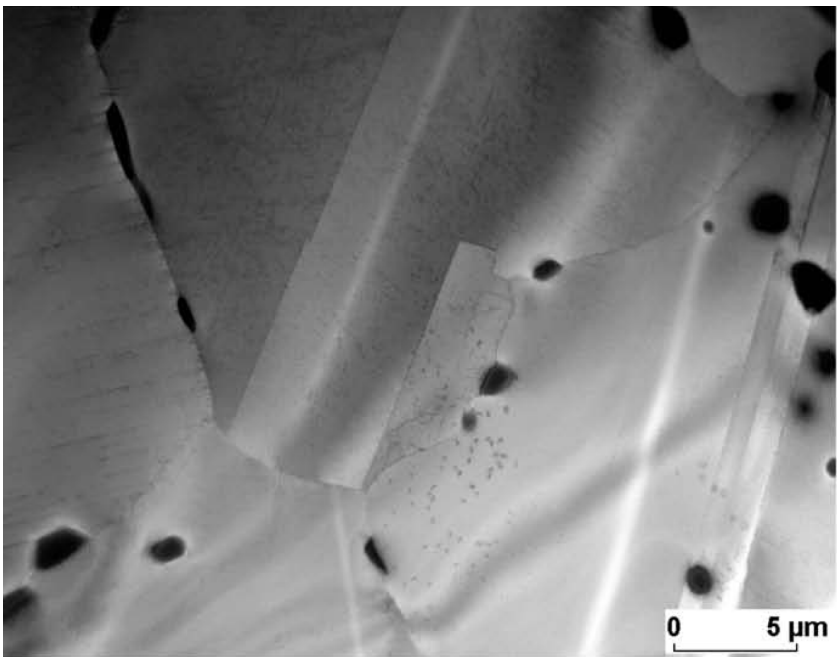

Abbildung 13: Large $M_{23}C_6$ particles on the grain boundaries in 7A

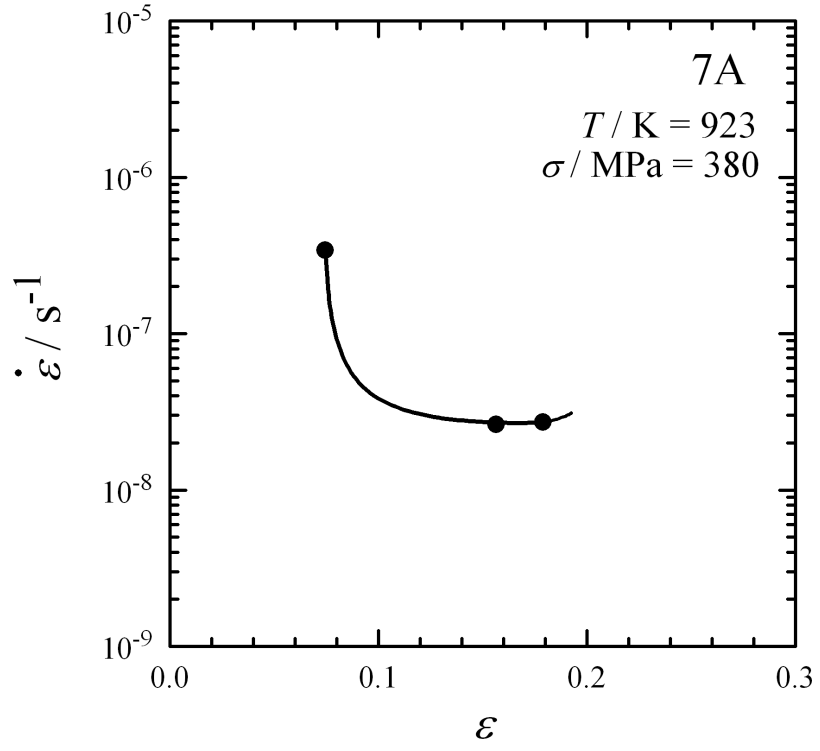

Abbildung 14: 7A creep curve

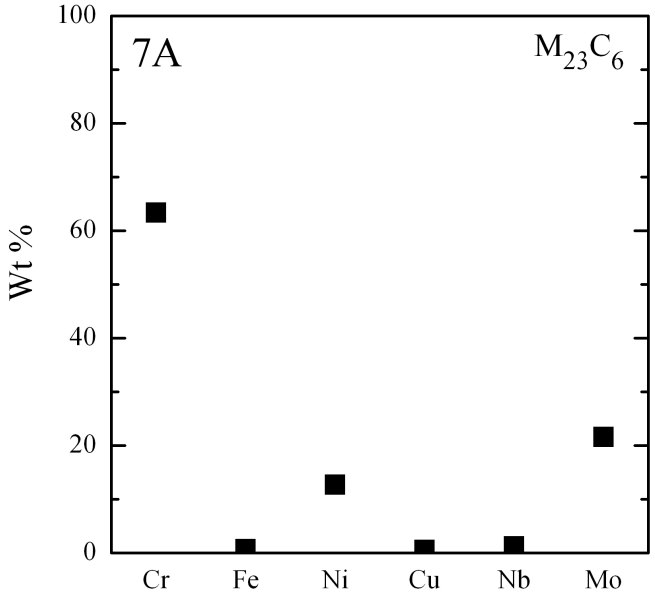

Abbildung 15: $M_{23}C_6$ chemical composition in 7A

Literatur

[1] A. Strang and V. Vodarek. Z phase formation in martensitic 12CrMoVNb steel. *Materials Science and Technology*, 12:552–556, July 1996.

[2] F. Abe. Evolution of microstructure and acceleration of creep rate in tempered martensitic 9Cr-W steel. *Mater. Sci. Eng. A*, 234-236:1045–1048, August 1997.

[3] K. Sawada, M. Takeda, K. Maruyama, R. Ishii, M. Yamada, Nagae Y., and R. Komine. Effect of W on Recovery of Lath Structure During Creep of High Chromium Martensitic Steels. *Mater. Sci. Eng. A*, 267:19–25, 1999.

[4] T. Fujita. Advances in 9-12% Cr Heat resistant Steels for Power Plants. In R. Viswanathan, W.T. Bakker, and J. D. Parker, editors, *Advances in materials technology for fossil power plants, Proc. of the 3rd Conference held at University of Wales Swansea, 5th April - 6th April 2001*, pages 33–65, London, 2001. The Institute of Materials.

[5] G. Götz and W. Blum. Influence of thermal history on precipitation of hardening phases in tempered martensite steel of type X12CrMoWVNbN10-1-1. *Mater. Sci. Eng. A*, 348/1-2:201–207, 2003.

[6] J. Hald. Long-term Stability of 9-12% Cr Steels - Current Understanding and Future Perspectives. In *Werkstoffe und Qualitätssicherung 2004*, Dortmund, March 2004. VGB.

[7] W. Blum and H. Chilukuru. Tertiary creep of tempered martensite 9-12microstructural origin of creep life limitation. In *OPE 2006 - Chennai, International Conference on Pressure vessels and Piping*, Chennai, 2006.

[8] F. Abe. Bainitic and martensitic creep-resistant steels. *Current Opinion in Solid State and Materials Science*, 8:305–311, 2004.

[9] H. Chilukuru, M. Schwienheer, A. Scholz, and W. Blum. Subgrain coarsening in tempered martensite steel X12CrMoWVNbN10-1-1 due to cyclic deformation. In S.L. Mannan, editor, *4th Conference on Creep, Fatigue and Creep-Fatigue Interaction, Kalpakkam, Indien, Oct 8-10, 2003*, pages C39–C44, 2003.

[10] H. Chilukuru, W. Blum, M. Schwienheer, and A. Scholz. Creep-fatigue interaction in martensitic tempered steels by dynamic subgrain growth. In *Langzeitverhalten warmfester Stähle und Hochtemperaturwerkstoffe, Beiträge zur 26. Vortragsveranstaltung der Arbeitsgemeinschaft für warmfeste Stähle und für Hochtemperaturwerkstoffe am 28. November in Düsseldorf*, pages 65–74. Stahlinstitut VDEh, 2003.

[11] J.S. Dubey, H. Chilukuru, J.K. Chakravartty, M. Schwienheer, A. Scholz, and W. Blum. Effects of cyclic deformation on subgrain evolution and creep in 9-12% Cr-steels. *Materials Science and Engineering A*, 406:152–159, 2005.

[12] G. Götz, Y. Qin, and W. Blum. Investigation of precipitation in cast martensitic annealed steel X12 CrMoVWNbN 10-1-1 by semiautomatic EDX-analysis in the scanning transmission electron microscope. In R. Viswanathan, W.T. Bakker, and J. D. Parker, editors, *Advances in materials technology for fossil power plants, Proc. of the 3rd Conference held at University of Wales Swansea, 5th April - 6th April 2001*, pages 155–163, London, 2001. The Institute of Materials.

[13] T. Seibert, K. Durst, H. Chilukuru, W. Blum, and M. Göken. Quantitative Gefügeananlyse von 9-12%Cr Stählen mittels AFM, REM und TEM. In Mathias Göken, editor, *37. Praktischen Metallographie Sonderbände - Fortschritte in der Metallographie*, page 73, Erlangen, Sept. 2005. DGM.

[14] R. Agamennone, W. Blum, C. Gupta, and Chakravartty. Evolution of microstructure and deformation resistance in creep of tempered martensitic 9-12%cr-2%w-5%co steels. *Acta Mater.*, im Druck, 2006.

[15] K. Kimura, K. Suzuki, H. Kushima, and F. Abe. Precipitation of Z-phase and its effect on creep strength of Mod.9Cr-1Mo steel. In R. Gladiš A. Jakobová Z. Kuboň J. Purmenský M. Filip, V. Foldyna and J. Sobotka, editors, *Proceedings of the 10th joint International Conference on Creep & Fracture of Engineering Materials and Structures, Creep Resistant Metallic Materials, 8-11 April 2001*, pages 186–195, Prag, Czech Republic, 2001. Vitkovice-Research and Development and TERIS 2002.

[16] H. Danielsen and J. Hald. Z-Phase in 9-12%Cr Steels. Technical Report M4-313, Värmeforsk Service AB, 10153 Stockholm, February 2004.

[17] I. Letofsky-Papst, P. Warbichler, F. Hofer, E. Letofsky, and H. Cerjak. On the occurrence of Z-phase in a creep-tested 10% Cr steel. *Z. Metallkd.*, 95(1):18, 2004.

[18] L. Lundin, S. Fällman, and H.-O. Andrén. Microstructure and mechanical properties of a 10% chromium steel with improved creep resistance at 600°C. *Mat. Sci. Tech.*, 13(3):232–242, 1997.

[19] X. H. Zeng and W. Blum. Modelling the Influence of Microstructure on Creep Strength of G-X12CrMoWVNbN 10-1-1. In *29th MPA Seminar, Safety and Reliability in Energy Technology, Oct 2003*, Stuttgart, 2003.

[20] T. Barkar and J. Agren. Creep simulation of 9-12% cr steels using the composite model with thermodynamically calculated input. *Materials Science and Engineering A*, 395:110–115, 2005.

[21] R. Sedláček and W. Blum. Microstructure-based Constitutive Law of Plastic Deformation. *Comp. Mater. Sci.*, 25(1-2):200–206, 2002.

[22] P. Polcik. *Modellierung des Verformungsverhaltens der warmfesten 9-12%Chromstähle im Temperaturbereich von 550–650°C.* D29 (Dissertation Universität Erlangen-Nürnberg). Shaker Verlag, Aachen, 1999.

[23] S. Straub. *Verformungsverhalten und Mikrostruktur warmfester martensitischer 12%-Chromstähle*. Fortschr.-Ber. VDI Reihe 5 Nr. 405. VDI Verlag, Düsseldorf, 1995.

A Publication [9]

Subgrain coarsening in tempered martensite steel X12CrMoWVNbN10-1-1 due to cyclic deformation

H. Chilukuru, M. Schwienheer, A. Scholz, and W. Blum

In S.L. Mannan, editor, *4th Conference on Creep, Fatigue and Creep-Fatigue Interaction, Kalpakkam, Indien, Oct 8-10*, 2003, pages C39-C44, 2003.

SUBGRAIN COARSENING IN TEMPERED MARTENSITE CrMoV-STEEL DUE TO CYCLIC DEFORMATION

H. Chilukuru†, M. Schwienheer‡, A. Scholz‡, W. Blum†

† *Institut für Werkstoffwissenschaften LS1, Universit ät Erlangen-Nürnberg Martensstraße 5, D-91058 Erlangen, Germany*

‡ *Institut für Werkstoffkunde, Technische Universit ät Darmstadt Grafenstr. 2, D-64229 Darmstadt, Germany*

ABSTRACT

Tempered martensite 9-12% Cr-steels are used for heat, stress, and corrosion resistant parts in power stations. Their deformation resistance stems from particle stabilized subgrain hardening. It is known that the subgrain structure coarsens during creep. This coarsening leads to softening as is evident from onset of tertiary creep in compression. In the present work the influence of cyclic loading at elevated temperature has been investigated. A specimen of G-X12CrMoWVNbN10-1-1 was subjected to tensile-compressive strain cycles at 600°C with four hold periods where stress was relaxing. The total number of cycles till fracture was 724 and the total time of cyclic loading 2317 h. It was found that there was significant subgrain coarsening during cyclic loading from the initial subgrain size of 400 nm to about 1500 nm. A subsequent creep test proved that the subgrain coarsening by cyclic deformation led to softening, with an increase of the minimum creep rate by a factor of 15. The results confirm that subgrain hardening is an important strengthening mechanism in tempered martensite steels and that the synergistic interaction of both creep loading and cyclic loading has to be accounted for in estimating the lifetime of the steels.

INTRODUCTION

It is well known that the subgrain structure of materials approaches a steady state in the course of deformation. This holds also for Cr-steels which inherit their fine subgrain structure from martensitic transformation followed by tempering. Under conditions of creep at elevated temperatures as applied in power stations the size of the subgrains (which is a measure of the subgrain boundary area per volume) usually increases towards a steady state value which is a unique function of (shear modulus normalized) applied stress. Under conditions of cyclic deformation the situation is more complicated, because the stress is not constant and may even change its sign. The definition of steady state must be adjusted to this situation. In principle, there is no longer a unique steady state size of subgrains. Rather, there is a subgrain size evolution during each cycle and it is the history of this evolution during each cycle which approaches a steady state in the sense of exactly repeating itself from cycle to cycle. However, as the subgrain structure evolution is rather sluggish, the fluctuation of subgrain size in a single cycle is expected to be rather small. So far there is little knowledge about the effect of cyclic deformation on subgrain structure evolution. In the present work the subgrain size has been determined for a member of the group of 9-12% Cr-steels after a specific long term cyclic deformation treatment. It will be shown that this cyclic loading

causes significant coarsening of the dislocation structure. This has important consequences for the lifetime of the steels under complex loading conditions.

CYCLIC DEFORMATION

The chemical composition and the heat treatment of the tempered martensite steel with the German designation G-X12CrMoWVNbN10-1-1 (Nr. 2A) investigated in this work has been

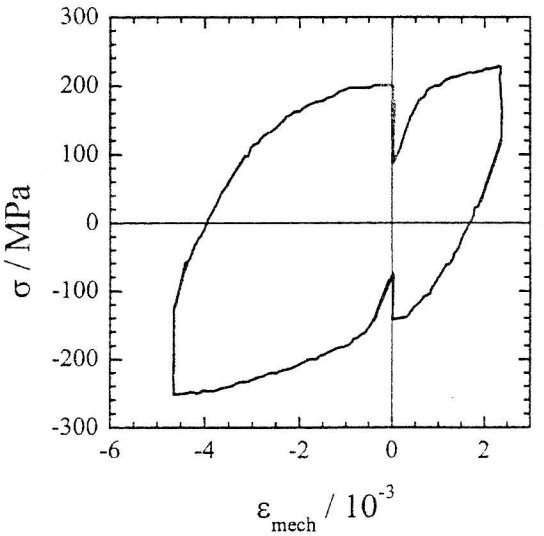

Figure 1: Stress σ-(mechanical) strain ϵ_{mech} cycle at 873 K with stress relaxations during hold times $t_{Hd\,1}$ = 0.24 h at ϵ_{mech} = -0.467% under compressive stress, $t_{Hz\,1}$ = 2.24 h at ϵ_{mech} = 0 under tensile stress, $t_{Hz\,2}$ = 0.48 h at ϵ_{mech} = 0.233% under tensile stress, and $t_{Hd\,2}$ = 0.24 h at ϵ = 0 under compressive stress.

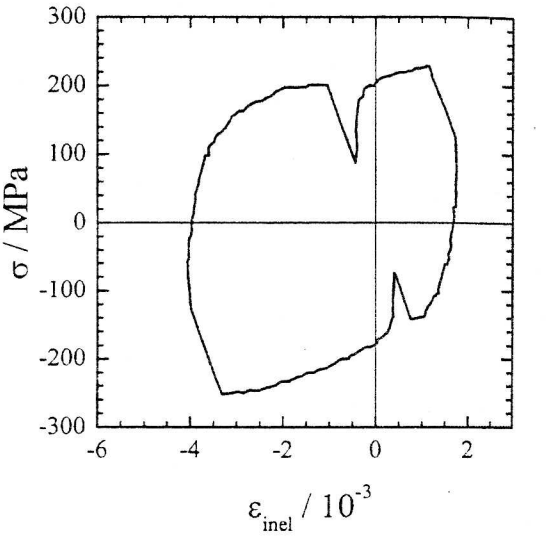

Figure 2: σ-ϵ_{inel}-curve of cycle of Fig. 1.

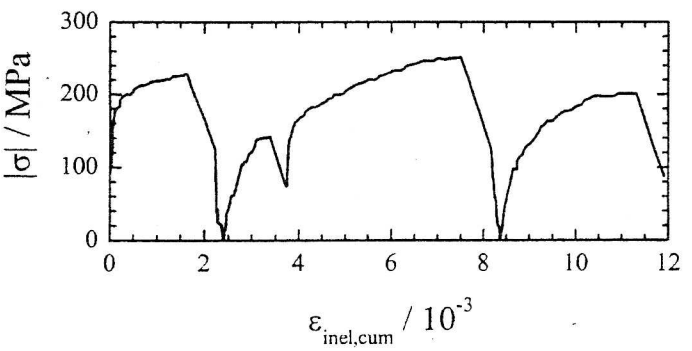

Figure 3: $|\sigma|$-$\epsilon_{inel,cum}$-curve of cycle of Fig. 1.

reported elsewhere[1]. The conditions of cyclic deformation have been adapted to the conditions in power stations. Deformation occurred in mechanical (elastic plus inelastic) strain ϵ_{mech}-control at 873 K with a tensile strain amplitude of 0.233 % and a compressive strain amplitude of 0.467 %, resulting in a total strain amplitude of $\Delta\epsilon_{mech}$ = 0.7%. The specimen

fractured after $N_A = 724$ cycles. Fig. 1 shows the variation of stress σ with mechanical strain ϵ_{mech} for a cycle at approximately half lifetime. There were four periods of stress relaxation during hold times in tension as well as compression. The cycle period was 3.2 h. The time to fracture was $t_A = 2317$ h.

After each stress relaxation, the material behaves predominantly elastically. This behavior is reflected by a linear σ-ϵ_{mech} relation with slopes E. $E = 190$ GPa was used to determine the inelastic strain $\epsilon_{inel} = \epsilon_{mech} - \sigma/E$. Fig. 2 displays the cyclic stress-strain curve with inelastic strain plotted on the abscissa. The increase in absolute magnitude of inelastic strain during stress relaxation is now becoming apparent. The cumulative inelastic strain is defined as $\epsilon_{inel,cum} = \int |d\epsilon_{cyclic}|$. Fig. 3 shows the variation of the absolute magnitude of stress $|\sigma|$ with $\epsilon_{inel,cum}$ during the cycle.

SUBGRAIN SIZE EVOLUTION

The initial dislocation structure of the specimen after quality heat treatment consists of subgrains of size $w_0 \approx 400$ nm.[1] During deformation at a low constant value of stress σ the subgrain structure will coarsen with strain[2] at the rate:

$$\frac{d \log w}{d\epsilon} = -\frac{\log w - \log w_\infty}{k_{\log w}} \qquad w_\infty = \frac{10bG}{\sigma} \tag{1}$$

where w_∞ is the steady state subgrain size, $k_{\log w}$ is a growth constant which was set to 0.12, $b = 0.248$ nm is the length of the Burgers vector and $G = 63$ GPa is the shear modulus at test temperature. Little is known about the behavior of the subgrain structure during alternating strain cycling. The final subgrain size after cycling was determined by the line intersection technique as the average w of subgrain intercept lengths w_i, measured from montages $i = 1, 2, ...$ of TEM pictures. As seen in Fig. 4, the subgrain structure is elongated.

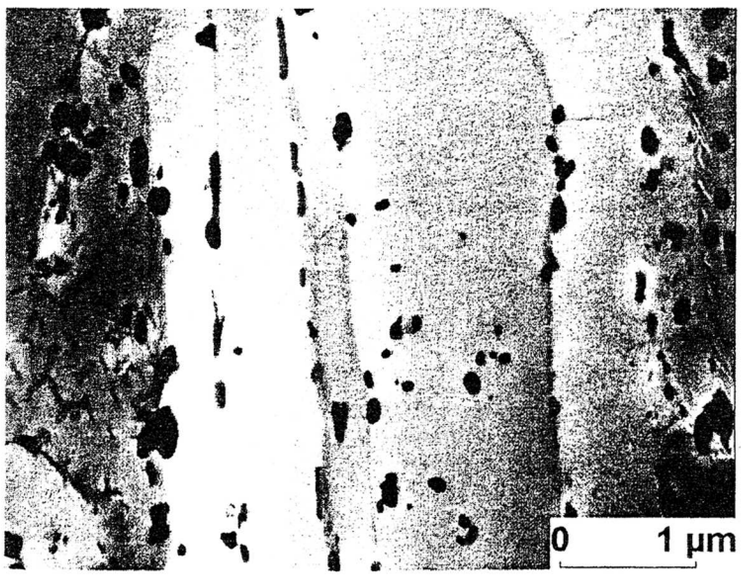

Figure 4: Microstructure with elongated subgrains

For each montage measurements were done in the directions parallel and perpendicular to the elongation. Parallel test lines were drawn in each direction and the distance between the points of intersection between test line and subgrain boundaries was measured using the software 'Grab It'. The averages of these intercepts $w_i^{\parallel}$ and $w_i^{\perp}$ are the subgrain sizes in the directions parallel and perpendicular to the direction of elongation in the investigated area

A_i. For equiaxed subgrains, $w_i^{\parallel} = w_i^{\perp} = w_i$, it is known that the subgrain boundary area per volume equals $2/w_i$. Therefore, in this case the boundary area can be expressed as:

$$\frac{2}{w_i} = \frac{1}{w_i^{\parallel}} + \frac{1}{w_i^{\perp}} \tag{2}$$

We extend this formula to the case where $w_i^{\parallel} \neq w_i^{\perp}$. It was checked that this value agrees to within 10% with the subgrain sizes determined previously[1] from test lines extending at an angle of about 45° to the direction of elongation. The volume average of the subgrain size is:

$$w = \frac{1}{A} \sum_{i=1}^{N} A_i w_i \qquad\qquad A = \sum A_i. \tag{3}$$

The experimental error of w was quantified by 95% confidence limit. The resulting subgrain size obtained from a total investigated area $\sum A_i = 1731 \mu\text{m}^2$ is $w = (1.54 \pm 0.23)\ \mu\text{m}$. The subgrain aspect ratio was found to be $w_i^{\parallel}/w_i^{\perp} = 1.4$.

The subgrain size after cyclic deformation can be estimated from the stress-strain curves. The simplest estimate is based on the assumption that the subgrain size adjusts to the steady state value which would be observed during monotonic creep at the maximum stress $\sigma_{\text{max}} =$ 250 MPa occurring within the cycle. From (1) one gets $w(\sigma_{\text{max}}) = 625$ nm. This value is expected to be a lower bound, because the periods with smaller stresses and the changes in direction of straining during the cycles have been neglected. The expectation is confirmed by the experimental data (Fig. 5). A better estimate can be made by applying eq. (1) to the curve of Fig. 3. The evolution of w was derived from this curve by digitizing the curve and integrating (1) numerically. The resulting evolution of w with $\epsilon_{\text{inel,cum}}$ is shown

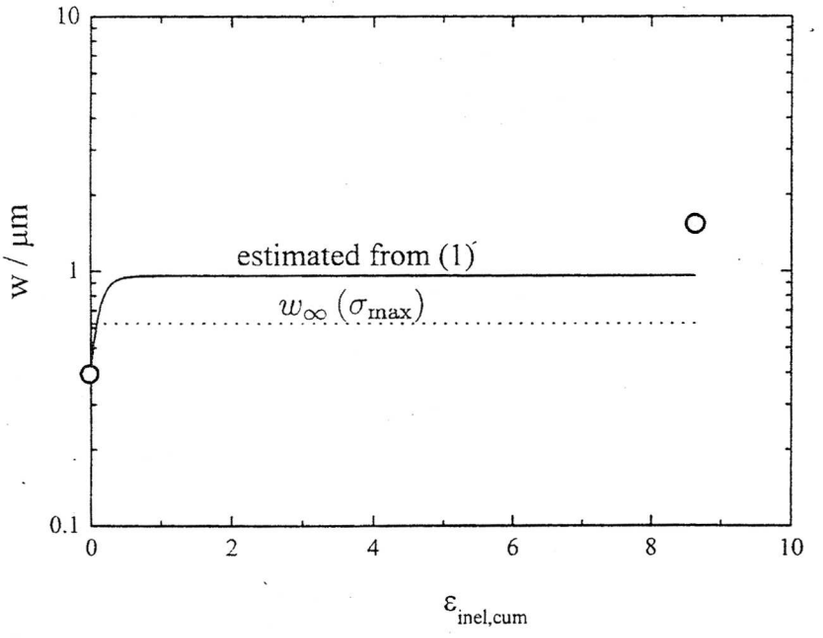

Figure 5: Subgrain size w as function of cumulative strain $\epsilon_{\text{inel,cum}}$.

in Fig. 5. Starting from the initial value $w_0 = 400$ nm, w increases. Beyond a strain corresponding to 82 cycles there is no more coarsening of the subgrains, resulting in a steady state at $w = 975$ nm. This value is closer to the experimental value than the previous one, but still lower by 50%.

DISCUSSION

The transmission electron microscopic results show that cyclic deformation leads to considerable subgrain coarsening from 400 to 1500 μm within a relatively short period of time < 2317 h. This result obtained by probing an extremely small volume of the specimen was checked by a mechanical test. According to (1) there will be no subgrain coarsening, if the cyclically deformed specimen is crept under a stress of 98 MPa, because the steady state subgrain size at that stress equals the subgrain size in the cyclically deformed specimen. Fig. 6 shows the $\dot{\epsilon}$-ϵ-curve of the cyclically deformed specimen measured at 923 K together with the curve which would be expected for a specimen with the initial subgrain size of 400 nm resulting from the quality heat treatment. The latter curve displays a pronounced minimum in $\dot{\epsilon}$, whereas in the former curve a relative minimum in $\dot{\epsilon}$ is nearly absent. The minimum of $\dot{\epsilon}$ is interpreted to result from subgrain coarsening. Consistent with that, the lack of a pronounced relative $\dot{\epsilon}$-minimum in the other curve indicates that nearly no subgrain coarsening is necessary. Thus, the result of the creep test on the cyclically deformed specimen with coarsened subgrain structure is fully consistent with the TEM observation.

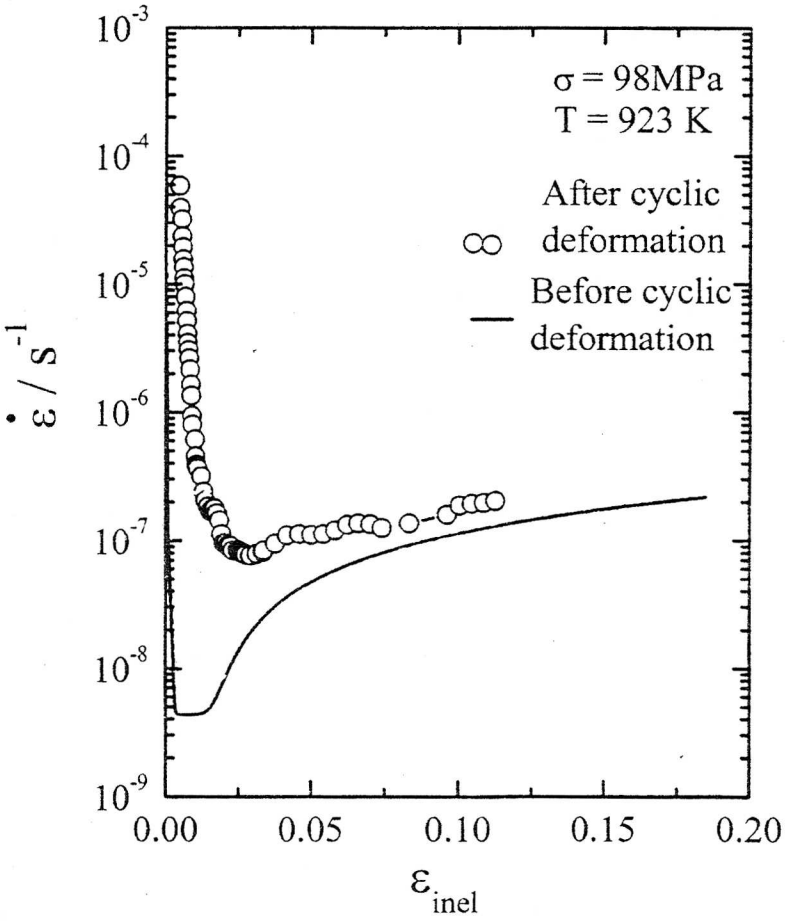

Figure 6: Compressive creep rate $\dot{\epsilon}$ as function of strain ϵ after cyclic deformation. The curve to be expected without prior cyclic deformation was calculated from the modified Garofalo creep equation reported by[3]

Both estimates of the cyclic steady state subgrain size based on $w(\sigma_{\max})$ as well as eq. (1) yields values which are distinctly smaller than the measured one. The probable reason is that the change in the direction of dislocation motion during each cycle has been neglected. As the stress changes from tension to compression and back the dislocations stop and continue moving in the opposite direction. This backward motion may cause significant recovery of

the dislocation content. This extra recovery due to cycling may lead to enhanced subgrain growth.

The results show that there is an interaction between cyclic deformation and creep (creep-fatigue interaction) causing degradation of the creep resistance by prior cyclic deformation leading to enhanced subgrain growth. This interaction can explain deviations from the linear damage accumulation rule.

SUMMARY

Cyclic strain-controlled alternating tensile-compressive deformation at 873 K with stress relaxation during hold times and maximum stress of 250 MPa causes significant growth of subgrains from 400 to 1500 nm within distinctly less than 2317 h. The subgrain coarsening degrades the creep resistance by increasing the minimum compressive creep rate at 923 K and 98 MPa by a factor of 15, lifting it close to the steady state creep rate. The interaction between cyclic loading and creep is expected to cause deviations from the linear damage accumulation rule.

ACKNOWLEDGEMENTS

Thanks are due to the Deutsche Forschungsgemeinschaft and the consortium of BMWi and industry within the project DT1/2 for financial support.

References

[1] Y. Qin, G. Götz, and W. Blum. Subgrain structure during annealing and creep of the cast martensitic Cr-steel G-X12CrMoWVNbN 10-1-1. *Mater. Sci. Eng. A*, 341:211–215, 2003.

[2] S. Straub, T. Hennige, P. Polcik, and W. Blum. Microstructure and Creep Rate during Long-Term Cyclic Creep of the Martensitic Steel X 22 CrMoV 12 1. *steel research*, 66:394–401, 1995.

[3] C. Berger, A. Scholz, and M. Schwienheer. Ermittlung der Gebrauchseigenschaften der 600°c-Stähle, Teilprojekt Kriech-, Dehnwechsel- und Kerbverhalten. Technical report, BMWi-PTJ-Verbundvorhaben, Förderkennzeichen 0327053, Inst. f. Werkstoffkunde, TU Darmstadt, 2002.

B Publication [10]

Creep-fatigue interaction in martensitic tempered steels by dynamic subgrain growth

H. Chilukuru, W. Blum, M. Schwienheer, and A. Scholz

In *Langzeitverhalten warmfester Stähle und Hochtemperaturwerkstoffe, Beiträge zur 26. Vortragsveranstaltung der Arbeitsgemeinschaft fär warmfeste Stähle und für Hochtemperaturwerkstoffe am 28. November in Düsseldorf*, pages 65-74. Stahlinstitut VDEh, 2003.

Creep-fatigue interaction in martensitic tempered steels by dynamic subgrain growth

Hemambar Chilukuru, Institut für Werkstoffwissenschaften LS1, U Erlangen-Nürnberg
Michael Schwienheer, Institut für Werkstoffkunde, TU Darmstadt
Alfred Scholz, Institut für Werkstoffkunde, TU Darmstadt
Wolfgang Blum, Institut für Werkstoffwissenschaften LS1, U Erlangen-Nürnberg

Abstract

Tempered martensite 9-12% Cr-steels are used for heat, stress, and corrosion resistant parts in power stations. Their deformation resistance stems from particle stabilized subgrain hardening. It is known that the subgrain structure coarsens during creep. This coarsening leads to softening as is evident from onset of tertiary creep in compression. In the present work the influence of cyclic loading at elevated temperature has been investigated. Two specimens of 9-12% Cr-steels group were subjected to tensile-compressive strain cycles at 600°C with four hold periods where stress was relaxing. It was found that there was significant subgrain coarsening during cyclic deformation consistent with the observed cyclic softening, subsequent creep proved that the subgrain coarsening by cyclic deformation led to softening, with an increase of the minimum creep rate by a factor of 15. The results confirm that subgrain hardening is an important strengthening mechanism in tempered martensite steels and that the synergistic interaction of both creep loading and cyclic loading has to be accounted for in estimating the lifetime of the steels.

Introduction

It is well known that the subgrain structure of materials approaches a steady state in the course of deformation. This holds also for Cr-steels which inherit their fine subgrain structure from martensitic transformation followed by tempering. Under conditions of creep at elevated temperatures as applied in power stations the size of the subgrains (which is a measure of the subgrain boundary area per volume) usually increases towards a steady state value which is a unique function of (shear modulus normalized) applied stress. Under conditions of cyclic deformation the situation is more complicated, because the stress is not constant and may even change its sign. The definition of steady state must be adjusted to this situation. In principle, there is no longer a unique steady state size of subgrains. Rather, there is a subgrain size evolution during each cycle and it is the history of this evolution during each cycle which approaches a steady state in the sense of exactly repeating itself from cycle to cycle. However, as the subgrain structure evolution is rather sluggish, the fluctuation of subgrain size in a single cycle is expected to be rather small. So far there is little knowledge about the effect of cyclic deformation on subgrain structure evolution. In the present work we report on the subgrain size evolution for two specimens from the group of 9-12% Cr-steels after a specific long term cyclic deformation treatment. It will be shown that this cyclic loading causes significant coarsening of the dislocation structure. We also report the subgrain coarsening effect on the creep after the

specimen is subjected to cyclic loading. This has important consequences for the lifetime of the steels under complex loading conditions.

Cyclic deformation

The forged steel (Nr.1A, German grade X12CrMoWVNbN10-1-1 and the cast steel (Nr.2A, German grade G-X12CrMoWVNbN10-1-1)) were investigated in this work, The chemical composition and the heat treatment are given in Table 1 and Table 2 respectively. Details of the cyclic deformation are given in Table 3. The conditions of cyclic deformation with hold periods are similar to that in power stations.

	C	Si	Mn	B	Cr	Mo	N	Nb	V	W
1A	0.12	0.10	0.42	-	10.7	1.04	0.056	0.05	0.16	1.04
2A	0.13	0.29	0.82	0.0005	9.51	1.02	0.041	0.059	0.19	1.02

Table 1: Chemical composition of 1A and 2A in mass %.

	Austenitisation		Tempering1		Tempering2	
	T/°C	t/h	T/°C	t/h	T/°C	t/h
1A	1050	7	570	10.25	690	10
2A	1070	12	730	10	730	10

Table 2: Heat treatment of 1A and 2A.

		Nr.1A	**Nr.2A**
Temperature /°C		600	600
No of cycles (N_i)		1119	724
Hold periods			
Tension	$t_{Ht}1$	7h	2.24h
	$t_{Ht}2$	1.5h	0.48h
Compression	$t_{Hd}1$	0.75h	0.24h
	$t_{Hd}2$	0.75h	0.24h
Total strain Amplitude ($\Delta\varepsilon_{mech}$)		0.65%	0.7%
Cycling time to crack initiation t_i (h)		11190	2317

Table 3: Test parameters of the cyclic deformation in steels 1A and 2A, N_i: number of cycles to initiation of crack.

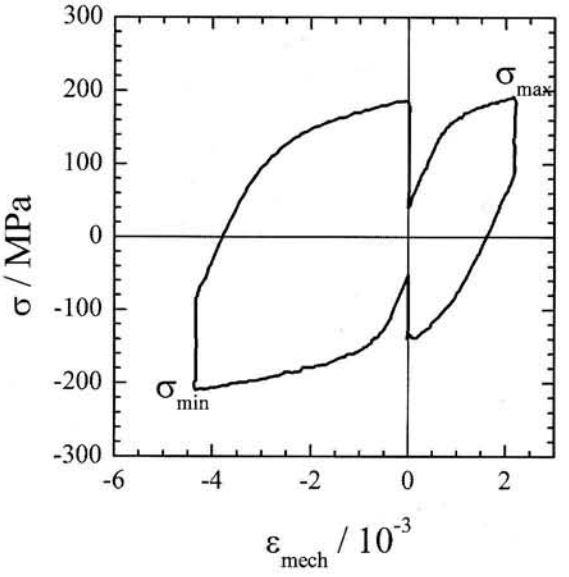

Figure 1: Stress σ - (mechanical) strain ε_{mech} cycle of the steel 1A (1000th cycle)

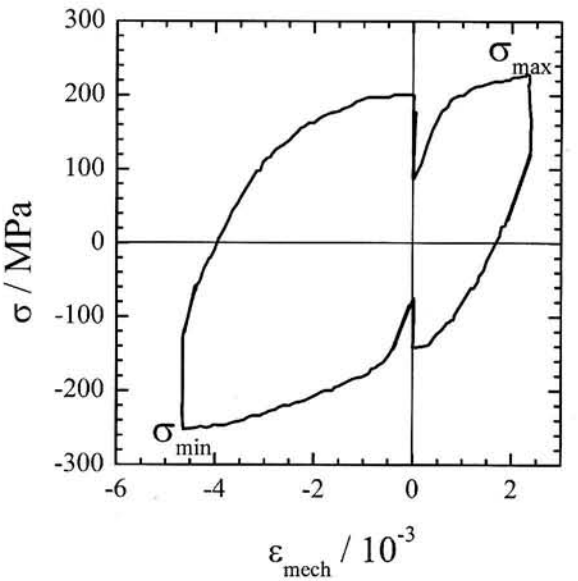

Figure 2: Stress σ -(mechanical) strain ε_{mech} cycle of the steel 2A (300th cycle)

The deformation occurred under controlled mechanical (elastic plus inelastic) strain ε_{mech}. Figures 1 and 2 show the variation of stress σ with ε_{mech} for a single cycle in steels 1A and 2A, respectively. There were four periods of stress relaxation during hold times in tension as well as compression.

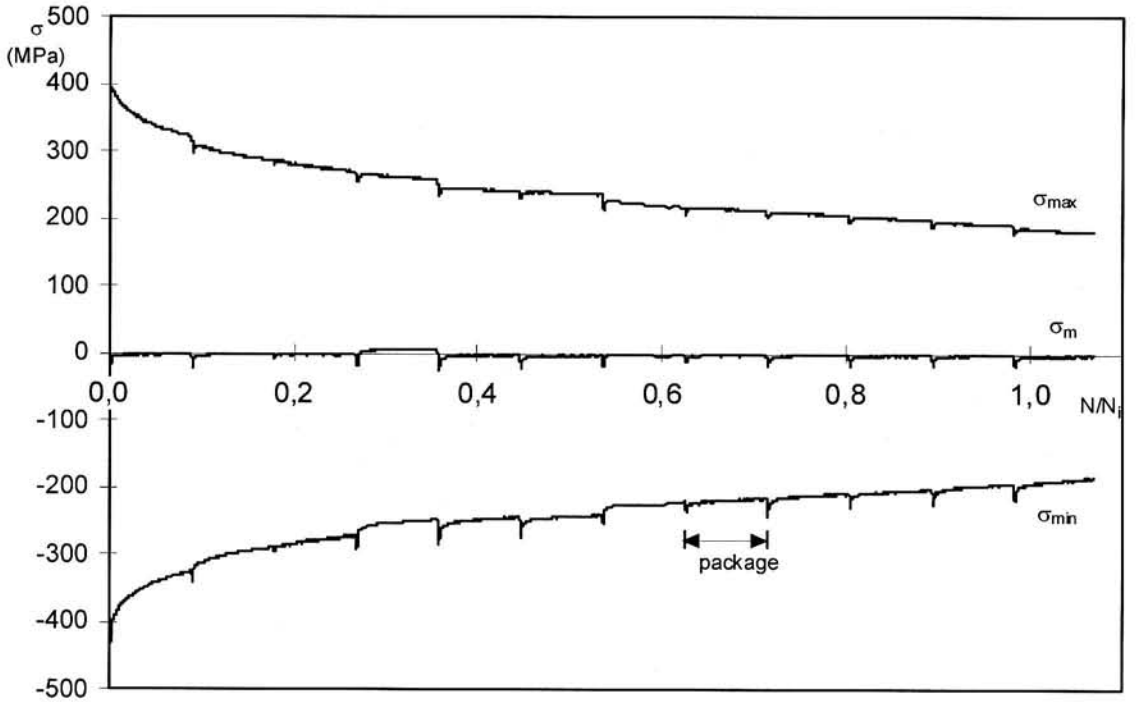

Figure 3: Variation of maximum and minimum stress amplitude as the cycling progressed in 1A. N_i =1119, t_i= 11190 h, mean stress σ_m= (σ_{max}+σ_{min})/2, test performed in "package-type"-mode [9]

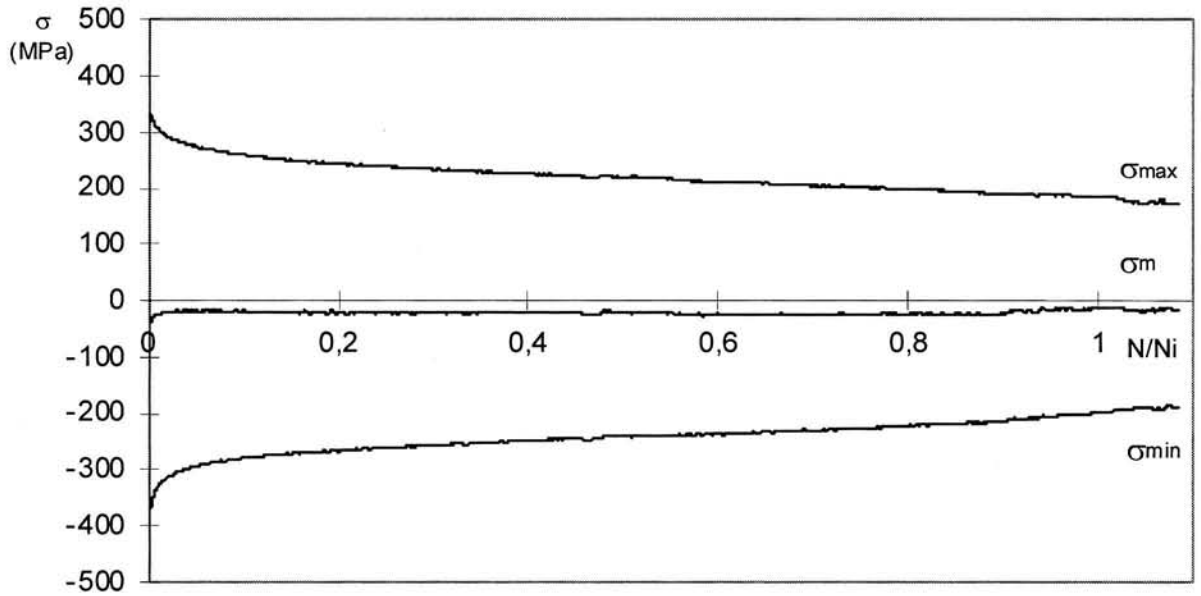

Figure 4: Variation of maximum and minimum stress amplitude as the cycling progressed in 2A. N_i =724, t_i= 2317 h, test performed in continuous mode [9]

Figures 3 and 4 show the variation of maximum and minimum stress as the cycling progressed in 1A and 2A, in both the cases, significant softening is observed in the initial cycles, followed by a gradual decline as cycling progresses.

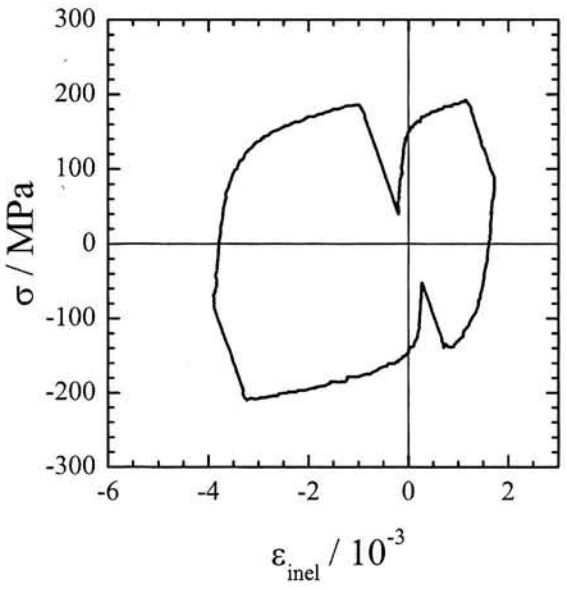

Figure 5: σ - ε_{inel} -curve of cycle of Fig.1

Figures 5 and 6 refer to a single cycle of 1A (Fig. 1), here we discuss how each cycle is unfolded in order to estimate the subgrain evolution which would be dealt with in the later part. As mentioned before there were four periods of stress relaxation during hold times, after each stress relaxation, the material behaves predominantly elastically. This behavior is reflected by a linear σ-ε_{mech} relation with slopes E. $E \approx$

190 GPa was used to determine the inelastic strain $\varepsilon_{inel} = \varepsilon_{mech} - \sigma / E$. Fig. 5 displays the cyclic stress-strain curve with inelastic strain plotted on the abscissa. The increase in absolute magnitude of inelastic strain during stress relaxation is now becoming apparent. The cumulative inelastic strain is defined as $\varepsilon_{inel,cum} = \int \left| d\varepsilon_{cyclic} \right|$ Fig. 6 shows the variation of the absolute magnitude of stress $|\sigma|$ with $\varepsilon_{inel,cum}$ during the cycle.

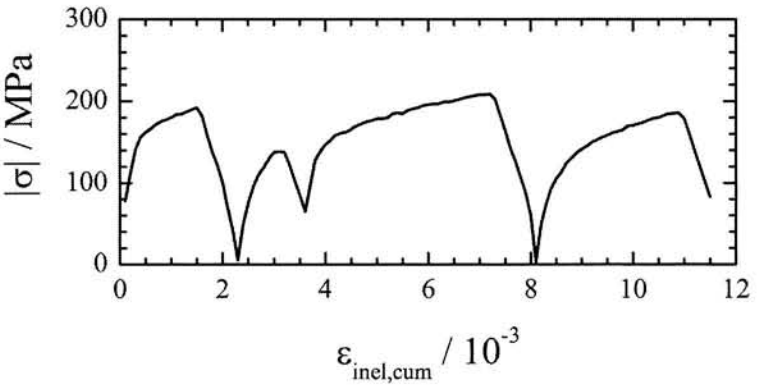

Figure 6: $|\sigma| - \varepsilon_{inel,cum}$ -curve of cycle of Fig. 1.

Subgrain size evolution

The initial dislocation structure of the specimen after quality heat treatment consists of subgrains of size $w_0 \approx 256$ nm [1] and 400 nm [2] for 1A and 2A, respectively. During deformation at a low constant value of stress σ the subgrain structure will coarsen with plastic strain [3] at the rate

$$\frac{d \log w}{d\varepsilon} = \frac{(-\log w - \log w_\infty)}{k_{\log w}} \qquad w_\infty = \frac{10bG}{\sigma} \qquad (1)$$

where, w_∞ is the steady state subgrain size, $k_{\log w}$ is a growth constant which was set to 0.12, $b = 0.248$ nm is the magnitude of the Burgers vector and $G =$ 63 GPa is the shear modulus at test temperature. Little is known about the behavior of the subgrain structure during alternating strain cycling. The final subgrain size w after cycling was determined by the line intersection technique as the average of subgrain intercept lengths w_i, measured from montages $i = 1,2...$ of TEM pictures. As seen in Fig. 7, the subgrain structure is slightly elongated.

For each montage measurements were done in the directions parallel and perpendicular to the elongation. Parallel test lines were drawn in each direction and the distance between the points of intersection between test line and subgrain boundaries was measured. The averages of these intercepts are the subgrain sizes in the directions parallel $w_i^{\parallel}$ and perpendicular $w_i^{\perp}$ to the direction of elongation in the investigated area A_i. For equi-axed subgrains, $w_i^{\parallel} = w_i^{\perp} = w_i$, it is known that $2/w_i$ represents the total area of boundaries within the prior austenite grains which is addressed as area of subgrain boundaries, without distinguishing between subspecies of subgrain boundaries like martensite colony boundaries (high angle),

martensite lath boundaries (low angle) and low angle boundaries within the laths. Therefore, in this case the boundary area can be expressed as

$$\frac{2}{w_i} = \frac{1}{w_i^{\parallel}} + \frac{1}{w_i^{\perp}} \qquad (2)$$

We extend this formula to the case where $w_i^{\parallel} \neq w_i^{\perp}$. It was checked that this value agrees to within 10% with the subgrain sizes determined previously [2] from test lines extending at an angle of about 45° to the direction of elongation. The volume average of the subgrain size is

$$w = \frac{1}{A}\sum_{i=1}^{N} A_i w_i \qquad A = \sum A_i \qquad (3)$$

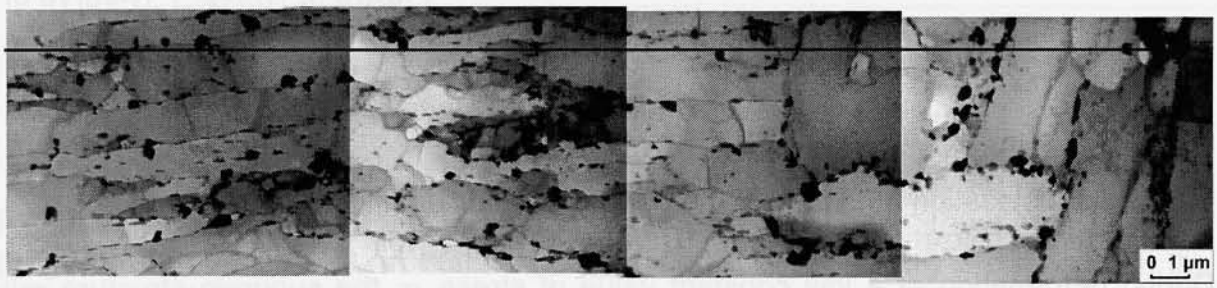

Figure 7: Montage of TEM Pictures of 1A after cyclic deformation displaying subgrains with a test line parallel to the direction of elongation

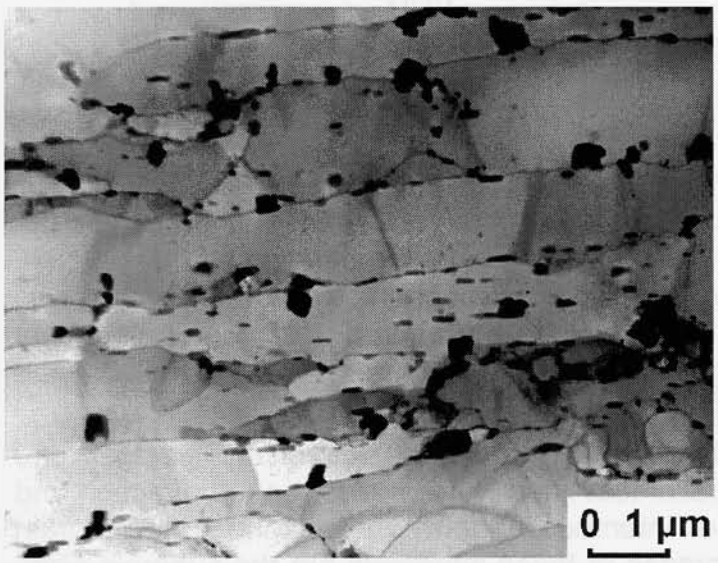

Figure 8: Detail from montage of Fig. 7.

The experimental error of w was quantified by the 95% confidence limit. The resulting subgrain size values for steel 1A from a total investigated area $A =$ 2162 µm² is $w = (1.54 \pm 0.24)$ µm with an aspect ratio $w_i^{\parallel} / w_i^{\perp} =$ 1.5 and for steel 2A from a

total investigated area $A =$ 1731 µm² is $w = (1.54 \pm 0.23)$ µm, with an aspect ratio $w_i^{\parallel} / w_i^{\perp} =$ 1.4.

The subgrain size after cyclic deformation can be estimated from the stress-strain curves. The simplest estimate is based on the assumption that the subgrain size adjusts to the steady state value which would be observed at the maximum stress σ_{max} occurring within the cycle, σ_{max} changes from cycle to cycle. From (1) for steel 1A one gets $w(\sigma_{max}) =$ 780 nm. This value is expected to be a lower bound, because the periods with smaller stresses and the changes in direction of straining during the cycles have been neglected. The expectation is confirmed by the experimental data (Fig. 9). A better estimate was made by numerically integrating eq. (1) over all cycles of $|\sigma|$ with $\varepsilon_{inel,cum}$ (Fig. 6 represents an individual one) for steel 1A. From the evolution of peak stress and three given cycle shapes ($i = 1$, 100, 1000) the evolution of the cycle shapes was interpolated on the whole range of cycles. The resulting evolution of w with $\varepsilon_{inel,cum}$ is shown in Fig. 9.

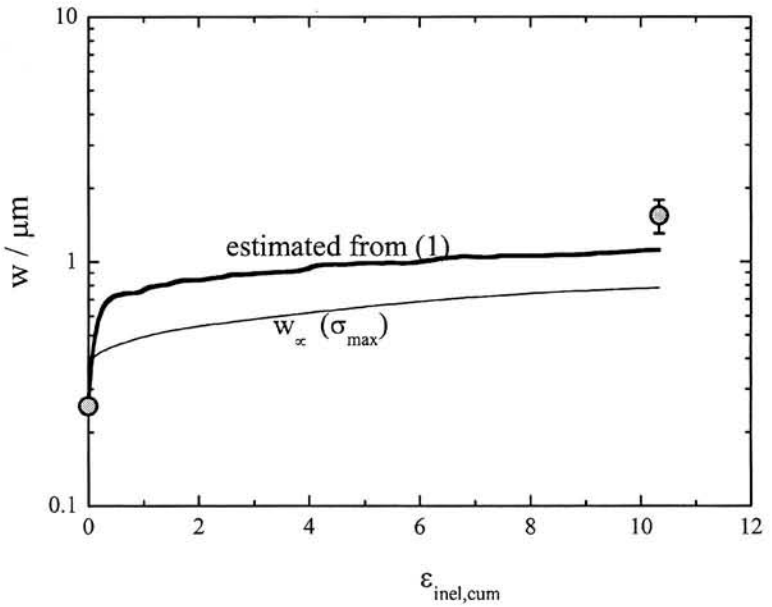

Figure 9: Subgrain size as a function of cumulative strain $\varepsilon_{inel,cum}$ of 1A.

Starting from the initial value $w_0 =$ 256 nm for the 1A the rate at which w increases is high in the initial cycles and tends to saturate as cycling progresses, resulting in $w =$ 1115 nm which is less than the experimental value. The difference between the curves estimated form eq. (1) and the $w_\infty(\sigma_{max})$ in Fig. 9 reflects the influences of stress relaxation and stress reversals. Similar behavior was observed in the 2A [4].

Effect of cycling on creep due to subgrain coarsening

The transmission electron microscopic results show that cyclic deformation leads to substantial coarsening of subgrains from 256 nm to (1.54 ± 0.24) µm for 1A and from

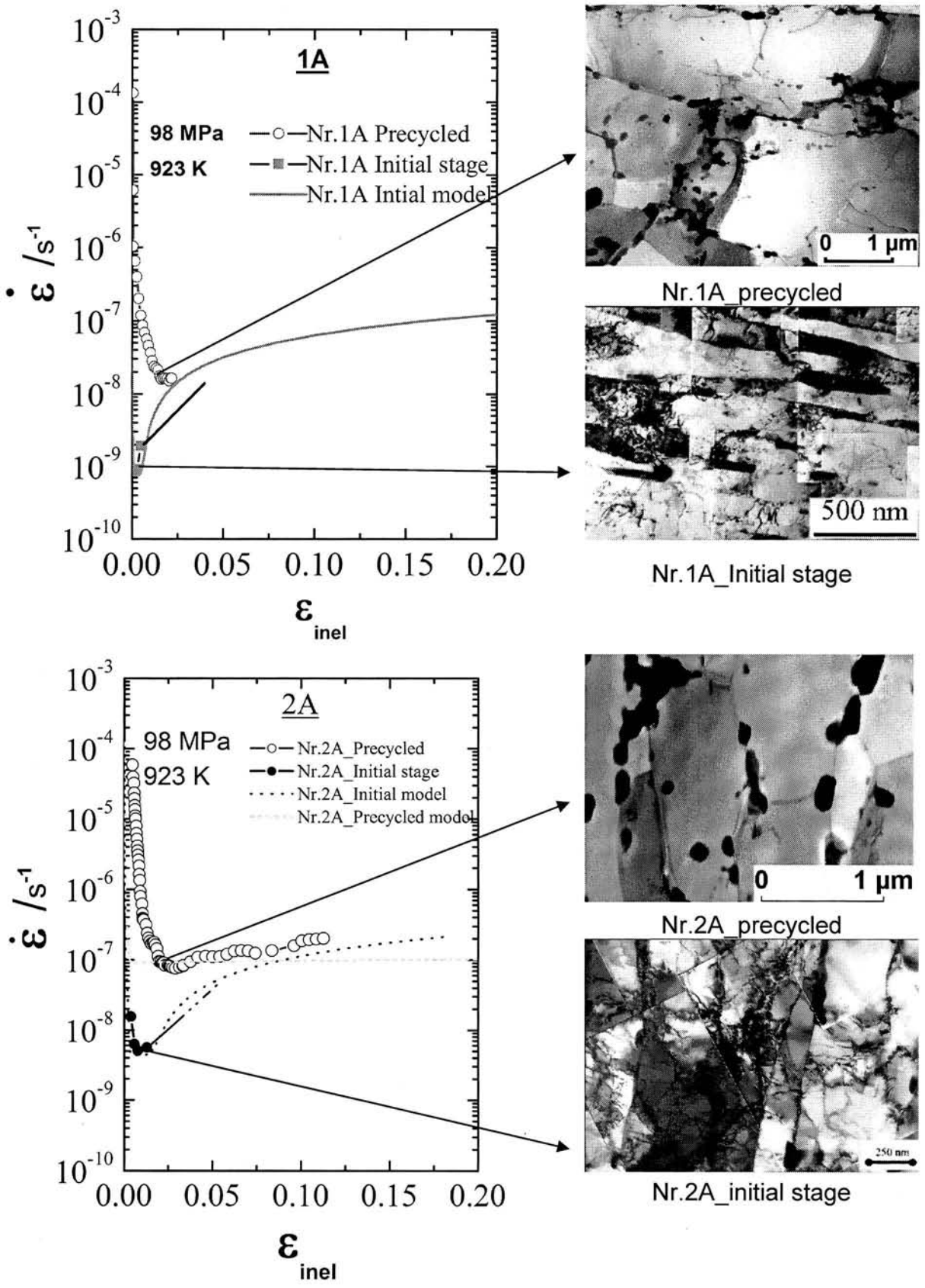

Figure 10: Compressive creep rate $\dot{\varepsilon}$ as function of strain ε_{inel} for 1A and 2A with and without prior cyclic deformation with the subgrain structures before the start of the creep test

400 nm to (1.54 ± 0.23) µm in 2A within a relatively short period of time. The corresponding subgrain growth is the probable source of the observed cyclic softening. This is supported by the fact that both the growth and the softening decrease in rate during cycling.
In order to check the effect of subgrain coarsening due to cyclic deformation on creep and to check results obtained from TEM investigation a compression creep test was performed on the cyclically deformed specimens of 1A and 2A.
According to (1) there will be no subgrain coarsening, if the cyclically deformed specimen is crept under a stress of 98 MPa, because the steady state subgrain size at that stress equals the subgrain size in the cyclically deformed specimen. Fig. 10 shows the $\dot{\varepsilon}-\varepsilon$ - curve of the cyclically deformed specimen measured at 923 k together with the modeled curves using composite model [1] for the precycled specimens and modified Garofalo creep equation reported by Berger et al. [5] for specimens with the initial stage subgrain sizes of 256 nm (Nr.1A) and 400 nm (Nr.2A) resulting from the quality heat treatment. In both cases the curves with the initial stage microstructures display a pronounced minimum in $\dot{\varepsilon}$, whereas in the precycled curves a relative minimum in $\dot{\varepsilon}$ is nearly absent.

The minimum of $\dot{\varepsilon}$ is interpreted to result from subgrain coarsening. Consistent with that, the lack of a pronounced relative $\dot{\varepsilon}$ -minimum in the other curve indicates that virtually no subgrain coarsening is necessary. TEM measurements on the crept specimen which has been precycled prior to the test reveals a decrease in aspect ratio $w_i^{\parallel} / w_i^{\perp}$ of the subgrain structure, without a significant change in the width of subgrains. This decrease in the aspect ratio suggests that the subgrain structure rearranges during creep leading to the faint minimum of $\dot{\varepsilon}$. Factors leading to this faint $\dot{\varepsilon}$ minimum are to be fully understood. Same effect has been observed previously, where $w_0 \approx w_\infty$ [1]. Thus, the results of the creep test on the cyclically deformed specimens with coarsened subgrain structure are consistent with the TEM observation. The effect of precipitates on degradation of creep is insignificant, according to Götz et al. [7] negligible coarsening of the precipitates is expected in the course of cyclic deformation at 600°C, more over fresh precipitation of tungsten based laves phase is expected, owing the degradation of creep resistance to subgrain coarsening.

Both estimates of the cyclic steady state subgrain size based on $w(\sigma_{\max})$ as well as eq. (1) yield values which are distinctly smaller than the measured one. The probable reason is that the change in the direction of dislocation motion during each cycle has been neglected. As the stress changes from tension to compression and back the dislocations stop and continue moving in the opposite direction. This backward motion may cause significant recovery of the dislocation content in subgrain [8]. Such extra recovery due to cycling may lead to enhanced subgrain growth.
The results show that there is clearly an interaction between cyclic deformation and creep (creep-fatigue interaction) causing degradation of the creep resistance by prior cyclic deformation leading to enhanced subgrain growth.

Summary

Cyclic strain-controlled alternating tensile-compressive deformation at 873 K with stress relaxation during hold times causes significant growth of subgrains. The subgrain coarsening degrades the creep resistance by increasing the minimum compressive creep rate at 923 K and 98 MPa by a factor of 15, lifting it close to the steady state creep rate. The interaction between cyclic loading and creep is expected to cause deviations from the linear damage accumulation rule.

Acknowledgements

Thanks are due to the Deutsche Forschungsgemeinschaft and the consortium of BMWA and industry within the project DT1/2 for financial support.

References

[1] P. Polcik. Modellierung des Verformungsverhaltens der warmfesten 9-12% Chromstähle im Temperaturbereich von 550_650°C. D29 (Dissertation Universität Erlangen-Nürnberg). Shaker Verlag, Aachen, 1999.
[2] Y. Qin, G. Götz, and W. Blum. Subgrain structure during annealing and creep of the cast martensitic Cr-steel G-X12CrMoWVNbN 10-1-1. Mater. Sci. Eng. A, 41:211–215, 2003.
[3] S. Straub, T. Hennige, P. Polcik, and W. Blum. Microstructure and Creep Rate during Long-Term Cyclic Creep of the Martensitic Steel X22 CrMoV 12 1. Steel Research, 66:394–401, 1995.
[4] H. Chilukuru, M. Schwienheer, A. Scholz, and W. Blum. Subgrain coarsening in tempered martensite steel X12CrMoWVNbN10-1-1 due to cyclic deformation. In S.L.Mannan, editor, Proc. 4th Conference on Creep, Fatigue and Creep-Fatigue Interaction, Kalpakkam, India, 2003.
[5] C.Berger, A. Scholz, and M. Schwienheer Ermittlung der Gebrauchseigenschaften der 600°C-Stähle, Teilprojekt Kriech-, Dehnwechsel- und Kerbverhalten. Technical report, BMWi-PTJ-Verbundvorhaben, Förderkennzeichen 0327053, Inst für Werkstoffkunde, TU Darmstadt, 2002.
[7] G. Götz, Y. Qin, and W. Blum. Investigation of precipitation in cast martensitic annealed steel X12 CrMoVWNbN 10-1-1 by semiautomatic EDX-analysis in the scanning transmission electron microscope. In R. Viswanathan, W. Bakker, and J. D. Parker, editors, Advances in materials technology for fossil power plants, Proc. of the 3rd Conference held at University of Wales Swansea, 5th April - 6th April 2001, pages 155-163, London, 2001. The Institute of Materials.
[8] T.Hasegawa and T.Yakou Mater. Sci. Eng. 20 (1975) 267-276.
[9] K. H. Kloos, J. Granacher und A. Scholz. Mehrstufige betriebsähnliche Dehnwechselbeanspruchung warmfester Stähle, Mat.-wiss. u. Werkstofftech. 27 (1996) S. 331/37.

C Publication [19]

Modelling the Influence of Microstructure on Creep Strength of G-X12CrMoWVNbN 10-1-1

X. H. Zeng and W. Blum

In *29th MPA Seminar, Safety and Reliability in Energy Technology, Oct 2003*, Stuttgart, 2003.

Modelling the Influence of Microstructure on Creep Strength of GX12CrMoWVNbN 10-1-1

X.H. Zeng, W. Blum
Institut für Werkstoffwissenschaften LS1
Universitt Erlangen-Nürnberg, Martensstrae 5, 91058 Erlangen
Tel: 09131 8527507, Fax: 09131 8527504
e-mail: xiaohui.zeng@ww.uni-erlangen.de, wolfgang.blum@ww.uni-erlangen.de

13. August 2003

1 Modelling Results and Discussions

The tempered martensitic GX12CrMoWVNbN 10-1-1 has fine lath structure and gains its high temperature creep strength with the hardening effect of precipitates (MX, $M_{23}C_6$ and Laves phase in this material), subgrain and solute atom. However, the hardening effect caused by these factors are not simply superimposed. In the present work, the composite model is used to analyze the hardening effects by subgrain size and precipitates.

1.1 Influence of the Initial Subgrain Size on Creep Strength

In the present work, two simulations were made with the same condition expect different initial subgrain size. The microstructure investigations were shown in Fig. 2. The lower part of the figure corresponds to the material after quality heat treatment, the average sugrain size is 411 nm. The upper part of the figure corresponds to the same material but after 724 cycles strain controlled deformation, the subgrain coarsens to a quite value, 1500 nm [1]. The comparison was made in Fig. 1. Obviously the model did not give a satisfied absolute result comparing with the test at this low stress, however, it reflected the difference of the $\dot{\epsilon}$-ϵ curves caused by different initial subgrain size rather well. and it confirmed, that in martensitic steels, the finer the subgrain size is, the stronger the steel gains its high temperature creep strength.

1.2 Influence of the Precipitates on Creep Strength

In the following work, the mathematically creep tests were done at: 185 MPa, 873K and 10^7 s deformation. The initial subgrain size is 411 nm, the initial mean size of MX , $M_{23}C_6$ and

Laves-phase are 54 nm, 90 nm and 100 nm, respectively [2]. In this section, one simulation with considering all three kinds of precipitates was made at the above mentioned condition, Fig. 3. For convenient, such simulation was named as full version simulation. In the following section, in order to reveal the influence of each kind of precipitate, the studied object, e.g. MX, was cancelled from the model on purpose while the influence of the other two kinds of precipitates were remained.

1.2.1 MX

MX (platelike VN, spherical Nb(C,N)) forms and remains in the microstructure during heat treatment. Its volume fraction and mean size does not change significantly in this material and some other 9-12Cr steel after creep deformation [3, 4, 5, 6, 7] below 923K. Many authors [7, 8, 9] have confirmed that this intragranularly precipitated particle, because of its fine distribution and stability, significantly contributes to high temperature creep strength. In order to reveal the MX hardening effect, A new simulation was made but the effect of MX was cancelled on purpose. In the full version simulation, after deformation, the mean size of MX coarsened from the initial value to 55 nm (only 1 nm difference to the initial value). Comparing Fig. 3 with Fig. 5, one can see a quite large strain rate increases (by a factor of 10) when the MX was cancelled. Meanwhile, in the primary creep, it is clear that the strong strain rate decrease can not be only interpreted by the sharp dislocation density decreasing, obviously the MX hardening plays an important role also.

Another evidence of MX particle strength came from the work of Sawada et al. [10], their study indicates, in 9Cr-0.5Mo-1.8W-VNb steel, the strengthening effects of MX disappear at short time at 1023 K due to the particles rapid coarsening during creep. Hamada et al. [8, **?**] reported that so-called V-Wing (Nb(C,N)+V(C,N)) shape MX particle in P92 and E911 steel has stronger ability to pin mobile dislocations and restrains dislocations pile-up on grain boundary than the platelike and spherical MX, so it contributes more strengthening effect.

1.2.2 $M_{23}C_6$

$M_{23}C_6$ is mainly precipitated on prior austenite grain boundaries and martensite lath boundaries. That means the volume fraction of this particle entering the expression of Orowan stress in hard region should be local volume fraction instead of average volume fraction [11]. The coarsen procedure was assumed to obey Ostwald ripening rule during creep deformation. As in the former section, a similar comparison was made to reveal the influence of $M_{23}C_6$ ($M_{23}C_6$ was cancelled in the second simulation). The result was shown in Fig. 7. Comparing Fig. 7 with Fig. 3, very slight increase of minimum strain rate and decrease of slope after minimum strain rate in the most upper part of the two figures can be found. It means, based on Orowan mechanism, the hardening effect of $M_{23}C_6$ is significant less than of MX. So $M_{23}C_6$ might not contribute to creep strength directly, instead it may retard subgrain coarsening by pinning martensitic lath boundaries (It should be noted that the retardation does not affect the steady state subgrain size) [7, 8, 9]. If this is true, how to establish the relationship between $M_{23}C_6$ and subgrain coarsening rate (k_w in the current model) would be expected in the future work. The stress $\sigma_p s$ caused by $M_{23}C_6$ was separated from

Fig. 3 was shown in Fig. 8, the result shows, after reaching its maximum value, the stress decrease with the particle coarsening.

1.2.3 Laves-Phase

Laves phase (Fe_2(Mo, W)) mainly precipitated on prior austenite grain boundaries and martensite lath boundaries. It precipitates and coarsens during creep deformation. A similar comparison was made to reveal the influence of this particle as before. The result was shown in Fig. 9. Comparing Fig. 9 with Fig. 3, there is nearly no difference that can be found. The stress caused by it was shown in Fig. 10. Up to now Whether or not Laves-phase has a hardening effect on creep property is still in controversy. Ishii et al. [**?**] suggested Laves-phase on grain boundaries reduces efficiency of grain boundary as a sink of dislocations and suppresses recovery of dislocation at grain boundaries, however, [**?**] suggested that the precipitation of Laves phase reduces creep strength because of the depression of the solute hardening by W. The work of Sawada et al. [12] showed the precipitation of Laves phase on the lath boundaries has the effect to pin the subgrain boundaries, however, those precipitation on grain boundaries not. The hardening effect of Laves-phase need to be studied in the future work.

1.3 Comparison between Empirical Model and Composite Model

A systematical comparison was made between this composite model and a modified Garofalo creep equation reported by [13]. From b) of Fig. 11, one can see the composite model gave quite good result with stress above 100 MPa and with temperature below 923K. At low stress, the calculated minimum strain rate was obviously lower than experimental data. This might be due to that attractive interaction between free dislocations and precipitates dominates at low stress **??**.

2 Conclusion

Literatur

[1] H. Chilukuru, M. Schwienheer, A. Scholz, and W. Blum. Subgrain coarsening in tempered martensite steel X12CrMoWVNbN10-1-1 due to cyclic deformation. In S.L. Mannan, editor, *4th Conference on Creep, Fatigue and Creep-Fatigue Interaction, Kalpakkam, Indien*, 2003.

[2] G. Götz. 2002.

[3] Y. Qin, G. Götz, and W. Blum. Subgrain structure during annealing and creep of the cast martensitic Cr-steel G-X12CrMoWVNbN 10-1-1. *Mater. Sci. Eng. A*, 341, 2003.

[4] Y. Qin. Microstructure Evolution of The Cast Martensitic Steel G-X12CrMoWVNbN 10-1-1 During Creep at 823 K. *Mater. Sci. Eng. A*, 357:1–6, 2003.

[5] R. Agamennone and W. Blum. Martensitic/ferritic super heat-resistant 650°C steels – Experimental investigation and modelling. 2003.

[6] G. Götz and W. Blum. Influence of thermal history on precipitation of hardening phases in tempered martensite steel of type X12CrMoWVNbN10-1-1. *Mater. Sci. Eng. A*, 2002.

[7] P. J. Ennis and A Czyrska-Filemonowicz. Recent Advances in Creep Resistant Steels for Power Plant Applications. *OMMI*, 1:1–28, 2002.

[8] K. Hamada, K. Tokuno, Y. Tomita, H. Mabuchi, and K. Okamoto. Effects of Precipitate Shape on High Temperature Strength of Modified 9Cr-1Mo Steels. *ISIJ Int.*, 35:86–91, 1995.

[9] G. Eggeler. The Effect of Long-Term Creep on Particle Coarsening in Tempered Martensitic Ferritic Steels. *Acta Metall.*, 37:3225–3234, 1989.

[10] K. Sawada, K. Kubo, and Abe. F. Creep Behavior and Stability of MX Precipitates at High Temperature in 9Cr-0.5Mo-1.8W-VNb Steel. *Mater. Sci. Eng. A*, 319-321:784–787, 2001.

[11] R. Agamennone, W. Blum, Y. Wang, and A. Scholz. Deterioration of creep resistance at 650°c by precipitation of Z-phase in martensitic tempered steels with 2 mass-% W. *Mater. Sci. Eng. A*, to be submitted.

[12] K. Sawada, M. Takeda, K. Maruyama, R. Ishii, M. Yamada, Nagae Y., and R. Komine. Effect of W on Recovery of Lath Structure During Creep of High Chromium Martensitic Steels. *Mater. Sci. Eng. A*, 267:19–25, 1999.

[13] C. Berger, A. Scholz, and M. Schwienheer. Ermittlung der Gebrauchseigenschaften der 600°c-Stähle, Teilprojekt Kriech-, Dehnwechsel- und Kerbverhalten. Technical report, BMWi-PTJ-Verbundvorhaben, Förderkennzeichen 0327053, Inst. f. Werkstoffkunde, TU Darmstadt, 2002.

[14] B. Garofalo. *Fundamentals of Creep and Creep Rupture*. McMillan, New York, 1965.

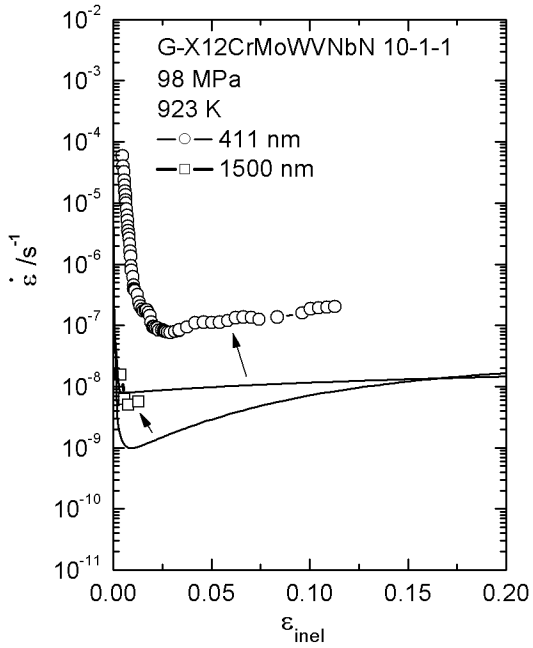

Fig 1: The $\dot{\epsilon}$-ϵ curve with the initial subgrain sizes of (tempered 411) nm and 1500 nm (cyclic deformed).

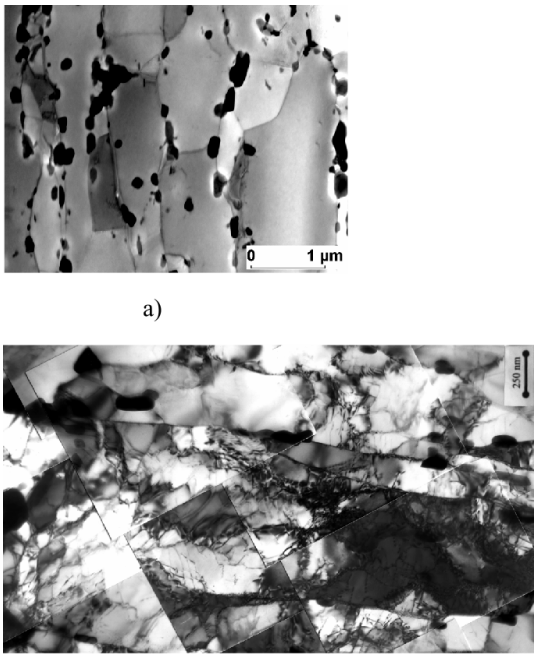

a)

b)

Fig 2: The microstructure of the subgrain with the size of a) 1500 nm and b) 411 nm

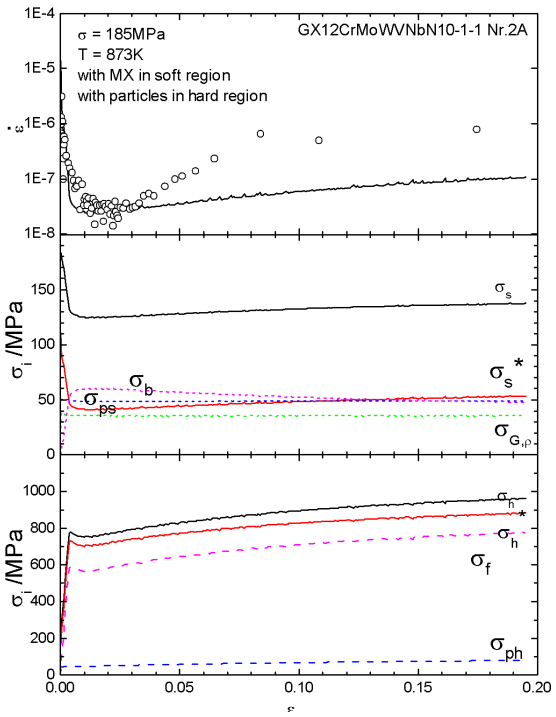

Fig 3: A full version precipitate hardening calculation. The corresponding microstructure evolution result was shown in Fig. 4.

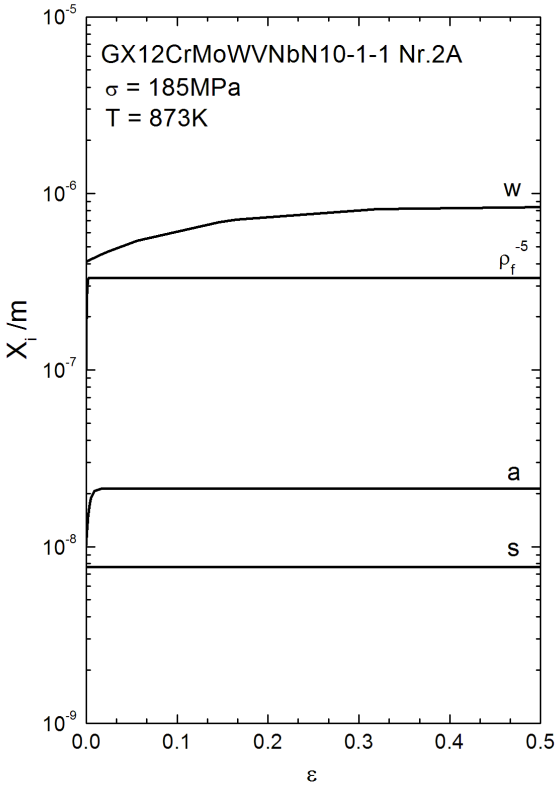

Fig 4: Microstructure evolution

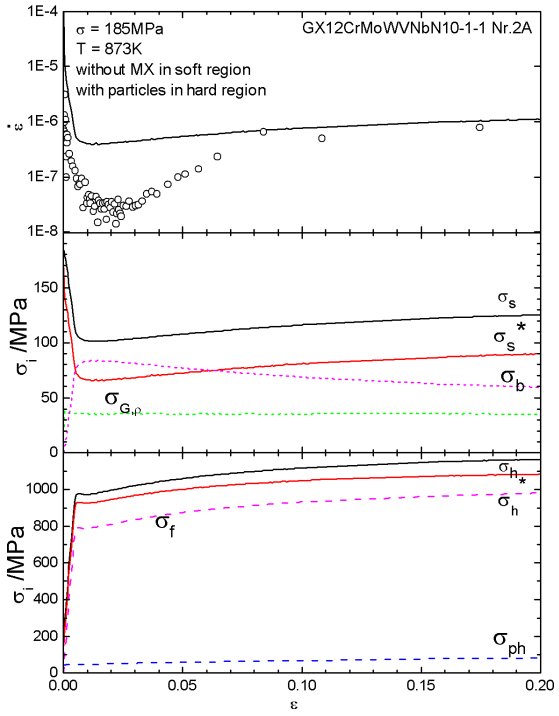

Fig 5: MX particle was cancelled in this calculation, the effective stress, $\sigma_s{}^{\star}$, in soft region is larger than that in Fig. 3.

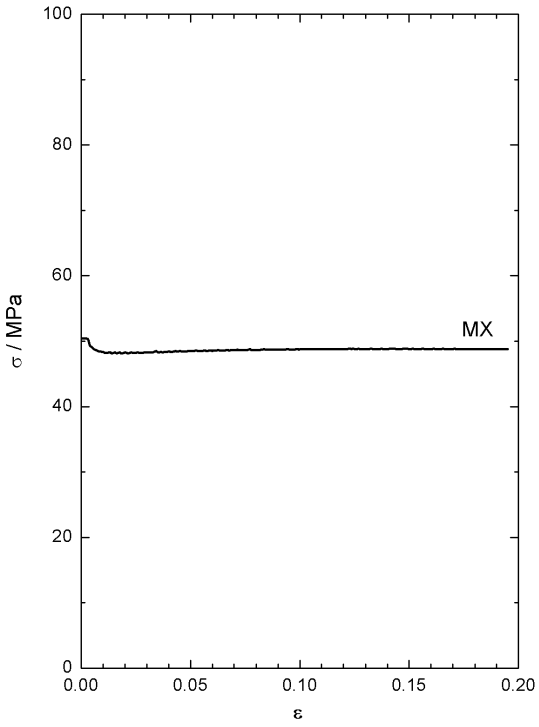

Fig 6: stress caused by MX based on Orowan mechanism.

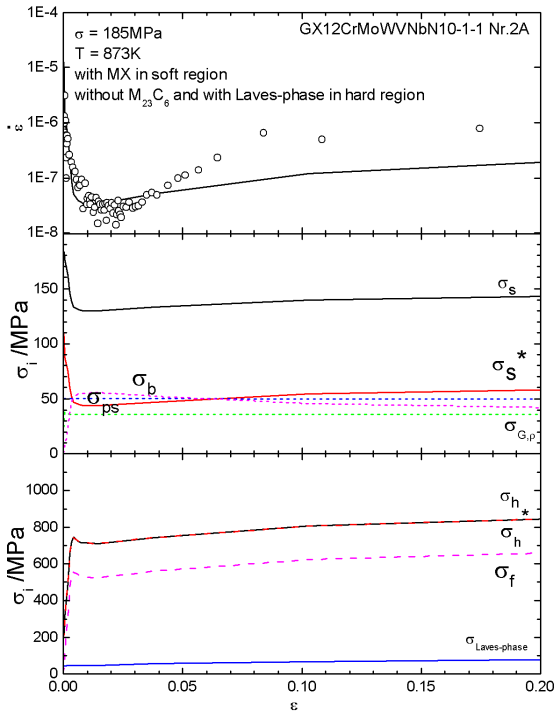

Fig 7: Cancelled the effect of $M_{23}C_6$

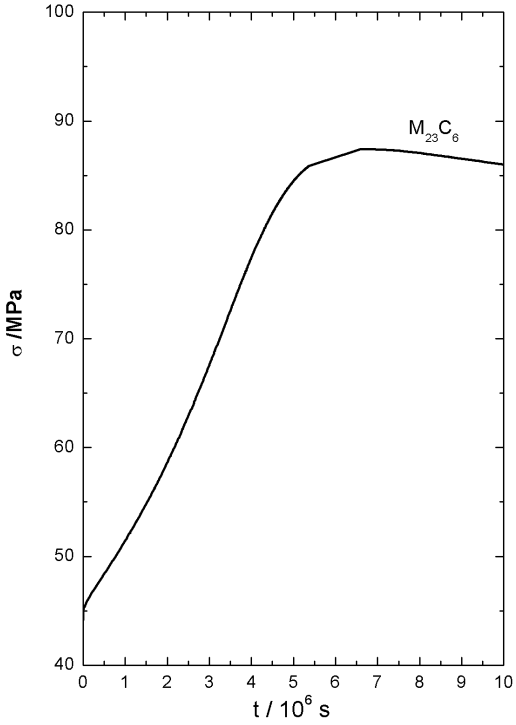

Fig 8: stress caused by $M_{23}C_6$ based on Orowan mechanism

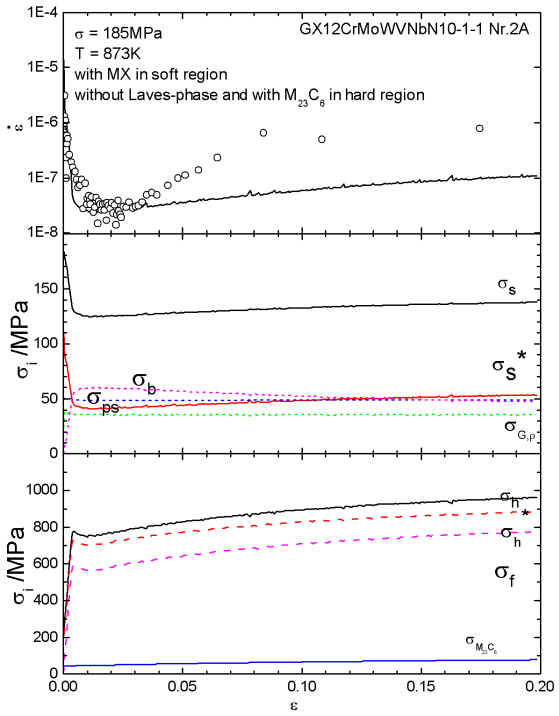

Fig 9: Cancelled the effect of Laves-phase

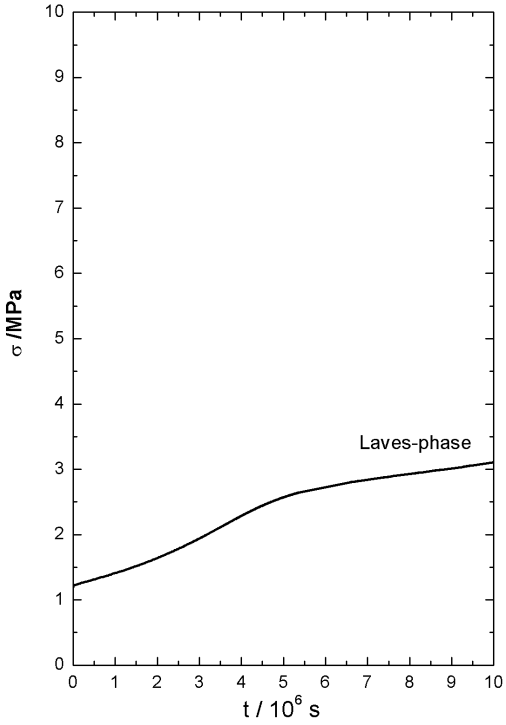

Fig 10: stress caused by Laves-phase based on Orowan mechanism

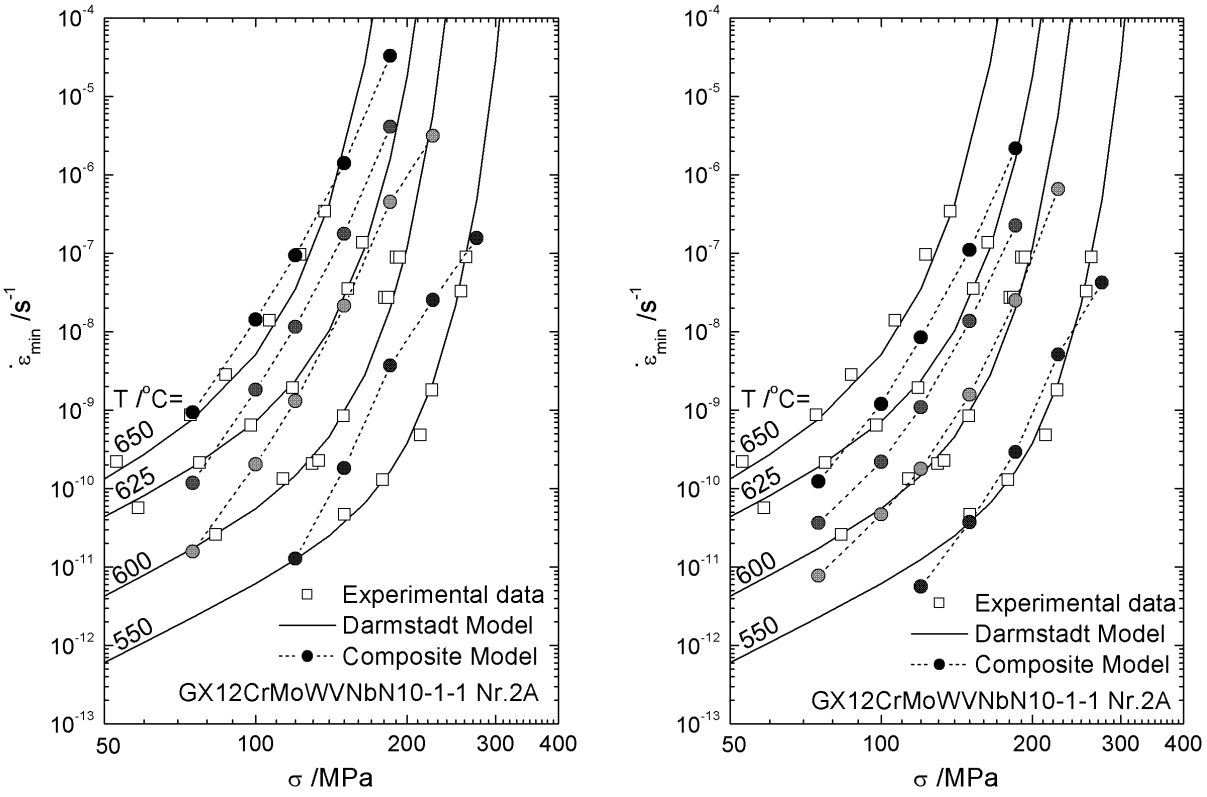

(a) Without MX

(b) With all particles

Fig 11: Comparison between Empirical Model([13, 14].) and Composite Model(MIKORA)

D Publication [11]

Effects of cyclic deformation on subgrain evolution and creep in 9-12% Cr-steels

J.S. Dubey, H. Chilukuru, J.K. Chakravartty, M. Schwienheer, A. Scholz, and W. Blum

Materials Science and Engineering A, 406:152-159, 2005.

Materials Science and Engineering A 406 (2005) 152–159

www.elsevier.com/locate/msea

Effects of cyclic deformation on subgrain evolution and creep in 9–12% Cr-steels

J.S. Dubey[a], H. Chilukuru[b,*], J.K. Chakravartty[a], M. Schwienheer[c], A. Scholz[c], W. Blum[b]

[a] *Materials Science Division, Bhabha Atomic Research Center, Mumbai 400085, India*
[b] *Institut für Werkstoffwissenschaften, LS 1, Universität Erlangen-Nürnberg, Martensstaße 5, 91058 Erlangen, Germany*
[c] *Institut für Werkstoffkunde, Technische Universität Darmstadt, Grafenstr. 2, 64283 Darmstadt, Germany*

Received in revised form 9 June 2005; accepted 10 June 2005

Abstract

Power plant components from modern 9–12% CrMoV-steels having fine precipitate stabilized subgrain structure undergo cyclic deformation as well as creep during service. The present work studies changes in subgrain structure due to cyclic straining and their effects on the creep behaviour in 12CrMoWVNbN10-1-1 steel. It was found that the cyclic plastic straining causes significant coarsening of the subgrain structure. Presence of hold periods during deformation significantly increases the extent of coarsening. Evolution of subgrain structure during cyclic deformation has been treated by extending the phenomenological law known from creep. Subgrain coarsening induced by cyclic deformation leads to significant increase in the resistance against creep.

Keywords: 9–12% Cr-steels; Subgrains; Dislocations; Hold periods; Cyclic deformation; Creep

1. Introduction

9–12% Cr-steels inherit their creep strength from combination of hardening mainly by subgrains and carbide/carbonitride precipitates [1,2]. Modern 9–12% CrMoVWNbN-steels with superior creep strength in comparison to conventional steels of type X20(22)CrMoV are good candidate materials for fabrication of components used in power plants [3–5].

The subgrain and precipitate structures may change due to the exposure to elevated temperature and stresses during service. It has been found that the subgrain structure in tempered martensitic steels approaches a steady state in the course of unidirectional deformation at elevated temperature, e.g. creep. As for many other materials, the steady state subgrain size w_∞ of tempered martensitic steels can be expressed as a function of stress σ [6–9]:

$$w_\infty \approx 10\,\frac{bG}{\sigma} \tag{1}$$

where $b = 0.248$ nm is the length of the Burgers vector and G is the shear modulus. The precipitate structure changes as function of time at elevated temperature by precipitation, coarsening of precipitates, possibly also by exchange of existing precipitates for more stable ones [1,7,10–14].

It is important to understand these microstructural changes and their effects on the creep behaviour. Of special relevance is the effect of cyclic loading which is commonly found under service conditions. In the present work we examine the changes of the dislocation structure due to cyclic straining and their effects on the creep behaviour in 12CrMoWVNbN10-1-1 steel.

2. Experimental

Materials 1A and 2A used in this study are forged and cast variants of the steel X12CrMoWVNbN10-1-1 (German

* Corresponding author. Tel.: +49 9131 8527478; fax: +49 9131 8527504.
E-mail address: hemambar.chilukuru@ww.uni-erlangen.de (H. Chilukuru).

0921-5093/$ – see front matter © 2005 Published by Elsevier B.V.
doi:10.1016/j.msea.2005.06.029

Table 1
Chemical compositions in mass %

Steel	C	Si	Mn	B	Cr	Mo	N	Nb	W	V
1A	0.12	0.10	0.42	–	10.7	1.04	0.056	0.05	1.04	0.16
2A	0.13	0.29	0.82	0.0005	9.51	1.02	0.041	0.059	1.02	0.19

Table 2
Heat treatments

Steel	Austenitization		Temper 1		Temper 2	
	T(°C)	t (h)	T(°C)	t (h)	T(°C)	t (h)
1A	1050	7	570	10.25	690	10
2A	1070	12	730	10	730	10

designation), respectively. Their chemical compositions are given in Table 1. The initial heat treatments consist of an austenitizing anneal and two-stage tempers (Table 2).

Cylindrical specimens with 10 mm diameter and 25 mm gage length were used for cyclic deformation at 873 K and constant amplitude $\Delta\epsilon_{mech} \approx 0.65\%$ of mechanical strain $\epsilon_{mech} = \epsilon_{el} + \epsilon_{inel}$ (ϵ_{el}, elastic strain; ϵ_{inel}, inelastic strain) in a servo-hydraulic machine. Specimen designations and details of cyclic deformation are shown in Table 3.

Compressive creep tests were performed at 923 K with a kinked lever arm type machine to maintain constant stress σ during test. Specimens having 5 mm × 5 mm cross-section and 6 mm height were tested under compression to observe the creep behaviour. Changes in specimen height during test were measured with three displacement transducers placed in circular symmetrical arrangement around the specimen to get an averaged reading and minimize errors. Load and displacement data were continuously recorded with a data acquisition system.

Tensile creep tests were performed at constant load. $\dot{\epsilon}_{inel}$ was determined in the primary and secondary stages of creep as $\Delta\epsilon/\Delta t$ (t, time) and in the tertiary stage by interpolation of the strain–time data [7,15] on the basis of exponential increase of $\dot{\epsilon}_{inel}$ with ϵ_{inel} and subsequent correction of $\dot{\epsilon}_{inel}$ for constant stress σ assuming $\sigma = \sigma_0 \exp(\epsilon_{inel})$ and $\dot{\epsilon}_{inel} \propto \sigma^n$ (σ_0, initial stress at $\epsilon_{inel} = 0$ and $n = 9$).

Transmission electron microscopic (TEM) investigations were performed following the procedures described previously [16]. The subgrain sizes w were determined by the line intersection technique as average of subgrain intercept lengths w_i (i = 1, 2, ...) measured from montages of TEM pictures (see [17] for details). The average spacing of free dislocations in the interior of subgrains is characterized through their density ρ_f as $\delta = \rho_f^{-0.5}$. The statistical experimental error in measurement of spacings was quantified by the 95% confidence limit of the average values determined for different samples of the microstructure of a given state.

Table 3
Specimen designation (NH, no hold periods; 2H, two hold periods; 4H, four hold period) and details of cycling at 873 K until crack initiation was detected at cycle no. N_i and time t (t_{HT}, hold time in tension; t_{HC}, hold time in compression)

Specimen	$\Delta\epsilon_{mech}$ (%)	N_i	t (h)	t_{HT} (h)		t_{HC} (h)	
				H_1	H_4	H_2	H_3
1A-NH	0.65	3513	13	0	0	0	0
1A-2H	0.65	1491	154	0.05	0	0	0.05
1A-4H	0.65	1119	11192	1.5	7.0	0.75	0.75
2A-4H	0.70	724	2317	0.5	2.2	0.25	0.25

3. Results

3.1. Cyclic deformation

Fig. 1 shows $\sigma - \epsilon_{mech}$ cycles no. $N = 1$, 100 and 1000 of specimen 1A-4H. In each cycle there are four loading portions R_i (i = 1–4) and four hold periods H_i, two of them in tension and two in compression. The cycling leads to significant softening as manifested by decrease in peak tensile and compressive stresses with N (Fig. 2). The rate of decrease of peak stress reduces rapidly as cycling is continued. These effects are related to the decelerating concomitant subgrain coarsening reported below.

The inelastic strain ϵ_{inel} was obtained from the mechanical strain ϵ_{mech} by subtracting the elastic strain $\epsilon_{el} = \sigma/E$. Young's modulus E was taken as slope of the linear loading portion of ramp R_1. This choice is not critical as the modulus values for different ramp portions of any given cycle vary only within a small range (e.g. 155–157 GPa in cycle 100 in Fig. 1). The experimental values of the (static) modulus E are consistent with the dynamic modulus $E_{dyn} = 169$ GPa of the CrMoV-steel X20CrMoV121 at 873 K reported by Straub [8]. From the increments of ϵ_{inel} the cumulative cyclic inelastic strain $\epsilon_{inel,cum} = \int |d\epsilon_{inel}|$ was calculated. It increases during all phases of the cyclic test as exemplified in Fig. 3.

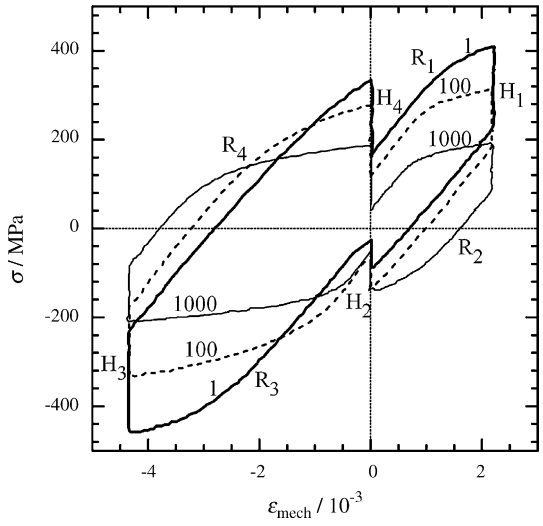

Fig. 1. $\sigma - \epsilon_{mech}$ at cycles no. $N = 1$, 100 and 1000 of specimen 1A-4H; R_1–R_4, periods of deformation at constant $\dot{\epsilon}_{mech} = 10^{-3}\ s^{-1}$; H_1–H_4, hold periods with relaxation of σ at constant $\epsilon_{mech} = 0$ (H_2, H_4) and at peak values of ϵ_{mech} (H_1, H_3).

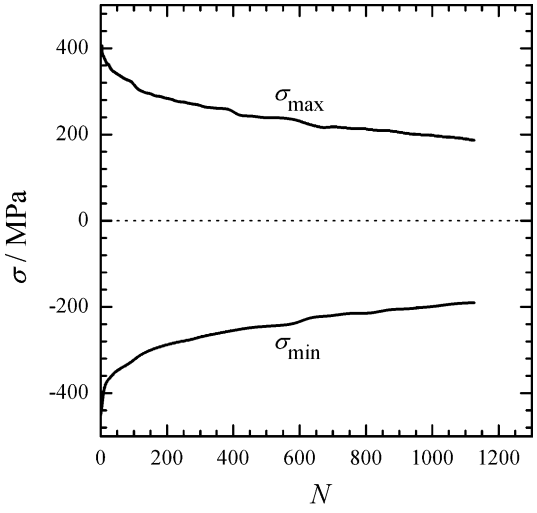

Fig. 2. Decrease of tensile peak stress σ_{max} and compressive peak stress σ_{min} with number N of cycles for specimen 1A-4H until crack initiation at $N_i = 1119$.

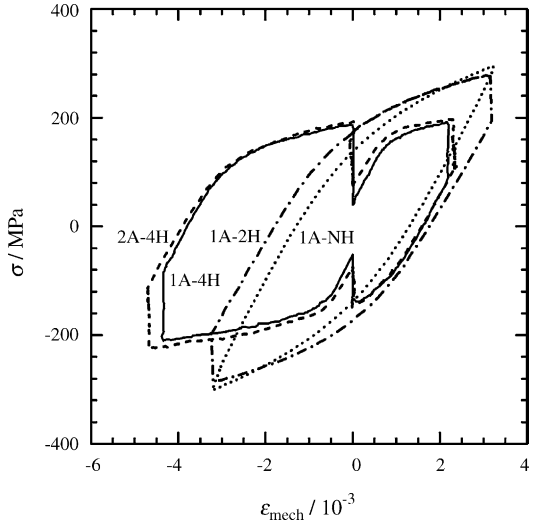

Fig. 4. $\sigma - \epsilon_{mech}$ cycles for 1A-4H, 1A-2H, 1A-NH and 2A-4H in later half or near end of cyclic tests.

Fig. 4 compares the $\sigma - \epsilon_{mech}$ cycles of the different specimens in a late state of the cyclic test where progress of softening has become slow. For the cyclic treatments 1A-4H and 2A-4H with hold periods one observes quite similar cycles. For treatment 1A-NH without hold periods the stress amplitude is higher than in the former case, as hold periods with relaxation of stress are lacking. The similarity between the cycles of 1A-2H and 1A-NH is related to the fact that 1A-2H has no hold periods with reduction of stress level due to relaxation at $\epsilon_{mech} = 0$ in contrast to 1A-4H.

3.2. Dislocation structure

In the initial state after tempering of martensite the dislocation structure is characterized by the subgrain sizes $w_0 = 256$ nm in 1A and 411 nm in 2A [18,19,16]. The initial spacing δ_0 of free dislocations in the subgrain interior after tempering lies in the order of 100 nm [20,21].

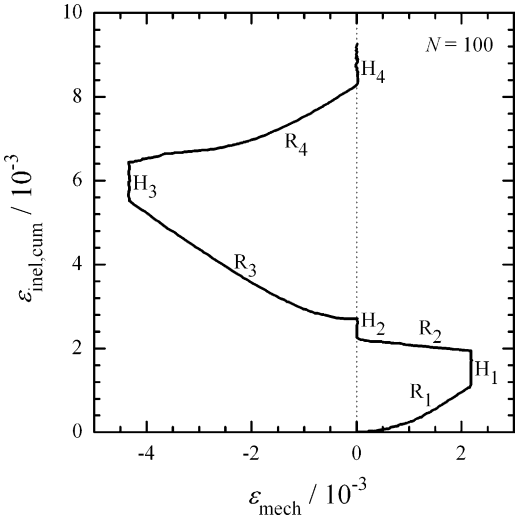

Fig. 3. Increase in cumulative inelastic strain during the cycle $N = 100$ of Fig. 1.

To delineate changes in subgrain structure due to thermal aging alone, the microstructure of the head portion of specimen 2A-4H was examined. This portion had similar time–temperature exposure as the gage portion of the specimen, but has not been influenced by strain cycling as the stresses were well within the elastic limit. Compared to the initial state the subgrains have grown by a limited amount (Fig. 7) in the course of annealing consistent with the result of Qin et al. [19].

In contrast, the cyclic inelastic deformation leads to distinct increase in w (Fig. 5) compared to the initial state after tempering and the annealed state. This makes clear that inelastic straining is necessary to bring about substantial increase in the subgrain size w. There are relatively few regions (less than about 20% areal fraction) where the degree of structural coarsening is much smaller than in Fig. 5. However, the coarsening process is not fully homogeneous. Fig. 6 gives an example where the subgrain size after cycling is still close to the initial value even though the high content of dislocations within the subgrains linking opposite boundaries suggests that dissolution of boundaries is going on also here.

Fig. 7 presents the evolution of w from state to state. It is seen that a significant (relative) increase is produced by pure cycling without hold periods. Addition of two hold periods at the ends of each cycle does not change the subgrain size w. This correlates with the similarity of the cycle shapes of 1A-NH and 1A-2H (Fig. 4) and indicates that stress σ has dominant influence on the structural spacings. Introducing hold times with stress relaxation *within* each cycle at $\epsilon_{mech} = 0$ has a marked effect not only on the stress level (Fig. 4), but also on w. In effect, the subgrains coarsen by factors of up to 6 compared to their initial size w_0. As is evident from Figs. 5 and 7 not only w, but also the dislocation spacing

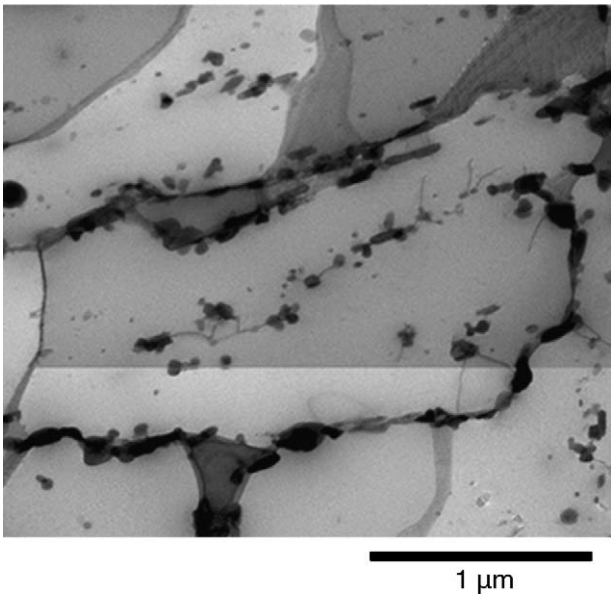

Fig. 5. Typical dislocation structure after cycling in specimen 1A-2H (two hold periods). Scanning TEM.

δ in the subgrain interior is strongly growing during cyclic deformation with four hold times.

Additional creep after cycling with four hold periods (4H) does not lead to additional coarsening of the dislocation structure (Fig. 7). This corresponds to the deliberate choice of the creep stress (see below) to render the steady state subgrain size w_∞ in creep (Eq. (1)) equal to the initial subgrain size in these creep tests, i.e. equal to the subgrain size after cyclic treatments 1A-4H and 2A-4H.

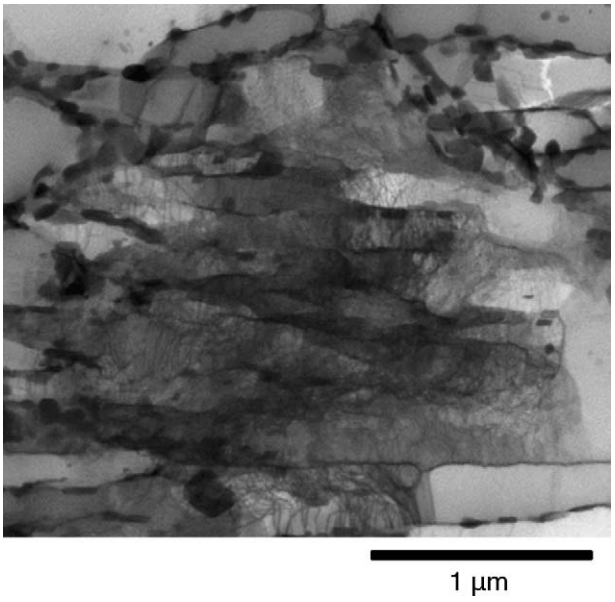

Fig. 6. Isolated region with little structural coarsening during cycling in specimen 1A-2H. Scanning TEM.

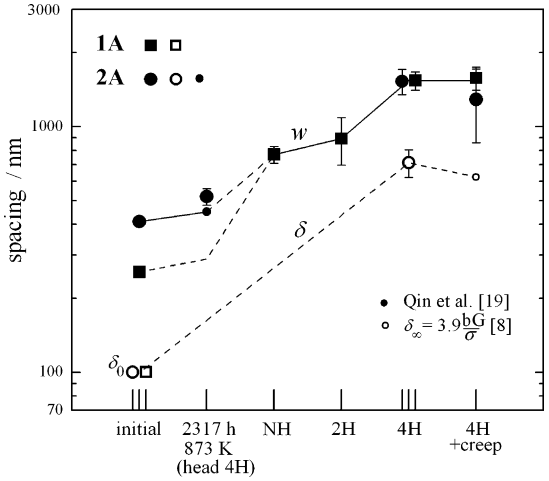

Fig. 7. Subgrain size w and dislocation spacing δ in subgrain interior for different thermal–mechanical treatments.

3.3. Effect of cyclic deformation on creep resistance

Fig. 8 shows the variation of creep rate $\dot{\epsilon}_{inel}$ at 923 K and 98 MPa with inelastic strain ϵ_{inel} for different specimens of 1A. It is seen that pure cycling without hold times has a strong effect. The primary creep stage with decreasing $\dot{\epsilon}_{inel}$ appears to have been significantly enlarged for 1A-NH compared to 1A-initial, even if one considers that the primary creep stage in the compression tests of the cycled states is enlarged compared to that in tension of the initial state by local deformation ($\approx 10^{-3}$) for adjustment between compression specimen and deformation machine. Even more importantly, the minimum creep rate $\dot{\epsilon}_{min}$ is increased by a factor of 6 by pure cycling. The duration of 13 h of prior cycling at 873 K (Table 3) is so small compared to that of the creep tests at 923 K (Fig. 8) that no extra change in precipitate structure must be expected; this is consistent with microstructural observations (work in progress). Therefore the strong difference in creep behaviours of 1A-initial and 1A-NH must be solely due to the coarsening of the dislocation structure due to prior cycling (Fig. 7). The increase of $\dot{\epsilon}_{inel}$ beyond $\dot{\epsilon}_{min}$ for both 1A-initial and 1A-NH is due to softening of the material by structural coarsening. This is a complex process where strain dependent changes of the subgrain size as well as time-dependent changes of the precipitates superimpose (see Introduction). Specimen 1A-4H creeps distinctly faster than 1A-NH (Fig. 8). This is consistent with lower creep resistance due to larger dislocation spacings compared to 1A-NH (Fig. 7).

Fig. 9 presents the curves for 2A-initial and 2A-4H. Qualitatively, the behaviour of 2A is similar to that of 1A (Fig. 8) with increase in primary creep strain and $\dot{\epsilon}_{min}$ due to prior cycling with hold periods. Quantitatively, one finds that $\dot{\epsilon}_{min}$ is lower and the rate of increase of $\dot{\epsilon}_{inel}$ with ϵ_{inel} in the tertiary stage of creep is lower for 2A compared to 1A. This can be related to the observed differences in precipitation hardening as will be discussed below.

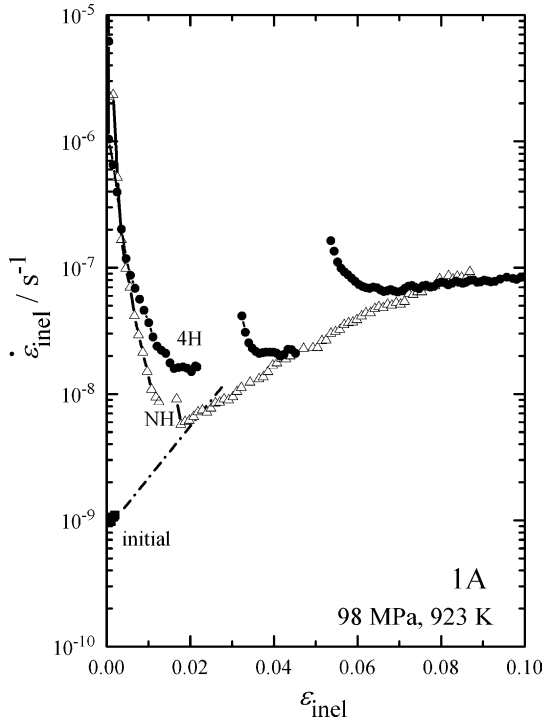

Fig. 8. Compressive creep rate as function of inelastic strain at 923 K for alloy 1A in initial state after heat treatment and in states NH (no hold periods) and 1A-4H (four hold periods) after cycling. Dash-dotted lines, interpolated (see text). Transient increases in $\dot{\epsilon}$ for 1A-4H and 1A-NH were caused by incidental interruptions of creep tests with cooling to room temperature and reheating without load. Duration of test: 1A-initial, 3428 h; 1A-NH, 1052 h; 1A-4H, 708 h.

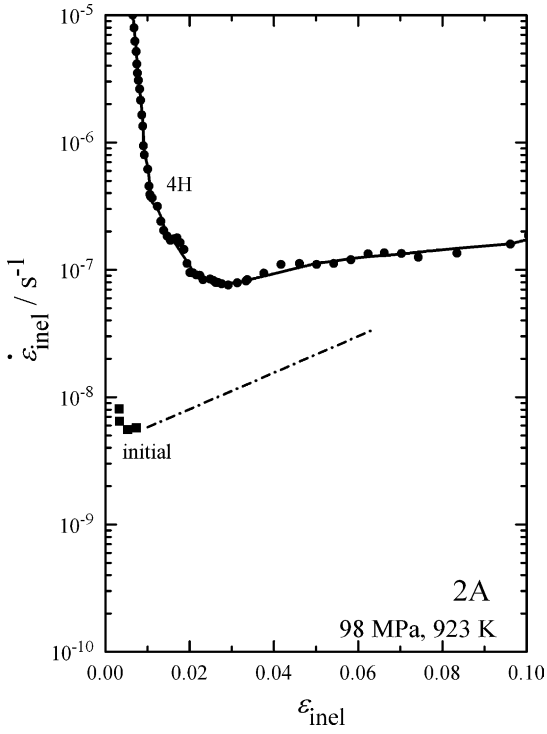

Fig. 9. As Fig. 8 for alloy 2A in initial state and state 2A-4H after cycling. Duration of test: 2A-initial, 2842 h; 2A-4H, 200 h.

4. Discussion

4.1. Subgrain evolution

The initial subgrain sizes w_0 of 1A and 2A (Figs. 7 and 12) are much smaller than the steady-state subgrain sizes from Eq. (1) corresponding to actual stresses experienced during service. Coarsening of the subgrain structure is therefore expected with deformation in components subject to cyclic or creep loads.

From creep observations it is known that the subgrains grow with inelastic strain at a certain rate depending on the ratio of the actual subgrain size w and the steady state size w_∞ [7,9,19,22]. It has been proposed to extend the expression for the subgrain growth rate [7,15,23] to the case of cyclic deformation by exchanging ϵ_{inel} for the cumulative inelastic strain $\epsilon_{inel,cum}$ [17,24]. This means that the change in direction of straining during cycling is ignored. The generalized growth rate expression then reads:

$$\frac{d \log w}{d\epsilon_{inel,cum}} = -\frac{\log w - \log w_\infty}{k_{\log w}} \quad (2)$$

$k_{\log w}$ is a growth constant controlling the rate of increase of $\log w$ with strain from $\log w_0$ towards $\log w_\infty$ which was experimentally found to be near 0.12 for martensitic tempered steels [2,7,8,15].

Numerical integration of Eq. (2) with $\epsilon_{inel,cum}$ (using $G(873\,K) = 63\,GPa$) was done using digitized values of σ and ϵ_{mech} from cyclic stress–strain curves. As the stress–strain loops were available for only limited number of cycles ($N = 1, 100, 1000$), the unknown cycle shapes were interpolated from the known ones. Fig. 10 shows the calculated evolution of w for 1A-4H within individual cycles. The points with $|\sigma| < \sigma_{cutoff} \approx 10$ MPa were omitted in the integration process in order to exclude numerical problems at $\sigma = 0$ and corresponding $w \to \infty$. This appears justified as the results are insensitive to σ_{cutoff} due to the slow progress of inelastic deformation at small stresses.

Due to its relatively small initial value, w increases continuously within the second cycle during all of the ramp and hold periods (Fig. 10a). Thus there is a rapid increase in w for small N. Comparing periods R_i and H_i (i =1–4) in Figs. 3 and 10 one finds that the progress of subgrain growth in the hold periods H_i is relatively large compared to the progress in cumulative strain during the loading periods R_i; the reason lies in the decrease of stress in the hold periods and the corresponding increase of w_∞ (Eq. (1)). As cyclic deformation progresses, the difference between the steady state subgrain size w_∞ and current subgrain size w reduces rapidly and the growth rate declines. When w reaches to the value where it exceeds the steady state subgrain size $w_\infty(\sigma)$ during certain part of cyclic deformation and is smaller in other part, the change in w is no longer monotonic. For instance, for cycle $N = 300$ of 1A-4H (Fig. 10b) w increases by a small amount during part of the cycle and decreases over other parts so that

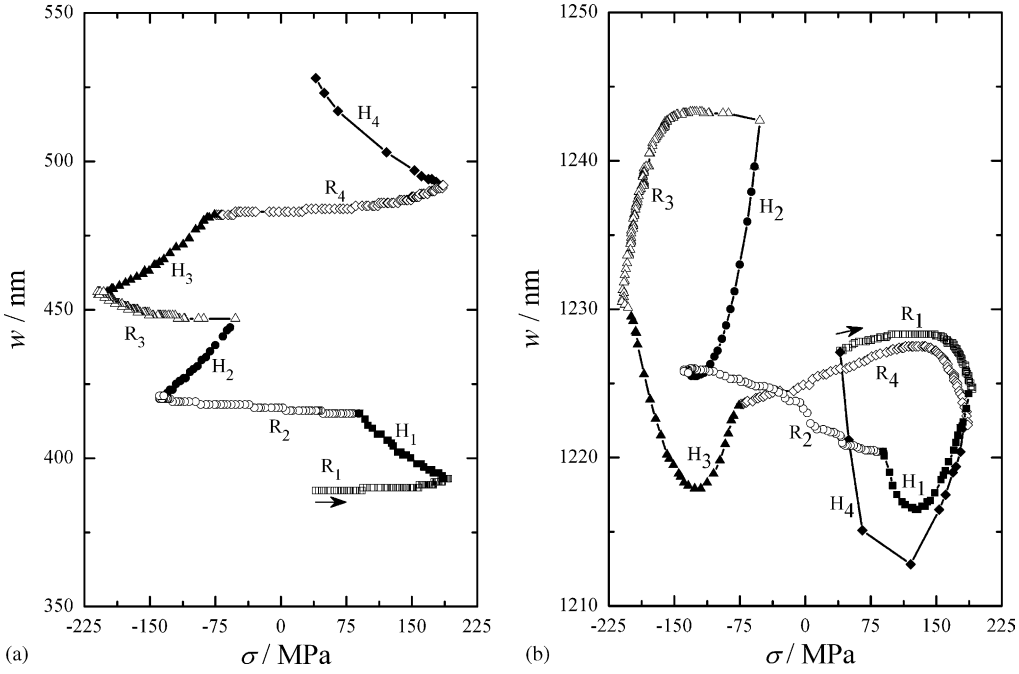

Fig. 10. Calculated evolution of subgrain size for specimen 1A-4H during cycle: (a) $N = 2$, and (b) $N = 300$. Open symbols, ramp periods; filled symbols, hold periods; arrow, start of cycle.

the net increase in w per cycle is very small. This is reflected by the saturation of subgrain size evolution over further cycling, provided the stress levels in the cycles do not change.

The overall evolution of w in 1A-4H is shown in Fig. 11. Also shown on the same plot are the evolutions to be expected if the stress–strain cycle shapes are assumed to be constant for all cycles, equal to those of cycles $N = 100$ and 1000, respectively. In these cases w saturates at $\epsilon_{\text{inel,cum}} \approx 1$. Comparison of the three curves shows that the final subgrain size is governed by the last cycles which have lower peak stresses, and thereby are associated with larger steady-state subgrain sizes. The dominant role of stress in determining the final subgrain size (Eq. (1)) is evident from the fact that subgrain sizes after cycling (Fig. 12) and peak stress levels during final stages of cycling (Fig. 4) in specimens 1A-4H and 2A-4H are nearly the same in spite of different initial sizes w_0 (Fig. 12).

Fig. 12 compares the measured subgrain sizes w to the sizes w_{cal} calculated with (2) and $k_{\log w} = 0.12$ (filled symbols). It is seen that the two agree within experimental uncertainty for the states 1A-NH and 1A-2H after cycling without hold times at $\epsilon_{\text{mech}} = 0$. The same holds for the states after creep following prior cycling with hold times confirming the well known subgrain evolution during creep. In qualitative agreement with the strong reduction of the peak stress levels due to hold periods at $\epsilon_{\text{mech}} = 0$ (Fig. 4), w_{cal} is somewhat larger for 1A-4H compared to 1A-NH and 1A-2H. The w_{cal}-values for 1A-4H and 2A-4H, however, are not large enough to fully agree to the measured w-values.

This means that the experimentally determined w is too large and/or the calculated w_{cal} is too low. A systematic experimental error in w, which may have been provoked by long-range heterogeneity of the cycled subgrain structure, cannot be excluded. On the other hand, the alternative of w_{cal} being too low finds support from the experimental evidence [25] that subgrain activity by migration is particularly strong and even dominating in periods of reduced stress, where the rate of subgrain growth with strain was enhanced by an order of magnitude short after reduction in stress. Modifying the rate of subgrain growth in (2) by reducing $k_{\log w}$ during the hold periods by a factor of 10 yields the w_{cal}-values depicted by open symbols in Fig. 12. This modification causes all data to fall within the shaded band representing ±20% experimental

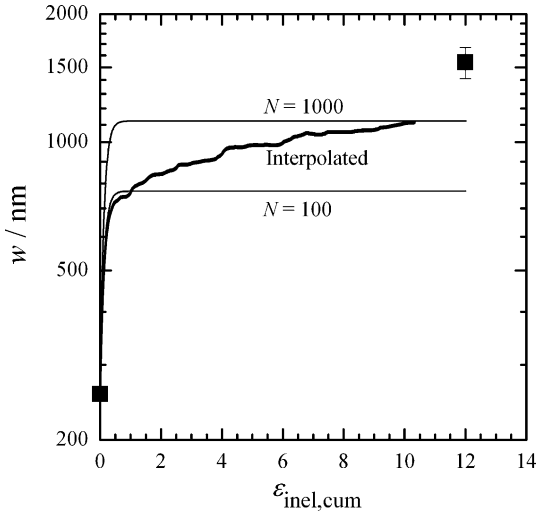

Fig. 11. Evolution of subgrain size with cumulative strain during cycling of specimen 1A-4H. Lines, calculated (see text); symbols, measured.

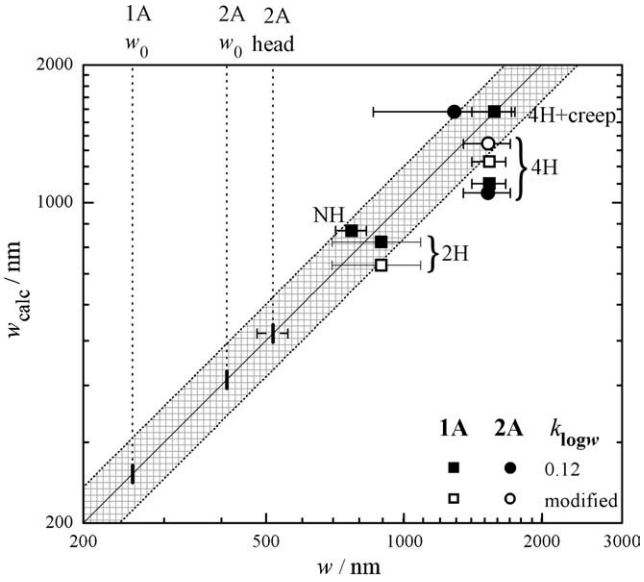

Fig. 12. Calculated final subgrain sizes w_{calc} vs. measured sizes w. Vertical dotted lines mark measured initial values. Modified $k_{\log w}$, see text.

scatter of w-determination. However, the position of w_{cal} is slightly deteriorated for 1A-2H by the modification so that the degree of improvement by the modification of $k_{\log w}$ remains unclear.

In any case, Eq. (2) with or without modification allows one to estimate the amount of subgrain coarsening due to cyclic deformation at reasonable accuracy.

4.2. Creep response to prior cycling

Two effects of cycling on the microstructure are prominent: the subgrains as well as the spacings of free dislocations in the subgrains have grown. The refilling of subgrains with free dislocations under creep load requires additional primary creep strain. It is well known from the kinetics of dislocation structure evolution, that the free dislocations attain their stress-dependent steady state spacing within a relatively small strain interval [7,8,23] which is about one order of magnitude smaller than that which is necessary for the subgrains. Consequently, the large increase of δ by cycling relative to δ_0 (Fig. 7) and the change in mode of deformation from cycling to creep will lead to an enhanced primary creep rate, but will contribute little to the increase of $\dot{\epsilon}_{min}$ which is controlled by the subgrain structure. The coarsening of the subgrains by prior cycling reduces subgrain strengthening and explains the increase of $\dot{\epsilon}_{min}$. As there is no alternative explanation of the observed reduction in creep resistance by pure cycling, the present results can be taken as proof of the existence of subgrain strengthening which is still debated by some [26].

Due to the fact that in the creep tests on 1A-4H and 2A-4H, the initial subgrain size (after prior cycling) and the final subgrain size are the same (Fig. 7), no change in w must occur during creep. Nevertheless one finds a relative minimum of creep rate even for these states.

The exact reason for this increase is unclear at present. Due to the short duration (200 h, Fig. 9) of creep of 2A-4H significant changes in precipitate structure are not expected. Thus, changes in the dislocation structure must be supposed to be one reason of tertiary creep in the compression tests on the 4H-specimens. It is proposed that the isolated regions with relatively low subgrain size (Fig. 6) constitute relatively hard regions whose structural coarsening during creep causes softening. In addition to that, detailed changes of the subgrain boundary structure may play a role. One possibility of such changes results from the notion that the cyclic change in the sign of applied stress and the corresponding direction of migration allows the subgrain boundaries to stick to places with high precipitate density (compare (Fig. 5)) more easily than is possible during unidirectional creep deformation. The reduction of areal density of precipitates at subgrain boundaries in subsequent creep may have a softening effect. For 1A-4H the situation is more complicated due to longer times of creep testing at 923 K and greater instability of V-containing precipitates. While in 2A VX is the only observed V-containing phase, one finds M_2X (M, metal; X, C and N) in the initial state of 1A and Z-phase after long-term creep of 1A [14]. It is possible that the structural changes associated with these two V-containing phases lead to loss of creep resistance even in the relatively short creep test on 1A-4H with rates above 10^{-8}/s.

5. Concluding remarks

Tensile–compressive strain cycling at elevated temperature of 12CrMoWVNbN10-1-1, belonging to the group of tempered martensite 9–12% Cr-steels with precipitate-stabilized subgrain structure, leads to significant subgrain coarsening. The presence of hold periods with stress relaxation within the cycles enhances the coarsening of subgrains. The evolution of subgrain size w was successfully calculated by extending the established expression for the rate of change of subgrain size with unidirectional strain in creep to the case of cyclic straining. This was done by replacing the inelastic strain by the cumulative inelastic strain. The coarsening of the dislocation structure due to cyclic deformation at elevated temperature is consistent with the drastic reduction of creep resistance observed after cyclic deformation confirming the idea of strengthening by subgrains. The present results open the opportunity of modeling the complex interaction between creep and cyclic loading at elevated temperature in terms of a plasticity model based on few important microstructural parameters like subgrain size and spacing between hard precipitates.

Acknowledgments

Thanks are due to the Deutsche Forschungsgemeinschaft and the consortium of BMWA and industry within the

project DT1/2 for financial support. We also thank the BMBF for funds under Indo-German scientific cooperation programme.

References

[1] G. Eggeler, N. Nilsvang, B. Ilschner, Steel Res. 58 (1987) 97.
[2] W. Blum, S. Straub, Steel Res. 62 (1991) 72.
[3] P.J. Ennis, A. Zielinska-Lipiec, O. Wachter, A. Czyrska-Filemonowicz, Acta Mater. 45 (1997) 4901.
[4] M. Staubli, K.H. Mayer, T.U. Kern, R.W. Vanstone, R. Hanus, J. Stief, K.H. Schönfeld, in: R. Viswanathan, W.T. Bakker, J.D. Parker (Eds.), Proceedings of the Third Conference on Advances in Materials Technology for Fossil Power Plants, The Institute of Materials, Swansea, 2001.
[5] T. Fujita, in: R. Viswanathan, W.T. Bakker, J.D. Parker (Eds.), Proceedings of the Third Conference on Advances in Materials Technology for Fossil Power Plants, The Institute of Materials, Swansea, 2001.
[6] W. Blum, S. Straub, in: Proceedings of the Eighth International Symposium on Creep-Resistant Metallic Materials, Zlín, 1991.
[7] S. Straub, M. Meier, J. Ostermann, W. Blum, VGB Kraftwerkstechnik 73 (1993) 646.
[8] S. Straub, Verformungsverhalten und Mikrostruktur Warmfester Martensitischer 12% Chromstähle. Fortschr.-Ber. VDI Reihe 5 Nr. 405, VDI Verlag, Düsseldorf, 1995.
[9] W. Blum, G. Götz, Steel Res. 70 (1999) 274.
[10] J. Hald, Steel Res. 67 (1996) 369.
[11] A. Strang, V. Vodarek, Mater. Sci. Technol. 12 (1996) 552.
[12] J.D. Robson, H.K.D.H. Bhadeshia, Mater. Sci. Technol. 13 (1997) 640.
[13] F. Abe, Mater. Sci. Eng. A 319–321 (2001) 770.
[14] G. Götz, W. Blum, Mater. Sci. Eng. A 348 (2003) 201.
[15] P. Polcik, Modellierung des Verformungsverhaltens der warmfesten 9–12% Chromstähle im Temperaturbereich von 550–650 °C, D29 (Dissertation Universität Erlangen-Nürnberg), Shaker Verlag, Aachen, 1999.
[16] G. Götz, Langzeitentwicklung der Mikrostruktur neuer 9–12% Chromstähle für den Einsatz in Kraftwerken, Dr.-Ing. Thesis, Universität Erlangen-Nürnberg, 2004.
[17] H. Chilukuru, W. Blum, M. Schwienheer, A. Scholz, Langzeitverhalten warmfester Stähle und Hochtemperaturwerkstoffe, Beiträge zur 26, Vortragsveranstaltung der Arbeitsgemeinschaft für Warmfeste Stähle und für Hochtemperaturwerkstoffe, Stahl Institut VDEh, Düsseldorf, 2003.
[18] G. Götz, W. Blum, Langzeitverhalten Warmfester Stähle und Hochtemperaturlegierungen, Beiträge zur 24. Vortragsveranstaltung der Arbeitsgemeinschaft für Warmfeste Stähle und für Hochtemperaturwerkstoffe, Stahl Institut VDEh, Düsseldorf, 2001.
[19] Y. Qin, G. Götz, W. Blum, Mater. Sci. Eng. A 341 (2003) 211.
[20] S. Straub, T. Hennige, P. Polcik, W. Blum, in: Proceedings of the Fourth European Conference on Advanced Materials and Processes, Associatione Italiana di Metallurgia, Mailand, 1995.
[21] W. Blum, P. Polcik, S. Straub, K.H. Mayer, VGB Power Tech. 80 (2000) 59.
[22] S. Straub, T. Hennige, P. Polcik, W. Blum, Steel Res. 66 (1995) 394.
[23] D. Henes, H. Möhlig, S. Straub, J. Granacher, W. Blum, C. Berger, H. Mughrabi, G. Gottstein, H. Mecking, H. Riedel, J. Tobolski (Eds.), Microstructure and Mechanical Properties of Metallic High-Temperature Materials, Wiley/VCH, Weinheim, 1999.
[24] H. Chilukuru, M. Schwienheer, A. Scholz, W. Blum, in: S.L. Mannan (Eds.), Proceedings of the Fourth Conference on Creep Fatigue and Creep-Fatigue Interaction, IGCAR, Kalpakkam, 2003.
[25] W. Müller, M. Biberger, W. Blum, Phil. Mag. A 66 (1992) 717.
[26] M. Kassner, M.T. Perez-Prado, Fundamentals of Creep in Metals and Alloys, Elsevier, 2004.

E Publication [13]

Quantitative Gefügeananlyse von 9-12%Cr Stählen mittels AFM, REM und TEM

T. Seibert, K. Durst, H. Chilukuru, W. Blum, and M. Göken

In Mathias Göken, editor, 37. *Praktischen Metallographie Sonderbände - Fortschritte in der Metallographie*, page 73, Erlangen, Sept. 2005. DGM.

Quantitative Gefügeanalyse von 9-12% Cr-Stählen mittels AFM, REM und TEM

T. Seibert, K. Durst, H. Chilukuru, W. Blum, M. Göken
Universität Erlangen - Nürnberg, Institut für Werkstoffwissenschaften, Lehrstuhl 1, 91058-Erlangen

1 Einleitung

Durch die Entwicklung neuer Materialien für Kraftwerke soll die Dampftemperatur von aktuell 610 °C auf 650 °C erhöht und dadurch der Treibstoffverbrauch reduziert und die CO_2-Emission gesenkt werden [1]. Von Bedeutung sind dabei getemperte martensitische 9-12% Cr-Stähle, die z.B. in Rohrleitungen eingesetzt werden. Eine wichtige Kenngröße, die das Verhalten der Stähle während des Einsatzes charakterisiert, ist deren Kriechverhalten. Das Kriech- bzw. Verformungsverhalten der Stähle ist direkt mit der Evolution der Mikrostruktur korreliert. Somit ist eine exakte Charakterisierung der Ausscheidungs- und Versetzungsstruktur zum Verständnis der mechanischen Eigenschaften notwendig. Von besonderem Interesse ist dabei die Verteilung und Langzeitstabilität von Karbonitriden. Im Rahmen eines Verbundprojektes werden Warmauslagerungsversuche an einer Modelllegierung durchgeführt und die Mikrostruktur sowohl mittels Extraktionsreplika und TEM-Folien, als auch ergänzend mit hochauflösender Rasterelektronenmikroskopie (REM) und Rasterkraftmikroskopie (AFM) charakterisiert. Mikrostrukturelle Kenngrößen, wie die Größenverteilung der Ausscheidungen und der Subkörner, dienen als Eingangsdaten für das Softwarepaket MIKORA, mit welchem das Kriechverhalten mikrostrukturell auf Basis eines Verbundmodells [2,3,4,5] modelliert werden kann.

2 Charakterisierung der Mikrostruktur

Tabelle 1: Chemische Zusammensetzung der Modelllegierung

	Fe	C	Si	Mn	Cr	Mo	W	V	Nb	N
Gew.%	bal.	0,12	0,10	0,42	10,7	1,07	1,04	0,16	0,05	0,056

Die folgenden Untersuchungen werden an einer experimentellen Modelllegierung (Tabelle 1) durchgeführt. Zur Charakterisierung der Mikrostruktur werden Extraktionsreplika hergestellt und im Transmissionselektronenmikroskop (TEM) mittels EDX-Analyse zur Identifikation einzelner Phasen untersucht. Somit kann die Teilchengrößenverteilung phasenselektiv erstellt werden. Aus den gemessenen Teilchendurchmessern wird der Volumenanteil der einzelnen Ausscheidungen berechnet. Das Ergebnis der Bestimmung des Volumenanteils der einzelnen Phasen ist dabei von den Ätzbedingungen abhängig. Aus der Modelllegierung wurde außerdem eine TEM-Folie präpariert, die sowohl im TEM, als auch im REM und AFM an der gleichen Stelle abgebildet wurde. Durch den Vergleich dieser drei Verfahren und unter zu Hilfenahme der Ergebnisse des Extraktionsreplika soll eine zuverlässigere Bestimmung der Volumenanteile der einzelnen Phasen ermöglicht werden.

2.1 Extraktionsreplika

Für die Herstellung eines Replikas wird die Oberfläche des Probenmaterials zunächst geschliffen und mittels Diamantpaste der Körnung 1 µm poliert. Anschließend wird sie mit Pikrinsäure für ca. 40 sec angeätzt. Die Pikrinsäure ätzt dabei nur die Fe-Matrix an, nicht die Karbidausscheidungen. Nach dem Bedampfen der Oberfläche mit Kohlenstoff wird das Replika unter Verwendung von Königswasser abgelöst (siehe Bild 1).

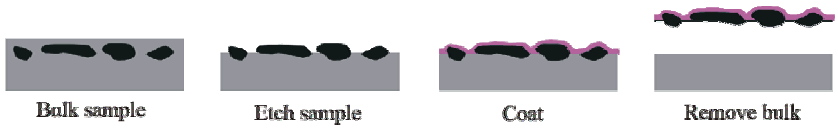

Bild 1: Herstellung eines Extraktionsreplika nach [6].

Anschließend werden Bilder des Replikas im Transmissionselektronenmikroskop im STEM-Modus (siehe Bild 2 links) aufgenommen und jedes einzelne Teilchen mittels EDX-Analyse untersucht. Durch die charakteristischen Spektren, die die Ausscheidungsphasen zeigen, können die Teilchen den entsprechenden Phasen zugeordnet werden. Wichtige Phasen sind dabei $M_{23}C_6$, M_2X, MX, Laves- und Z-Phase.

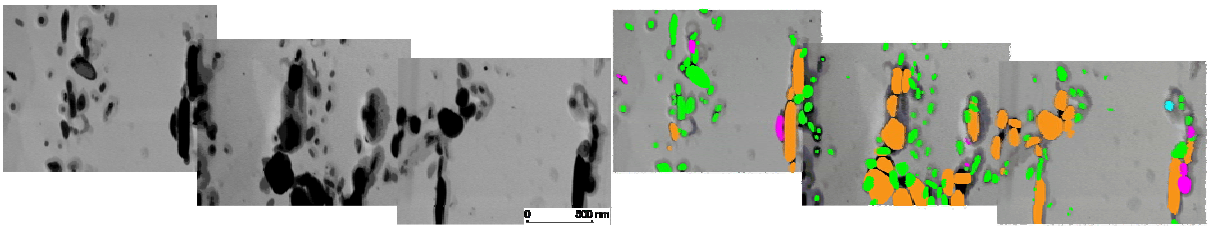

Bild 2: Abbildung des Extraktionsreplikas im TEM, STEM-Modus (links); Markierung der einzelnen Phasen (rechts).

Mit entsprechender Bildbearbeitungssoftware werden die jeweils gleichen Phasen markiert (siehe Bild 2 rechts) und mit einer Bildanalysesoftware (Image C) der Teilchendurchmesser der Ausscheidungen ermittelt. Aus den so gewonnenen Daten kann nun sowohl der Volumenanteil der einzelnen Phasen berechnet als auch die Vergröberungskonstanten der unterschiedlichen Ausscheidungen nach Kriechverformung oder Warmauslagerung bestimmt werden.

2.2 Untersuchung einer TEM-Folie im TEM, REM und AFM

Zusätzlich zur Charakterisierung der Modelllegierung mittels Replikatechnik wurden auch andere hochauflösende Mikroskopieverfahren zur Charakterisierung eingesetzt. Um die einzelnen Verfahren direkt miteinander vergleichen zu können, wird eine TEM-Stahlfolie präpariert, die sowohl im TEM (STEM-Mode) als auch im REM (FEG-REM) und AFM (tapping mode Spitze mit einem Spitzenradius von ca. 10 nm) an der gleichen Stelle untersucht wird (siehe Bild 3). Besonderes Augenmerk wird dabei auf die vergleichende Charakterisierung der Ausscheidungs- und Subkorngröße gelegt.

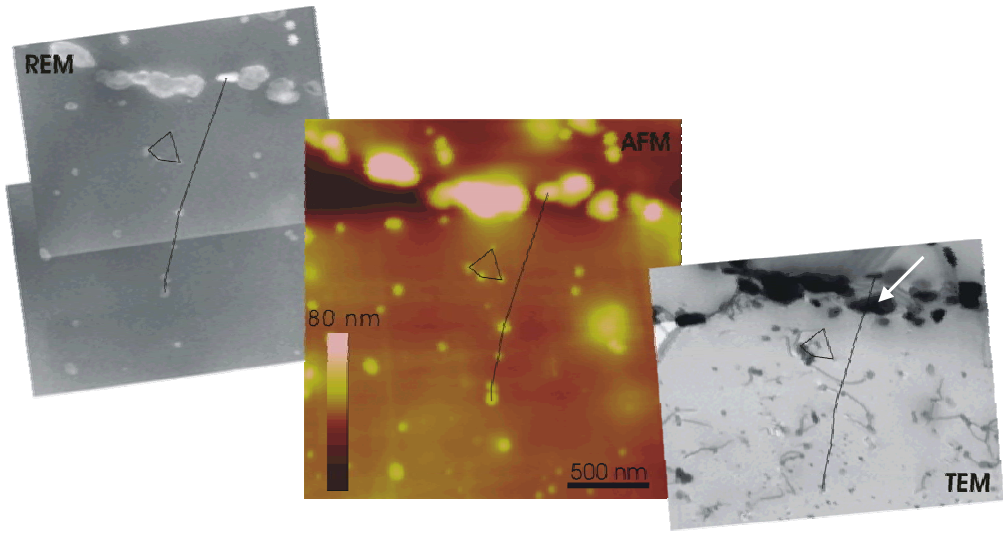

Bild 3: Abbildung der gleichen Stelle einer TEM-Folie im REM, AFM, und TEM

Tabelle 2: Mittlerer Teilchendurchmesser d_p im REM, AFM und TEM aus Bild 3

	REM	AFM	TEM
d_p / nm	68	67*	47,8**

* nach Korrektur des Spitzenradius
** korrigiert nach CHOW

In Bild 3 ist eine Detailanalyse der gleichen Stelle einer TEM-Folie im REM, AFM und TEM dargestellt. Durch den direkten Vergleich kann man deutlich erkennen, dass bestimmte Teilchen nur in der TEM-Abbildung zu sehen sind (weißer Pfeil). Besonders Ausscheidungen unter 20 nm sind nur im TEM sichtbar, weshalb der mittlere Teilchendurchmesser deutlich kleiner ist als der im REM und AFM. Dabei wurde bereits der Effekt der dünnen Folie auf die Bestimmung des mittleren Teilchendurchmessers auf TEM-Abbildungen berücksichtigt. Aus der Zahl der abgebildeten Ausscheidungen wird deutlich, dass im TEM ein Volumen, im AFM und REM jedoch nur die Oberfläche abgebildet wird (Tabelle 2). Die abgebildeten Teilchen im REM und AFM sind identisch. Nach der Berücksichtigung des Spitzenradius von ca. 10 nm [7] stimmt der mittlere Teilchendurchmesser im AFM und REM sehr gut überein. Da die Fläche der hier dargestellten Bilder zu klein ist, um eine ausreichende Statistik hinsichtlich der Bestimmung des Flächen- und Volumenanteils zu erhalten, wird die Ermittlung der Ausscheidungsgrößenverteilung an Bildmontagen durchgeführt.

2.2.1 Bestimmung des Volumen- und Flächenanteils

Der Volumenanteil V_V und der Flächenanteil A_A werden über folgende Formeln bestimmt:

$$V_v = \frac{N * \overline{V}}{A(h_{Folie} + d_p)} \qquad A_A = \frac{N * \overline{A}}{A}$$

N ist die Zahl der untersuchten Teilchen, A die untersuchte Fläche, d_p der mittlere Teilchendurchmesser, V das mittlere Volumen der Ausscheidungen und $\overline{A}$ die mittlere Teilchenfläche. Zur Bestimmung des Volumenanteils muss außerdem die Dicke der TEM-Folie h_{Folie} von ungefähr 100 nm berücksichtigt werden. Zur Bestimmung des Volumenanteils in TEM-Folien erweist sich dies als eine gute Abschätzung. Problematisch verhält es sich jedoch bei Replikas, da nicht genau bekannt ist, aus welchen Volumen die am Kohlenstofffilm haftenden Teilchen stammen.

2.2.2 Charakterisierung der Ausscheidungsgröße

Zur Bestimmung der Ausscheidungsgrößenverteilung werden Bildmontagen aus TEM- und REM-Abbildungen mit einer Fläche von ca. 12 µm² verwendet. Auf eine genaue Auswertung der AFM Bilder wird hier verzichtet, da die Abbildung im AFM im Wesentlichen mit der im REM vergleichbar ist. Zusätzlich wird ein Replika des gleichen Materials an einer ähnlichen Stelle untersucht und in den Vergleich mit einbezogen (siehe Bild 4).

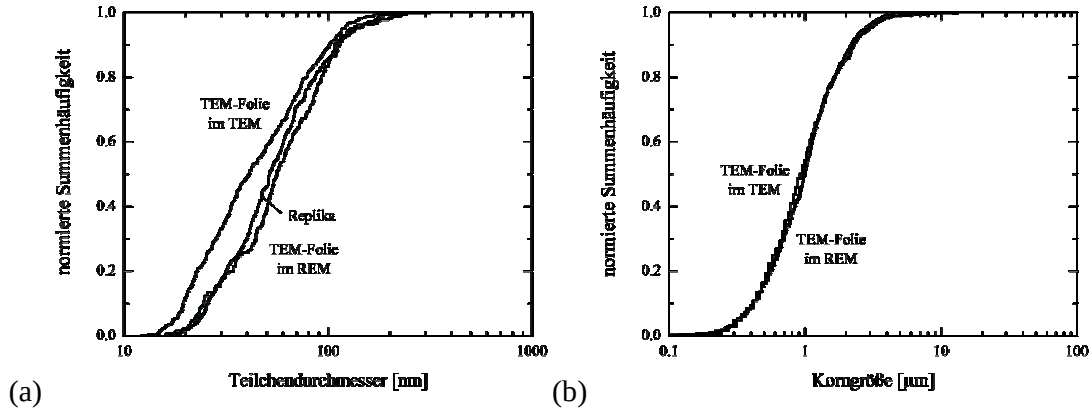

Bild 4:(a) Teilchengrößenverteilung des Replika, der TEM-Folie untersucht im TEM und im REM. (b) Subkorngrößenverteilung der TEM- und REM-Abbildungen

Anhand der Teilchengrößenverteilung der Ausscheidungen in den einzelnen Abbildungsverfahren (Bild 4a) wird deutlich, dass für Teilchen größer 100 nm eine sehr gute Übereinstimmung zwischen Replika und der TEM-Folie im TEM und REM vorliegt. Für Ausscheidungen unter 100 nm Größe scheinen die Abbildung des Replika und der TEM-Folie im REM sehr gut überein zustimmen, die Kurve der TEM-Abbildung ist etwas zu kleineren Teilchendurchmessern hin verschoben. Die Zahl der untersuchten Teilchen N (siehe Tabelle 3) bei etwa gleicher Bildgröße A für Replika und TEM-Abbildung ist in etwa gleich. Im REM hingegen werden weniger Teilchen gefunden. Hinsichtlich des Volumen- und Flächenanteils der Ausscheidungen zeigen TEM und REM Abbildung sehr gute Übereinstimmung, wohingegen der Flächenanteil des Replikas zu deutlich höheren Werten hin abweicht. Um diese Diskrepanz erklären zu können ist es notwendig, sowohl die Berechnung des Volumenanteils als auch die Replikaherstellung an sich genauer zu betrachten.

Tabelle 3: Vergleich der Teilchenzahl N, des Teilchendurchmessers d_p, des Volumenanteils V_V und Flächenanteils A_A der Montagen aus Bild 4a

	Replika	TEM	REM
N	343	418	186
d_p / nm	63,3	53,4	65
V_V	0,0645	0,0454	/
A_A	0,127	/	0,044

2.2.3 Charakterisierung der Subkorngröße

Zur Bestimmung der Subkorngröße der TEM-Folie im TEM und REM wurden Übersichtsbilder der gleichen Stelle verwendet, wobei die Fläche des TEM Bildes 1307 µm², die des REM Bildes 501 µm² betragen. Zur Analyse wurde ein Schnittlinienverfahren verwendet. Obwohl im Gegensatz

zur TEM-Abbildung Subkörner im REM nur durch die Belegung mit Ausscheidungen erkennbar sind, stimmen die Subkorngrößenverteilungen sehr gut überein. Eine mögliche Ursache kann sein, daß das untersuchte Material kriechverformt worden ist und aus diesem Grund die Subkorngrenzen sehr stark mit Ausscheidungen belegt sind. Dadurch kann die Lage der Subkorngrenzen relativ gut abgeschätzt werden (Bild 4b).

2.3 Detaillierte Betrachtung der Replikaherstellung

Die folgende Abbildung (Bild 5) soll schematisch zeigen, welche Oberflächenreliefs sich nach der Ätzung mit Pikrinsäure ausbilden können. In der Mitte ist der Zustand unmittelbar nach dem Ätzen dargestellt, bei dem bestimmte Teilchen vollständig frei gelegt werden. Durch anschließendes Reinigen der Probe kann Fall 1 eintreten, d.h. dass alle vollständig frei gelegten Teilchen von der Oberfläche abgespült werden. Es ist aber auch möglich, dass die frei liegenden Teilchen durch Adhäsion an der Oberfläche haften bleiben (Fall 2). Diese beiden Grenzfälle machen deutlich, dass die Dicke d bzw. das Volumen, aus dem die am Replika haftenden Teilchen stammen, in beiden Fällen stark voneinander abweichen.

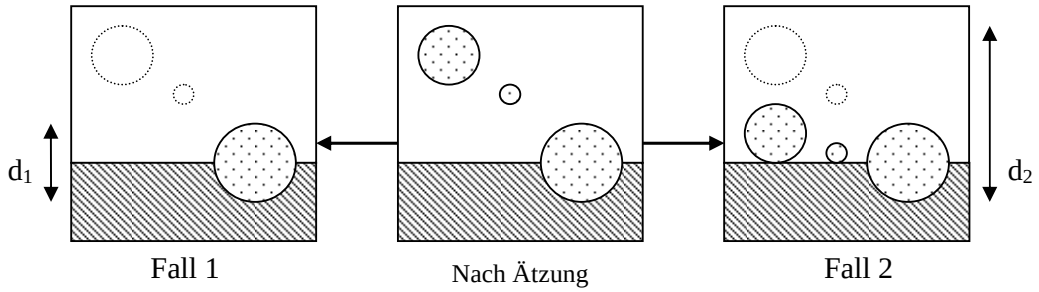

Bild 5: Replikaherstellung (schematisch)

Zur Aufklärung der Ätzbedingungen wurde die Probenoberfläche nach Ätzung mit Pikrinsäure im REM untersucht (siehe Bild 6).

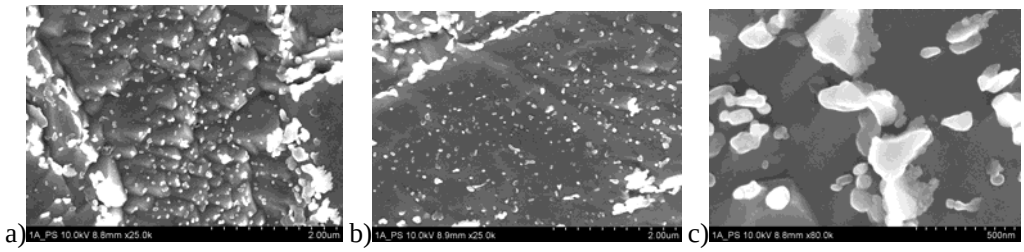

Bild 6: Oberfläche nach Ätzung mit Pikrinsäure a) unregelmäßiger Ätzangriff. b) glatte Abtragung. c) Überlappung einzelner Teilchen an Korngrenze (Balken a, b: 2000 nm, c: 500nm)

Im linken und mittleren Bild ist jeweils ein Korn inklusive Korngrenze dargestellt. Auffällig ist, dass das Ätzverhalten aufgrund unterschiedlicher Kornorientierungen in beiden Fällen stark voneinander abweicht. Die rechte Abbildung zeigt einen Ausschnitt einer Korngrenze, an der man das Überlappen einzelner Teilchen erkennen kann. Bei der Analyse im TEM muss deshalb darauf geachtet werden, dass nur repräsentative Stellen, an denen die Teilchenzahl weder zu hoch noch zu niedrig ist, analysiert werden. Da die untersuchte Replikafläche sehr klein ist, würde die Wahl einer zu stark mit Ausscheidungen belegten Fläche einen zu hohen Volumenanteil der entsprechenden Phasen ergeben. An manchen Stellen im Replika kann man außerdem erkennen, dass Teilchen aus der Folie gefallen sind. Auch diese Bereiche sollten nicht zur Analyse herangezogen werden.

Im Mittel liefert die Formel zur Berechnung des Volumenanteils unter der Annahme einer Ätztiefe von 100 nm eine relativ gute Übereinstimmung zwischen den Ergebnissen aus der Abbildung der Stahlfolie und des Replikas.

3 Zusammenfassung

Die Charakterisierung von 9-12% Cr-Stählen erfolgt mittels Extraktionsreplika im Transmissionselektronenmikroskop. Zur Ermittlung von Kenngrößen wie dem Volumenanteil ausgeschiedener Phasen ist es von großer Bedeutung zu wissen, aus welchem Volumen die am Replika haftenden Ausscheidungen stammen. Zur Aufklärung wurde die gleiche Stelle einer TEM-Folie im TEM, REM und AFM untersucht. Durch den direkten Vergleich der flächenhaften AFM- und REM-Abbildung, der Volumenabbildung im TEM und des Replikas wurde deutlich, dass das Replika eine Kombination aus flächen- und volumenhafter Abbildung darstellt. Diese Aussage wird durch das unterschiedliche Ätzverhalten einzelner Körner vor der Replikaherstellung bekräftigt. Zur Charakterisierung von Stählen mittels Extraktionsreplika sollten demnach nur repräsentative Stellen des Replikas mit einer angemessenen Teilchenzahl herangezogen werden, beziehungsweise möglichst große Volumina ausgewertet werden. Weiterhin erweißt sich die Annahme einer Ätztiefe von 100 nm zur Bestimmung des Volumenanteils der verschiedenen Phasen als relativ gute Abschätzung.

4 Literatur

[1] V. Knezevic, G. Sauthoff, J. Vilk, G. Inden, A. Schneider, R. Agamennone, W. Blum, Y. Wang, A. Scholz, C. Berger, J. Ehlers, L. Singheiser, Martensitic/ferritic super heat restistant 650°C steels – Design and testing of model alloys, ISIJ International 42, 2002, pp. 1505-1514.

[2] P. Polcik, S. Straub, W. Blum, in: The 4th European Conference on Advanced Materials and Processes, Associatione Italiana di Metallurgia, Mailand, 1995, pp. 313–318.

[3] D. Henes, H. Möhlig, S. Straub, J. Granacher, W. Blum, C. Berger, in: H. Mughrabi, G. Gottstein, H. Mecking, H. Riedel, J. Tobolski (Eds.), Microstructure and Mechanical Properties of Metallic High-Temperature Materials, Wiley-VCH, Weinheim, 1999, pp. 179–191.

[4] R. Sedlácek, W. Blum, Comp. Mater. Sci. 25 (1-2), 2002, pp. 200–206.

[5] X. H. Zeng, W. Blum, in: 29th MPA Seminar, Safety and Reliability in Energy Technology, Oct 2003, Stuttgart, 2003.

[6] R. Agamennone, Deterioration of creep resistance at 923K of tempered martensitic 9-12% Cr-steels by precipitation of Z-phase, Erlangen, 2004.

[7] K. Durst **,** M. Göken: Quantitative Microstructural Characterisation by Atomic Force Microscopy and Electron Microscopy - A Comparative Study on the Superalloy Waspaloy, Prakt. Metallogr., 38 (2001), 197-215

F Publication [7]

Tertiary creep of tempered martensite 9-12%Cr-steels - On the microstructural origin of creep life limitation

W. Blum and H. Chilukuru

In *OPE 2006 - Chennai, International Conference on Pressure vessels and Piping*, Chennai, 2006.

Tertiary creep of tempered martensite 9-12%Cr-steels – On the microstructural origin of creep life limitation

W. Blum* **and H. Chilukuru**

Institut für Werkstoffwissenschaften, LS 1, University of Erlangen-Nürnberg,
Martensstr. 5, 91058 Erlangen, Germany
* wolfgang.blum@ww.uni-erlangen.de, Tel.: +49 9131 8527507; Fax: +49 9131 8527504

ABSTRACT

In programs for development of tempered martensite steels with 9 to 12%Cr for enhanced creep resistance one finds that improved short-term creep properties frequently do not persist in long-term service. This is primarily due to acceleration of creep in the tertiary stage resulting from coarsening of the microstructure. Cavitation due to pore formation accelerates creep under uniaxial stress only in the final part of the tertiary stage. Precipitates formed in the course of the heat treatment consisting of martensitic transformation and tempering are of eminent importance for the creep resistance as they do not only harden the steel but also stabilize the dislocation (subgrain) structure by reducing the strain rate. Subtle differences between the different precipitate phases, in particular the V-containing ones, decide upon whether or not the precipitate structure remains stable and a high creep resistance is maintained in long-term service.

Keywords: Subgrains; Precipitates; Pores; Tertiary Creep; Compression Tests

1. INTRODUCTION

Tempered martensite steels with 9 to 12%Cr are used in power stations for components which are exposed to pressure, heat and environmental attack. Due to enhanced requirements for reduced specific CO_2 emission of power stations there is a demand for increase of the operating temperatures and pressures which means improved creep and fatigue resistance of the components [1, 2, 3, 4]. In material development programs one frequently finds that improved short-term creep properties do not persist in long-term service [5, 6, 7, 8, 9, 10]. For control of long-term properties it is necessary to understand the microstructural origin of this failure.

Under tensile stress creep life is limited by the continuous increase of creep rate $\dot{\epsilon}$ in the tertiary stage of creep. The tertiary stage follows the secondary stage where the creep rate has reached its minimum value. The reason for the changes of $\dot{\epsilon}$ lie in the microstructure of the materials. It is formed from dislocations being the carriers of deformation, solute atoms, precipitates of foreign phases within the steel matrix, pores and microcracks.

Evolution of damage in the form of pores and microcracks is one cause of tertiary creep. However, this is not the only and usually not the primary source of acceleration of creep in the tertiary stage. Rather, the life-limiting increase of creep rate stems from global changes in the dislocation and phase structure of the steels. Being hardened by dislocations forming a subgrain structure and by precipitates of various types located at the subgrain boundaries and in the subgrain interior the steels loose in creep resistance as strengthening by subgrains and precipitates is declining [11, 12, 13, 14, 15, 16, 17, 10]. This occurs inevitably by coarsening of the subgrain structure towards the steady state

structure depending on stress [18, 19, 20] and by coarsening of the precipitates due to Ostwald ripening and nucleation of stabler phases. The present contribution gives an overview of microstructural development in tempered martensite steels with focus on the differences in stability of different precipitate phases, their consequences on creep resistance and measures to avoid instable phases leading to deleterious breakdown of creep resistance.

2. DISLOCATIONS

It is known that the dislocation structure approaches a steady state where generation and annihilation of dislocation line length occur at equal rates so that the structure remains constant on an average, see e.g. [21]. Frequently the minimum creep rate in the secondary stage of creep is taken to be the steady state rate of creep associated with the steady state dislocation structure and the increase of $\dot{\epsilon}$ in the tertiary stage of creep is related to formation of damage in the form of pores and microcracks. However, this is fundamentally wrong. This is seen from compression tests where creep fracture is suppressed because pores do not form [14, 15]. A tertiary stage of creep is observed in compression, too [22, 18, 14, 15]. However, in contrast to tensile creep the increase of $\dot{\epsilon}$ saturates as the material reaches a steady state of deformation at a level which is much higher than $\dot{\epsilon}_{\min}$ at the normal level of creep stresses σ. Consequently the dislocation structure is not in its steady state at $\dot{\epsilon}_{\min}$ [18]. This is quite clear from the fact that the steels in question are strongly predeformed on a local level in order to maintain material compatibility during the strong shearing associated with formation of martensite laths in the course of the martensitic phase transformation. The martensitic structure is then subjected to a tempering at elevated temperature in order to reduce internal stresses, recover the dislocation structure to some extent and precipitate solutes from the supersaturated solid solution of the martensite. The result is a subgrain structure within the prior austenite grain. The boundaries of the subgrains have low misorientations within a martensite block and high misorientations between blocks [23, 24, 25]. Even within a lath low-angle subgrain boundaries form as a result of dislocation pattern formation during deformation. The low-angle (sub-) grain boundaries constitute dislocation networks because the neighbouring subgrains are crystallographically coherent, the high-angle (sub-) grain boundaries have different properties as crystalline coherency between the neighbours is lost. The degree of disorientation leading to loss of coherency depends on the boundary character and lies in the order of 10 to 15° [26].

There is the well-established general rule that the subgrain size w, i.e. the spacing at which subgrain boundaries in the form cell walls or two-dimensional dislocation networks form, varies in inverse proportion to the stress σ normalized by the shear modulus G and takes values close to the steady state value (see e.g. [21])

$$w_\infty = k_w\, b\, \frac{G}{\sigma}\,. \tag{1}$$

b is the length of the Burgers vector and k_w is a constant taking the value of 10 for tempered martensite steels [14, 15, 27]. w is related to the mean free path of dislocations [28] which decreases with increasing stress as the dislocation density increases. The small value of the initial subgrain size w_0 after heat treatment of the steels in the order of 300 to 500 nm indicates that high stresses $> 500\,\mathrm{MPa}$ must have acted during martensitic transformation. During creep the initial dislocation structure is not stable as it tends to approach the steady state value determined by the creep stress. Therefore the subgrain

size will coarsen with time t the more strongly the lower the creep stress. Fig. 1 gives an example.

Coarsening of the subgrain structure requires transport of dislocations under stress, e.g. in the course of migration of subgrain boundaries leading to recombination of boundaries [29]. Under stress the boundaries move preferentially in a direction resulting in (positive) strain contributions. It is therefore natural that subgrain coarsening is strain controlled [14, 15, 30, 31]. The rate at which the subgrain size w approaches its steady state value w_∞ with time t results as:

$$\frac{\mathrm{d}\log w}{\mathrm{d}t} = \frac{\mathrm{d}\log w}{\mathrm{d}\epsilon}\,\frac{\mathrm{d}\epsilon}{\mathrm{d}t} = -\frac{\log w - \log w_\infty}{\epsilon_w}\cdot\dot{\epsilon}. \tag{2}$$

The growth constant ϵ_w for tempered martensite steels was found to be close to 0.12. It is smaller than the value 0.05 found for pure materials [18, 14, 15, 27]. This may be explained by the pinning of subgrain boundaries by precipitates leading to a higher fraction of immobile boundaries in the steels compared to pure material.

Subgrain boundaries form obstacles to motion of free dislocations moving individually through the subgrain structure and reduce the velocity of free dislocations. This is seen not only from the decrease of creep rate as the subgrain structure forms in recrystallized pure materials, but also from the effect which a change in subgrain size has on the creep rate of steels. It turns out that the expression for $\mathrm{d}\log w/\mathrm{d}\epsilon$ from (2) holds to a good approximation also in the case of cyclic deformation, if ϵ is replaced by the cumulative strain [32, 33, 34]. As the latter increases rapidly during cyclic straining there is fast subgrain growth under cyclic deformation at elevated temperatures and the corresponding stress levels. The precipitate structure is not expected to change within the short periods of cycling without hold periods. Therefore the increase of $\dot{\epsilon}$ in creep after cycling mainly reflects the effect of subgrain coarsening. And this effect may be quite large with an increase of minimum creep rate due to prior cyclic deformation by a factor of 6 [34, 33].

The modeling of subgrain hardening can be done by reducing the applied stress in the subgrain interior by an athermal stress component related to subgrain boundaries. Nes [28] proposed to calculate this stress component from the bowing of free dislocations between subgrain boundaries. Blum and coworkers [35, 36] proposed to calculate it from the composite model treating the material as a composite of the subgrain interior and the surrounding subgrain boundaries, where the two components do not differ in elastic behavior but in plastic deformation resistance, being higher for the subgrain boundary regions than for the subgrain interior. The two approaches are somewhat related, as both go back to bowing of the free dislocations [28, 37].

In order to maintain the creep resistance high in the course of time, it is necessary to suppress the coarsening of the subgrain structure, which can be done according to eq. (2) by keeping the creep rate $\dot{\epsilon}$ low. This is achieved by precipitation hardening. Therefore the evolution of the precipitate structure during heat treatment and creep is of prime importance for the creep resistance of the steels.

3. SOLUTES

Solute elements in the matrix affect the progress of inelastic strain in two ways. First, they act as obstacles against glide of dislocations. Second, they influence annihilation of dislocations.

There are two modes of glide (see e.g. [21]). At high stresses and low temperatures the dislocations move fast so that the solutes act as fixed obstacles to be overcome by thermally activated glide. At low stresses and high temperatures solutes have a chance to stick to the dislocations under the influence of their interaction with the dislocation stress field and form a cloud of solutes which is dragged along with the dislocations in a diffusive manner. In this case there is a proportional relation between the dislocation velocity and the stress component necessary for dragging [38]. The stress components due to dislocation-solute interaction are commonly called effective stress. They depend strongly on temperature and strain rate. During long-term creep the glide velocities are relatively low so that the effective stress component for dragging becomes low. However, the influence of solutes on structure evolution via annihilation of dislocations by climb still remains. E.g., a low diffusion coefficient of the solutes will reduce the velocity of climb and thereby reduce the rate of dislocation annihilation and the creep rate.

As the solute-dislocation interactions do not change during creep, solutes do not appear to be a significant cause for tertiary creep. However, an influence of solutes on the creep rate cannot be totally excluded in the case where solute elements like W precipitate from the matrix during creep; yet in view of the multitude of interstitial and substitutional solute elements this effect is not expected to be significant.

4. PRECIPITATES

The grain structure which is formed during the martensitic deformation is important for the process of precipitation of solute elements from solid solution in the course of heat treatment. Three types of precipitates may be distinguished, namely the precipitates which do not dissolve during austenization, those which form in the austenite before the martensitic transformation and those which form within the martensitic structure. The latter ones nucleate preferentially at the grain and subgrain boundaries. However, a fraction of the precipitates also nucleates within the interior of the subgrains. Once formed the precipitates are not stable as they coarsen by diffusive processes in order to save on phase boundary energy (Ostwald ripening).

As the different precipitate phases behave differently with regard to their nucleation, growth and coarsening, it is necessary to treat them separately. Previous attempts to distinguish the different phases only on the basis of their sizes [16, 39] led to erroneous results [40, 41]. Therefore it is necessary to characterize the precipitates by both their phase and their size. In addition their location within the dislocation structure is of obvious importance. The method of extracting the precipitates from the matrix has been found successful for analysing the precipitate structure [40, 42, 43]. In the extraction procedure the matrix around the precipitates is first etched away. A washing step follows where loose precipitates are removed from the surface so that only such particles remain which still have mechanical contact to the matrix (see Fig. 2). The precipitates standing out of the matrix after etching and washing are then enclosed in a C-film, extracted with the film (Fig. 2) and investigated individually in a transmission electron microscope.

The thermodynamic data base of Cr-steels is relatively well established and documented in software packages [44, 45]. One of the important precipitate phases is $M_{23}C_6$ (M: substitutional metallic element). This phase nucleates after the martensitic transformation preferentially at (sub-)grain boundaries. It is thermodynamically stable. In steels containing a sufficient amount of W, the intermetallic Laves phase $(Fe,Cr)_2(Mo,W)$ precipitates during creep [46, 16]; during the relatively high temperatures of tempering W

is in solid solution. Like $M_{23}C_6$, Laves phase nucleates heterogeneously at (sub-)grain boundaries. Its relatively fast growth results from precipitation and coalescence of neighbouring precipitates and need not be interpreted as Ostwald ripening. The phases MX (X: interstitial elements C or N) with M=V or Nb are important because they form not only at the (sub-)grain boundaries, but also within the subgrain interior leading to hardening there [47, 15, 16, 9, 48]. It is believed that VX is not stable, but metastable [9, 48, 49]. This results from the observation that the V-containing Z phase nucleates and grows after prolonged times at the expense of VX at elevated temperature [5, 50]. Depending on the conditions of heat treatment V may precipitate during heat treatment not only in the form of VX, but also as M_2X [9] which is regarded less stable than VX [47, 9].

As an example we describe the evolution of precipitates in two steels with 2 mass-% W and 5 mass-% Co designated as 5A and 5C during creep at 923 K [43]. Their compositions are given in Table 1. They stem from the same melt and differ only in heat treatment (Table 2). This leads to differences in the dislocation and precipitate structures. The initial subgrain size after heat treatment is smaller in 5C ($w_0 = 270\,\mathrm{nm}$) than in 5A (530 nm). The initial size of $M_{23}C_6$ is larger in 5C. This may be due to the slower cooling of 5C after austenitization leading to earlier nucleation at higher temperatures. Precipitation of W in Laves phase is similar in both steels. However, a qualitative difference exists with regard to precipitation of V which occurs in the form of VX in 5A, while one observes a majority of M_2X precipitates in 5C. This is consistent with the difference in tempering [9]. The low initial tempering temperature of 843 K promotes precipitation of V in the form of a less stable phase with lower V content. The final tempering is not sufficient to transform M_2X into VX. After 10^3 h of creep at 923 K one observes Z-phase at subgrain boundaries in 5C (similar to the case of Fig. 1), but not in 5A. The Z-phase precipitates rapidly become quite large with sizes similar to those of $M_{23}C_6$ and Laves phase. Concurrent with that, the volume fraction of M_2X is found to decrease. This is expected if Z-phase is more stable than M_2X.

The differences in evolution of precipitate structure in the two steels differing only in heat treatment correspond to the observed differences in creep strength [43]. While for times below 10^3 h 5C has longer creep life than 5A, the opposite holds for times above 10^3 h. The reason for this change does not lie in the minimum creep rate which for 5C is smaller than for 5A. Rather, the relatively fast increase in creep rate $\dot{\epsilon}$ of 5C with strain beyond $\dot{\epsilon}_{\min}$ (Fig. 3) is responsible for its reduced creep life.

5. PORES

It is well known that damage in the form of pores develops during creep (see e.g. [51, 38]). Nucleation of pores occurs at large second phase particles. Generally there is a transition from transgranular to intergranular creep fracture with decreasing stress. Pores are often considered to be the primary cause of termination of creep life. Typical spatial pore distributions are in use to characterize the residual creep life. However, pores generally do not grow independently of the creep strain under uniaxial stress. Rather, pore growth is constrained by the surrounding undamaged volume as the local stress in the volume around the pores is relaxed by the pores [51]. Thus overall creep strain has to proceed in order to replenish the stress around the pores necessary for pore growth. This explains the Monkman-Grant law (see e.g. [38]) establishing a direct relation between creep fracture time and $\dot{\epsilon}_{\min}$. This line of arguments is supported by the observation that pores become rare as the purity of the steels increases. While one is able to find pores in each stage

of creep upon intensive search [15], the overall porosity is much smaller in the tertiary stage of creep of modern modified Cr-steels compared to older ones [52]. This shows that creep life and ductility are not primarily determined by formation of pores, but by creep deformation which generates different porosities in different steels depending on the ease of pore nucleation.

6. DISCUSSION

6.1 Microstructural Evolution and Tertiary Creep

The question for the microstructural origin of creep life limitation of tempered martensite Cr-steels can now be answered. As explained in the preceding section, cavitation cannot be the decisive reason for the increase of creep rate in the tertiary stage of creep under conditions of uniaxial loading. While it certainly influences the final stage of tertiary creep short before fracture, the onset of tertiary creep with increase in $\dot{\epsilon}$ beyond $\dot{\epsilon}_{\min}$ is determined by the processes connected with dislocations and precipitates and it is this onset which terminates the slow creep at minimum rate and leaves only limited time till complete failure.

The evolution of the dislocation structure by coarsening under the relatively low creep stress is certainly a softening phenomenon which leads to increase of creep rate. However, as this coarsening occurs in a strictly strain and stress controlled manner, it would be the same in all steels starting with the same initial dislocation structure determined by austenitization, martensitic transformation and subsequent tempering. Therefore the dislocation structure alone cannot explain differences between more or less creep resistant steels.

The conclusion is that the precipitates play the most important role in determining the rate of creep for a given initial dislocation structure and therefore the onset of tertiary creep. The attractive interaction between precipitates and grain boundaries stabilizes the latter against migration (see e.g. [53]). However, it is important that the precipitates appear as small particles in fine distribution; large incoherent precipitates at high-angle grain boundaries will lead to easy nucleation of pores and microcracks. The stabilization is particularly important with regard to subgrain boundaries of the small-angle type. Being dislocation networks which generally carry a tilt component, they are driven to migrate under stress and thereby contribute to creep strain (the volume which is covered by a subgrain boundary with tilt component Θ is sheared by an amount equal to Θ). Precipitates distributed along the boundaries exert a back stress (Zener drag) as the boundaries have to bow out between them. It is well possible that subgrain boundaries which are heavily loaded with precipitates are unable to migrate at all. In any case the rate of migration of low-angle grain boundaries will be reduced by the precipitates which have nucleated there. These precipitates will, however, have little effect on the velocity of dislocations moving individually through the subgrain interior. An important strengthening effect is therefore generated by those precipitates which form in the subgrain interior. These will hinder dislocation motion through the subgrains by forcing the dislocations to bow between them due to repulsive (Orowan stress) or attractive interaction (detachment stress).

6.2 Microstructural Modelling

According to the above creep is a complex process involving a number of interacting

subprocesses. The composite model in the form MIKORA has been set up to capture this complexity [54, 55, 16, 17, 56]. The model is partly empirical in nature by describing the evolution of the dislocation structure in a phenomenological manner based on experimental observations of the spacings between dislocations within the subgrains, between subgrain boundaries and between the dislocations in the subgrain boundaries. The strengthening effect of precipitates is taken into account by expressions for athermal stress components due to precipitates which are subtracted from the local stresses in the soft subgrain interior and the hard subgrain boundaries. The expressions for the dislocation velocities are based on glide of dislocations in the solid solution of the subgrain interior and through the dislocation network of the subgrain boundaries. It has been possible to fit the model to experimental data for a number steels [55, 16, 56]. The softening related with coarsening of the initial dislocation structure and with coarsening of precipitates has successfully been described. These two processes lead to increase of $\dot{\epsilon}$ in the tertiary stage of creep which is the same in tension and compression. The final stage of tertiary creep where the results of tensile and compressive creep differ, because fracture is suppressed in compression, has not been modelled so far; however, it is of little importance as it contributes negligibly to overall creep life. The creep life can thus be well estimated from the model once the fracture strain is approximately known.

In the present state the model treats the material as a homogeneous body. Matsui and coworkers [57, 58] have drawn attention to the fact that the steels may not behave in a homogeneous manner during long-term creep. They propose that there is preferential dynamic recovery at prior austentite grain boundaries where deformation becomes concentrated and leads to intergranular fracture. These processes may require attention when the model is fitted to experimental results.

6.3 Reasons for Enhanced Loss of Creep Strength

The model is able to explain the unexpectedly strong increase of tertiary creep rate observed in the case of steel 5C (Fig. 3). The point is that elimination of precipitation hardening in the subgrain interior by dissolution of small V-bearing precipitates of types VX or M_2X causes a significant extra increase of $\dot{\epsilon}$ [56] which is not compensated by the additional strengthening of the subgrain boundaries by relatively few additional precipitates of Z-phase.

So far the precipitation of stable V-bearing Z-phase has been proposed to be the main cause of loss of precipitation hardening in the subgrain interior [9, 49, 10]. However, the phase M_2X may play an important role as well [43]. It has been observed that M_2X coarsens rapidly (Fig. 4) at subgrain boundaries. The reason may be loss of coherency being easier at the boundaries than within the subgrains. The large M_2X precipitates at the boundaries lead to dissolution of the small ones in the subgrain interior. Thus M_2X will also cause anomalous loss of creep resistance independent of Z phase.

The presence of large incoherent M_2X and Z-phase may be related [43]. Being the most stable among the V-bearing phases, the precipitation of Z is not controlled by thermodynamic stability, but by the precipitation kinetics which is controlled by nucleation. Generally a stable phase with large specific phase boundary energy has difficulties to nucleate. Therefore nucleation is heterogeneous. The large M_2X particles at the subgrain boundaries will constitute favourable nucleation sites for Z-phase due to their high phase boundary energy and their composition being similar to that of Z-phase. Once nucleated near M_2X, Z-phase may grow rapidly and transform the M_2X particle. This would explain

why small precipitates of Z-phase are rarely found, why the morphologies of M_2X and Z-phase as thin, relatively transparent plates are strikingly similar and why Z-phase is not found (within the time of observation) in steel 5A where M_2X was not observed.

A different explanation of degradation of creep strength in the steels has recently been proposed recently by Maruyama and Lee [59]. These authors observed that the kinetics of creep differ at high and low stresses. They showed that the creep rupture times can successfully be predicted on the basis of the Larson-Miller approach taking these differences into account. Such differences must have a microstructural origin. Maruyama and Lee propose to consider the change in fracture mode from transgranular at high stresses to intergranular at low stresses as the cause for accelerated loss of creep resistance in steels with high short-term creep strength. This implies that the onset of tertiary creep is controlled by the fracture process, not by the deformation process. However, it is questionable whether the change in fracture process is the primary microstructural cause for accelerated degradation of creep resistance. In the case of steel 5C treated above the fracture strain is 0.322 while the degradation of creep resistance starts at a strain of $\epsilon = 0.001$. It is well possible that the change in fracture mode is a result of changes in the dislocation and precipitate structures. Removal of strengthening precipitates from the subgrain interior will put the subgrain boundaries under higher stress. In addition, more large incoherent precipitates are created there which may be sites of pore nucleation. The disappearance of strengthening particles from the neighborhood of the (sub-)grain boundaries will make this range particularly soft. This will localize deformation in those regions and cause localized subgrain coarsening as observed [57, 58].

7. CONCLUDING REMARKS

The creep life of tempered martensite steels is primarily limited by increase of creep rate in tertiary creep caused by microstructural coarsening of dislocation structure and precipitates. The coarsening of precipitates acts directly by decrease of precipitation hardening and indirectly by accelerating subgrain coarsening. Coarsening of precipitates occurs by Ostwald ripening of existing phases as well as by replacement of small metastable precipitates by large, more stable ones. The heat treatment of the steels is important in achieving a relatively stable structure by avoiding relatively instable phases like M_2X, which coarsens fast and may act as nucleation site for Z phase, and in encouraging precipitation of relatively stable MX which strengthens not only the subgrain boundary regions, but also the subgrain interior. In addition, the coarsening of precipitates by Ostwald ripening should be minimized. These goals can only be attained by careful control of all relevant alloying elements, e.g. N and B [60].

ACKNOWLEDGMENTS

Thanks are due to the Deutsche Forschungsgemeinschaft (project BL135/27), the Bundesministerium für Wirtschaft und Arbeit (project 0327055A), the industrial partners within this project and the Bundesministerium für Bildung und Forschung (IND 00/025) for financial support and to Dipl.-Ing. T. Seibert and Dr.-Ing. K. Durst, Dr. K. Kimura and Prof. K. Maruyama for stimulating discussions.

References

[1] K. H. Mayer, R. Hanus, T. Kern, M. Staubli, and D. V. Thorton. In Proceedings of the 6th Liege Conference *Materials for Advanced Power Engineering 1998*. (eds) J. Lecomte-Beckers, M. Carton, F. Schubert, and P. J. Ennis, EUROPEAN COMMISSION UNIVERSITE DE LIEGE, Schriften des Forschungszentrum Jülich, Reihe Energietechnik / Energy Technology Volume 5, (1998) Vol 1, p 71.

[2] M. Staubli, K. H. Mayer, T. U. Kern, R. W. Vanstone, R. Hanus, J. Stief, and K. H. Schönfeld. In Proc. of the 3rd Conference *Advances in materials technology for fossil power plants* (eds) R. Viswanathan, W.T. Bakker, and J. D. Parker, The Institute of Materials. London (2001), p 15.

[3] F. Masuyama. *ISIJ International* 41 (2001) 612.

[4] F. Abe, H. Okada, S. Wnanikawa, M. Tabuchi, T. Itagaki, K. Kimura, K. Yamaguchi, and M. Igarashi. In Proceedings of the 7th Liege Conference *Materials for Advanced Power Engineering 2002*, (eds) J. Lecomte-Beckers, M. Carton, F. Schubert, and P. J. Ennis, EUROPEAN COMMISSION UNIVERSITE DE LIEGE, Schriften des Forschungszentrum Jülich, Reihe Energietechnik / Energy Technology Volume 21, (2002) Vol 3, p1397.

[5] A. Strang and V. Vodarek. *Materials Science and Technology* 12 (1996) 552.

[6] F. Abe. *Mater. Sci. Eng. A* 234-236 (1997) 1045.

[7] K. Sawada, M. Takeda, K. Maruyama, R. Ishii, M. Yamada, Nagae Y., and R. Komine. *Mater. Sci. Eng. A* 267 (1999) 19.

[8] T. Fujita. as in [2],p 33.

[9] G. Götz and W. Blum. *Mater. Sci. Eng. A* 348/1-2 (2003) 201.

[10] J Hald. In *Werkstoffe und Qualitätssicherung 2004*, VGB, Dortmund (2004).

[11] G. Eggeler, N. Nilsvang, and B. Ilschner. *steel research* 58 (1987) 97.

[12] G. Eggeler. *Acta metall.* 37 (1989) 3225.

[13] W. Blum and S. Straub. *steel research* 62 (1991) 72.

[14] S. Straub, M. Meier, J. Ostermann, and W. Blum. *VGB Kraftwerkstechnik* 73 (1993) 646.

[15] S. Straub. *Verformungsverhalten und Mikrostruktur warmfester martensitischer 12%-Chromstähle*. Fortschr.-Ber. VDI Reihe 5 Nr. 405. VDI Verlag, Düsseldorf, (1995).

[16] P. Polcik. *Modellierung des Verformungsverhaltens der warmfesten 9-12%Chromstähle im Temperaturbereich von 550–650°C*. D29 (Dissertation Universität Erlangen-Nürnberg). Shaker Verlag, Aachen (1999).

[17] D. Henes, H. Möhlig, S. Straub, J. Granacher, W. Blum, and C. Berger. In *Microstructure and Mechanical Properties of Metallic High-Temperature Materials* (eds) H. Mughrabi, G. Gottstein, H. Mecking, H. Riedel, and J. Tobolski, Wiley-VCH, Weinheim (1999) p 179.

[18] W. Blum, S. Straub, and S. Vogler. In Proc. 9th Int. Conf. *Strength of Metals and Alloys (ICSMA 9)* , (eds) D. G. Brandon, R. Chaim, and A. Rosen, Freund Publishing House, London (1991) Vol. I, p 111.

[19] W. Blum. In *The Johannes Weertman Symposium* (eds) R. W. Arsenault, D. Cole, T. Gross, G. Kostorz, P. Liaw, S. Parameswaran, and H. Sizek,The Minerals, Metals & Materials Society, Warrendale (1996) p 103.

[20] W. Blum. *Mater. Sci. Eng. A* 319-321 (2001) 8.

[21] W. Blum. In *Plastic Deformation and Fracture of Materials*, *Materials Science and Technology, ed. by Cahn, R. W. and Haasen, P. and Kramer, E. J.*, (ed) H. Mughrabi, VCH Verlagsgesellschaft, Weinheim (1993) Vol 6, p 3.

[22] W. Blum and S. Straub. In VIIIth Int. Symp. *Creep-Resistant Metallic Materials* Zlín, Czechoslovakia (1991) p 178.

[23] S. Straub, W. Blum, and H. Mughrabi. Link OPAL application note, Oxford Instruments Microanalysis Group, High Wycombe Bucks, England (1996).

[24] F. Yoshida, D. Terada, H. Nakashima, H. Abe, H. Hayakawa, and S. Zaefferer. as in [2], p 143.

[25] A. Dronhofer, J. Pešička, A. Dlouhý, and G. Eggeler. *Z. Metallkd.* 94 (2003) 511.

[26] A. H. Cottrell. *An introduction to metallurgy.* Edward Arnold Ltd., London (1968).

[27] S. Straub and W. Blum. In Proc. of the Inter. Symp. *Hot Workability of Steels and Light Alloys-Composites*, (eds) H. J. McQueen, E. V. Konopleva, and N. D. Ryan, Montréal (1996) p 189.

[28] E. Nes. *Progr. Mater. Sci.*, 41 (1998) 129.

[29] M. Biberger and W. Blum. *Phil. Mag. A*, 65 (1992) 757.

[30] W. Blum and G. Götz. *Steel Research*, 70 (1999) 274.

[31] Y. Qin, G. Götz, and W. Blum. *Mater. Sci. Eng. A*, 341 (2003) 211.

[32] H. Chilukuru, W. Blum, M. Schwienheer, and A. Scholz. In *Langzeitverhalten warmfester Stähle und Hochtemperaturwerkstoffe, Beiträge zur 26. Vortragsveranstaltung der Arbeitsgemeinschaft für warmfeste Stähle und für Hochtemperaturwerkstoffe am 28. November in Düsseldorf*,Stahlinstitut VDEh, (2003) p 65.

[33] W. Blum. Creep Simulation. In *Continuum Scale Simulation of Engineering Materials Fundamentals, Microstructures, Process Applications*, (eds) L.-Q. Chen, F. Barlat, F. Roters, and D. Raabe, VCH Wiley, (2004).

[34] J.S. Dubey, H. Chilukuru, J.K. Chakravartty, M. Schwienheer, A. Scholz, and W. Blum. *Materials Science and Engineering A*, 406 (2005) 152.

[35] S. Vogler and W. Blum. In *Creep and Fracture of Engineering Materials and Structures*, (eds) B. Wilshire and R.W. Evans, The Institute of Metals, London (1990) p 65.

[36] R. Sedláček and W. Blum. *Comp. Mater. Sci.*, 25 (2002) 200.

[37] R. Sedláček and W. Blum. *Comp. Mater. Sci.*, 13 (1998) 148.

[38] J. Čadek. *Creep in metallic materials*. Elsevier, Amsterdam, (1988).

[39] P. Polcik, T. Sailer, W. Blum, S. Straub, J. Buršik, and A. Orlová. *Mater. Sci. Eng. A*, 260 (1999) 252.

[40] G. Götz, Y. Qin, and W. Blum. as in [2], p 155.

[41] Y. Qin, G. Götz, W. Blum, and Z.G. Zhu. *J. of Alloys and Compounds*, 352 (2003) 260.

[42] T. Seibert, K. Durst, H. Chilukuru, W. Blum, and M. Göken. In *37. Praktischen Metallographie Sonderbände - Fortschritte in der Metallographie*, (ed) Mathias Göken, DGM, Erlangen (2005) p 73.

[43] R. Agamennone, W. Blum, C. Gupta, J. K. Chakravartty, Y. Wang, and A. Scholz. *Mater. Sci. Eng. A*, to be submitted.

[44] B. Sundman, B. Jansson, and J-O. Andersson. *Calphad*, 9 (1985) 153.

[45] A. Borgenstamm, A. Engström, L. Höglund, , and J. Ågren. *Journal of Phase Equilibria*, 21 (200) 269.

[46] F. Abe. *Mater. Sci. Eng. A*, 319-321 (2001) 770.

[47] J. Hald. *Steel Research*, 67 (1996) 369.

[48] M. Taneike, F. Abe, and K. Sawada. *Nature*, 424 (2003) 294.

[49] F. Abe. *Current Opinion in Solid State and Materials Science*, 8:305–311, 2004.

[50] K. Kimura, K. Suzuki, Y. Toda, H. Kushima, and F. Abe. as in [4], p 1171.

[51] H. Riedel. *Fracture at High Temperatures*. Springer, Berlin (1987).

[52] W. Bendick, B. Hahn, and W. Schendler. as in [2], p 299.

[53] O. Hundri, E. Nes, and N. Ryum. *Acta. metall*, 33 (1985) 11.

[54] P. Polcik, S. Straub, and W. Blum. In 4th European Conference *Advanced Materials and Processes*, Associatione Italiana di Metallurgia, Mailand (1995) p 313.

[55] P. Polcik, S. Straub, D. Henes, and W. Blum. In *Microstructural Stability of Creep Resistant Alloys for High Temperature Plant Applications* Materials Research Institute, Sheffield (1997).

[56] X. H. Zeng and W. Blum. In *29th MPA Seminar, Safety and Reliability in Energy Technology, Oct 2003*, Stuttgart (2003).

[57] K. Kimura, Ohi. N., K. Shimazu, T. Matsuo, R. Tanaka, and M. Kikuchi. *Scripta Metallurgica*, 21 (1987) 19.

[58] K. Kimura. In Proc. of symposium *Creep Deformation and Fracture, Design, and Life Extension, Materials Science & Technology 2005* (eds) R.S. Mishra, J.C. Earthman, S.V. Raj, and R. Viswanathan, TMS, Warrendale (2005) p 97.

[59] K. Maruyama and J. S. Lee. In *ECCC Creep Conference*, London (2005) p 372.

[60] F Abe. as in [58], p 117.

TABLES

Cr	C	Si	W	Nb	V	Co	N	Mo	Mn	B
12.00	0.159	0.469	1.99	0.065	0.215	4.81	0.0315	0.176	0.102	<0.001

Table 1: Composition of steels 5A and 5C

Alloys	Austenitization	Temper
5A	1343 K/0.5h/air	1033 K/2h/air
5C	1373 K/0.5h/-3.5Kmin^{-1}	843 K/10h + 973 K/8h

Table 2: Heat treatments for steels 5A and 5C

FIGURE CAPTIONS

Fig. 1: Coarsened subgrain structure (TEM) in steel similar to 5A/5C after tensile creep (923 K, 100 MPa, $\epsilon = 0.266$, 3512 h); arrows mark Z-phase precipitated at the subgrain boundaries. From [43].

Fig. 2: Microstructure (high resolution SEM) of steel (composition similar to Table 1, but no Co and 0.10%C) in initial state after heat treatment; left: surface after etching and washing according to first step of extraction replica preparation with precipitates on top of peaks, right: replica [42].

Fig. 3: Maximum slopes $\mathrm{d}\log\dot{\epsilon}/\mathrm{d}\epsilon$ during tertiary creep as function of σ. Higher slopes in steel 5C indicate more rapid increase of $\dot{\epsilon}$ and shorter creep life compared to 5A.

Fig. 4: Typical M_2X precipitates in steel from Fig. 2; left: small particle in initial state, right: strongly coarsened particle after cyclic deformation (873 K, 11 kh) and subsequent creep (923 K, 800 h, 98 MPa).

FIGURES

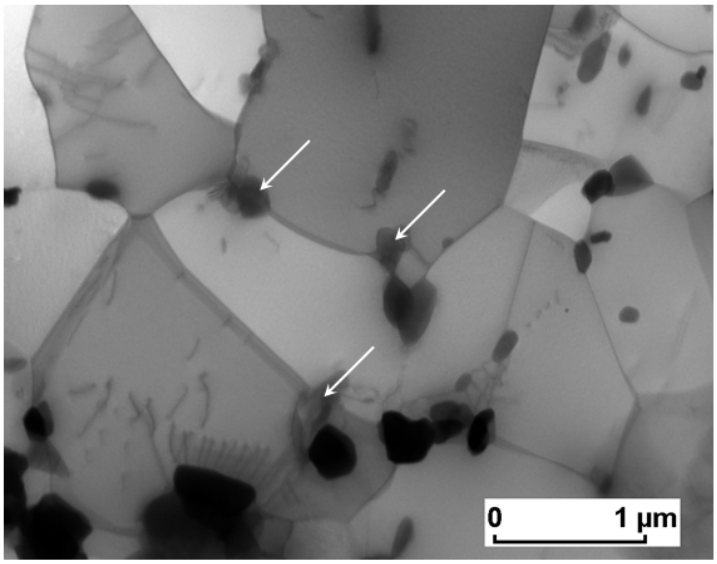

Figure 1: Coarsened subgrain structure (TEM) in steel similar to 5A/5C after tensile creep (923 K, 100 MPa, $\epsilon = 0.266$, 3512 h); arrows mark Z-phase precipitated at the subgrain boundaries. From [43].

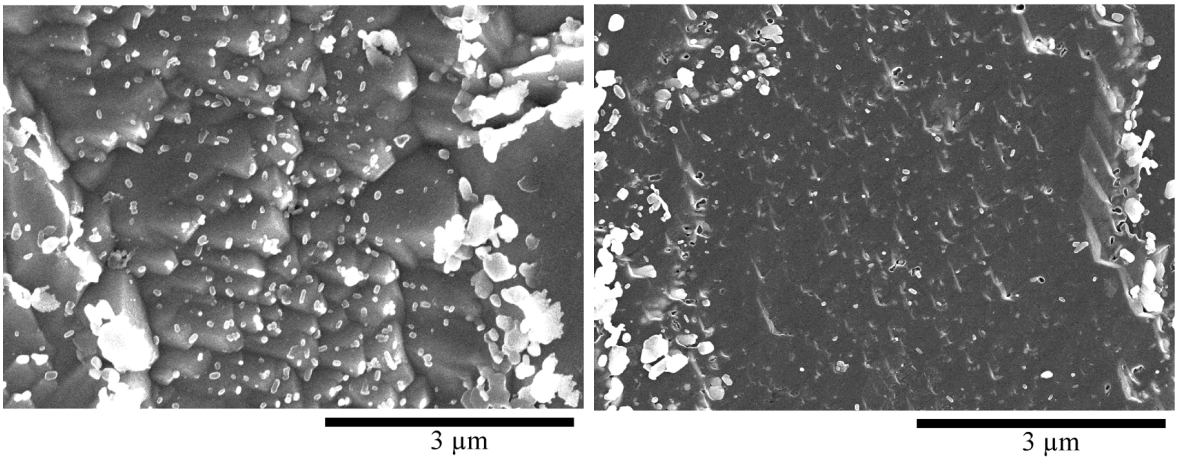

Figure 2: Microstructure (high resolution SEM) of steel (composition similar to Table 1, but no Co and 0.10%C) in initial state after heat treatment; left: surface after etching and washing according to first step of extraction replica preparation with precipitates on top of peaks, right: replica [42].

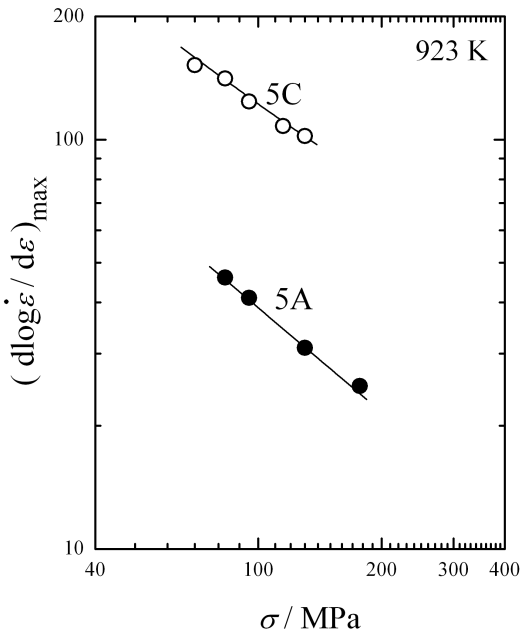

Figure 3: Maximum slopes $\mathrm{d}\log\dot{\epsilon}/\mathrm{d}\epsilon$ during tertiary creep as function of σ. Higher slopes in steel 5C indicate more rapid increase of $\dot{\epsilon}$ and shorter creep life compared to 5A.

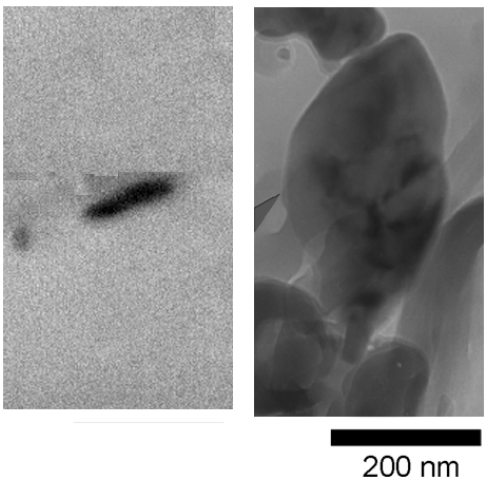

Figure 4: Typical M_2X precipitates in steel from Fig. 2; left: small particle in initial state, right: strongly coarsened particle after cyclic deformation (873 K, 11 kh) and subsequent creep (923 K, 800 h, 98 MPa).

G Microstructural data

State		**Initial**					
Alloy		**1A**	**3A**	**4A**	**5A**	**6A**	**7A**
T/K		293	293	293	293	293	293
Versuchszeit/ h							
σ/MPa		0	0	0	0	0	0
$\dot{\epsilon}/\mathrm{s}^{-1}$							
ϵ_{inel}		0	0	0	0	0	0
Probe		1AIn	3AIn	4AIn	5AIn	6AIn	7AIn
$A/\mu\mathrm{m}^2$			89	190	185	74	
N			230	385	244	143	
$w/\mu\mathrm{m}$			0.387 ± 0.03	0.492 ± 0.14	0.758 ± 0.27	0.520 ± 0.23	
$w_{(0.5)}/\mu\mathrm{m}$			0.287 ± 0.02	0.442 ± 0.04	0.488 ± 0.21		
$w_{(0.84)}/w_{(0.159)}$			3.97 ± 0.9	3.23 ± 1.14	5.57 ± 2.76		
$A/\mu\mathrm{m}^2$							7.9
N							167
δ							0.219 ± 0.19
$A/\mu\mathrm{m}^2$		7.8	28	52.2	27.58	17.23	
N		328	386	429	450	362	
$\mathrm{M_{23}C_6}$	d_{p}/nm	74 ± 5	112 ± 10	151 ± 22	94 ± 12	110 ± 11	
	f_{p}	0.051 ± 0.018	0.113 ± 0.058	0.053 ± 0.039	0.134 ± 0.039	0.135 ± 0.045	
MX	d_{p}/nm	34 ± 8	41 ± 12	51 ± 6	42 ± 21	34 ± 5	
	f_{p}	0.00039 ± 0.000029	0.00049 ± 0.00014	0.0023 ± 0.00032	0.00095 ± 0.0007	0.0129 ± 0.01	
$\mathrm{M_2X}$	d_{p}/nm	25 ± 1	43 ± 23				
	f_{p}	0.0155 ± 0.0065	0.0044 ± 0.004				

State		**Cycled**					
Alloy		**1A**				**2A**	**2A-Head**
T/K		873	873	873	873	873	873
Halteperioden/zyklus		0	2	2	4	4	
Haltezeit/ h/zyklus		0	0.1	0.1	10	3.2	
Versuchszeit/ h		13	154	72	11119	2317	2317
N_A		3513	1491	757	1119	724	
$\triangle\epsilon_{mech}/\%$		0.65	0.65	0.92	0.65	0.70	
Probe		uA16d3	uA16dh2	uA16dh4	uA16bp2	uB16b1	uB16b1
$A/\mu m^2$		702	315	340	2162	1731	341
N		911	353	352	1396	1125	657
$w/\mu m$		0.77 ± 0.06	0.894 ± 0.196	0.967 ± 0.14	1.54 ± 0.13	01.53 ± 0.18	0.519 ± 0.04
$w_{(0.5)}/\mu m$		0.648 ± 0.03	0.781 ± 0.21	0.787 ± 0.14	1.162 ± 0.19	1.12 ± 0.16	0.413 ± 0.02
$w_{(0.84)}/w_{(0.159)}$		3.41 ± 0.36	3.52 ± 0.52	3.85 ± 0.74	3.61 ± 0.16	5.21 ± 0.49	3.29 ± 0.56
$A/\mu m^2$						376	
$\delta/\mu m$						0.713 ± 0.093	
$A/\mu m^2$		25.3					
N		515					
$M_{23}C_6$	d_p/nm	112 ± 14					
	f_p	0.0323 ± 0.02					
MX	d_p/nm						
	f_p						
M_2X	d_p/nm	39 ± 3					
	f_p	0.0043 ± 0.003					
Laves	d_p/nm						
	f_p						
Z-Phase	d_p/nm						
	f_p						

State		**Cycled and Crept**		
Alloy		**1A**		**2A**
T/K		923	923	923
Kreichversuchszeit/ h		1054	708	200
σ/MPa		98	98	98
ϵ_{inel}		0.089	0.159	0.112
Probe		uA16d3+crept	uA16bp2+crept	uB16b1+crept
$A/\mu\text{m}^2$			657	803
N			415	622
w/μm			1.58 ± 0.17	01.29 ± 0.43
$w_{(0.5)}/\mu$m			1.31 ± 0.11	
$w_{(0.84)}/w_{(0.159)}$			3.51 ± 0.39	
$A/\mu\text{m}^2$		94	64.6	
N		528	420	
$M_{23}C_6$	d_{p}/nm	171 ± 8	200 ± 49	
	f_{p}	0.088 ± 0.03	0.0809 ± 0.038	
MX	d_{p}/nm	63 ± 6	57 ± 23	
	f_{p}	0.00027 ± 0.0001	0.00014 ± 0.0001	
M_2X	d_{p}/nm	121 ± 10	145 ± 68	
	f_{p}	0.01 ± 0.007	0.027 ± 0.026	
Laves	d_{p}/nm		100 ± 160	
	f_{p}		0.00044 ± 0.00077	
Z-Phase	d_{p}/nm	60 ± 18	105 ± 37	
	f_{p}	0.00017 ± 0.0007	0.0018 ± 0.0025	

State		**Crept**			**Crept (3Az5w) and Heat treated**	
Alloy		**3A**		**4A**	**3A**	
T/K		873	873	873	923	973
Versuchszeit/ h		14598	47262	15821	1000	1000
σ/MPa		160	125	90		
ϵ_{inel}		0.177	0.175	0.04		
Probe		3Az4	3Az5w	4Az6	3Az5w+ht1	3Az5w+ht1+ht2
$A/\mu\text{m}^2$			358	484		
N			360	618		
w/μm			0.99 ± 0.26	0.783 ± 0.04		
$w_{(0.5)}/\mu$m			0.781 ± 0.2	0.676 ± 0.11		
$w_{(0.84)}/w_{(0.159)}$			3.53 ± 0.5	3.19 ± 0.23		
$A/\mu\text{m}^2$		61	46	76	72	111
N		466	323	327	303	368
$M_{23}C_6$	d_{p}/nm	157 ± 9	192 ± 7	163 ± 31	208 ± 3	237 ± 36
	f_{p}	0.12 ± 0.02	0.15 ± 0.008	0.073 ± 0.034	0.104 ± 0.03	0.12 ± 0.007
MX	d_{p}/nm	66 ± 6	60 ± 12	70 ± 11	70 ± 20	84 ± 5
	f_{p}	0.00027 ± 0.00013	0.0023 ± 0.003	0.00056 ± 0.0003	0.00025 ± 0.0002	0.00035 ± 0.0003
M_2X	d_{p}/nm	89 ± 10	103 ± 18		136 ± 10	205 ± 34
	f_{p}	0.007 ± 0.00165	0.0075 ± 0.004		0.0068 ± 0.003	0.001 ± 0.0003
Z-Phase	d_{p}/nm	50 ± 6	101 ± 67		71 ± 4	145 ± 18
	f_{p}	$0.0006 \pm 5E-5$	0.0012 ± 0.01		0.0012 ± 0.001	0.0015 ± 0.0052

List of Symbols

A . untersuchte Fläche
d_p Ausscheidungsgröße
ϵ .. Dehnung
$\dot{\epsilon}$ .. Dehnrate
f_p . Volumenanteil der Ausscheidungen
N_A Anrisswechselzahl
δ .. Abstand freier Versetzungen
σ . Spannung
T . Temperatur
w . Subkorngröße

G.1 Grain size

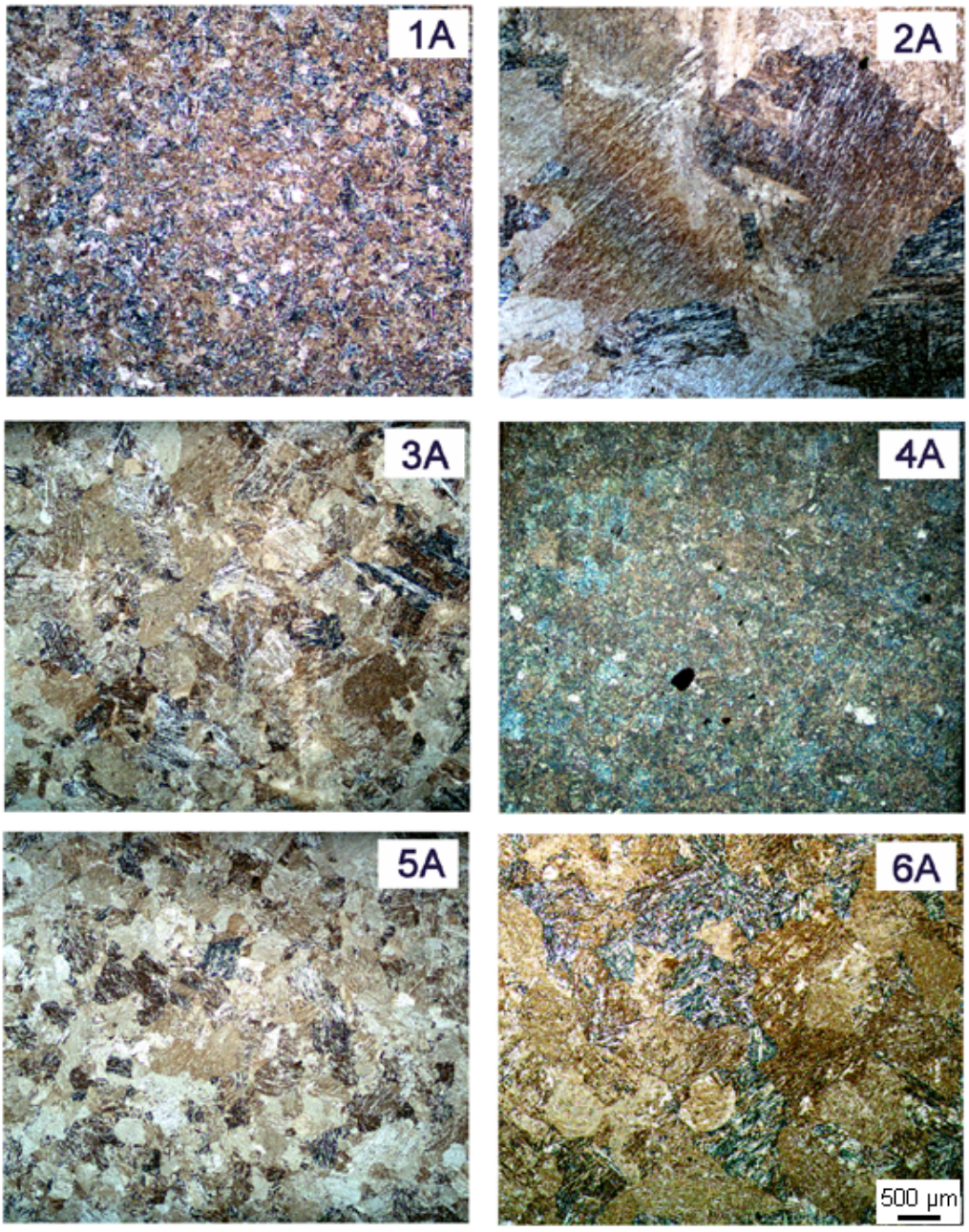

Abbildung 16: Prior austenite grain structure of the steels after heat treatment

G.2 Dislocation structures

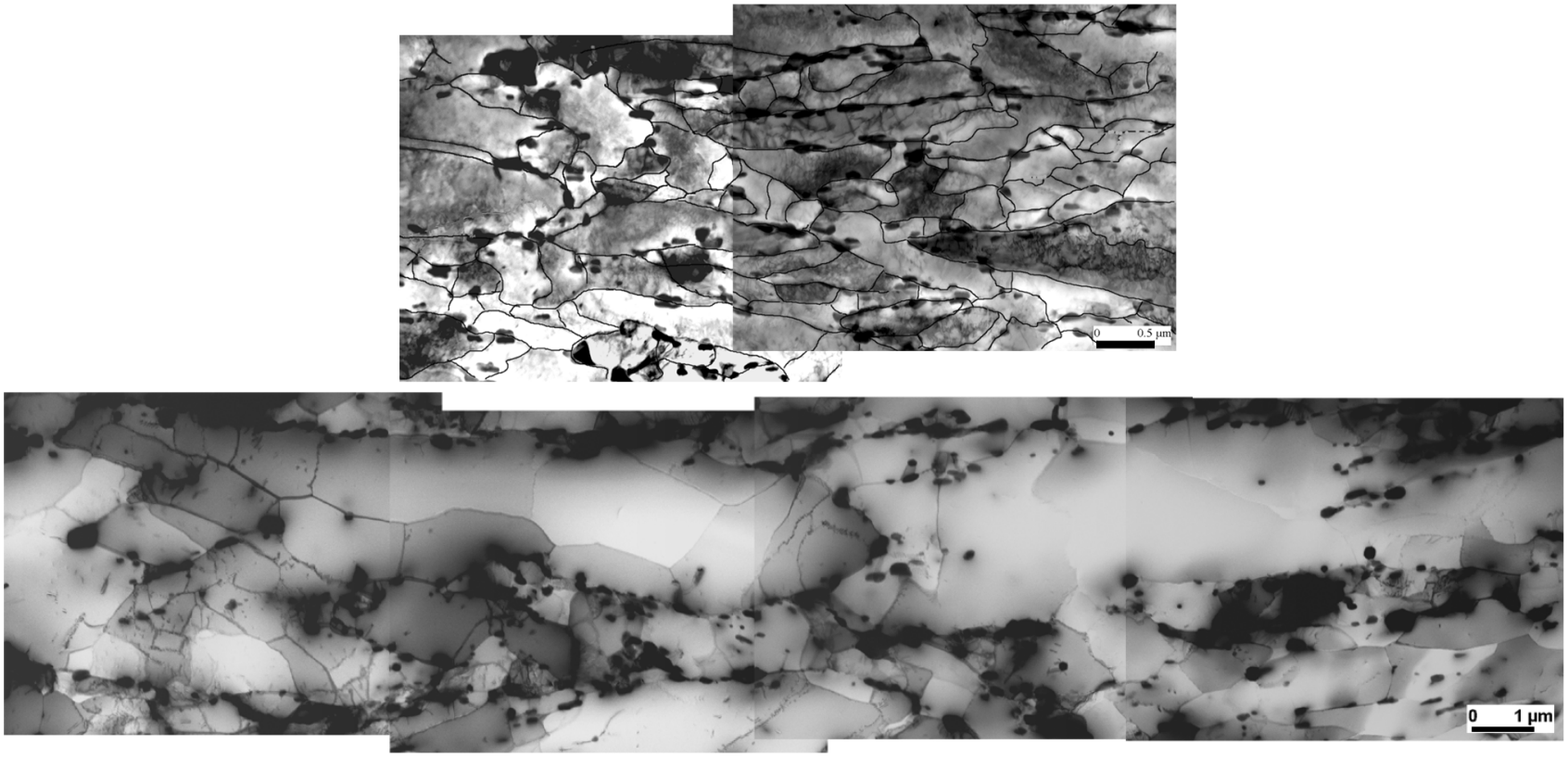

Abbildung 17: 3A microstructures. top: After heat treatment, bottom: crept at 125 MPa at 600 °C.

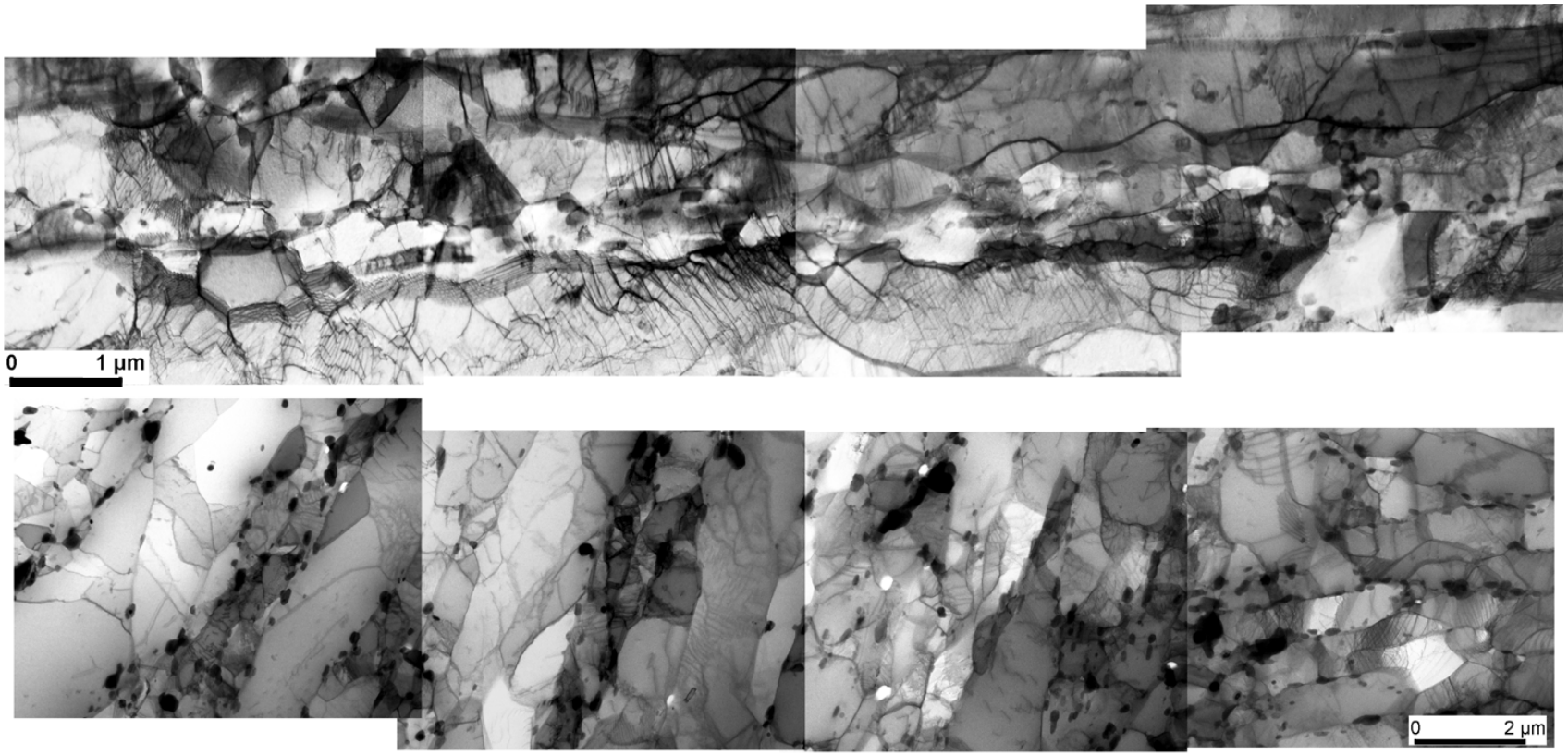

Abbildung 18: 4A microstructures. top: After heat treatment, bottom: crept at 90 MPa at 600 °C.

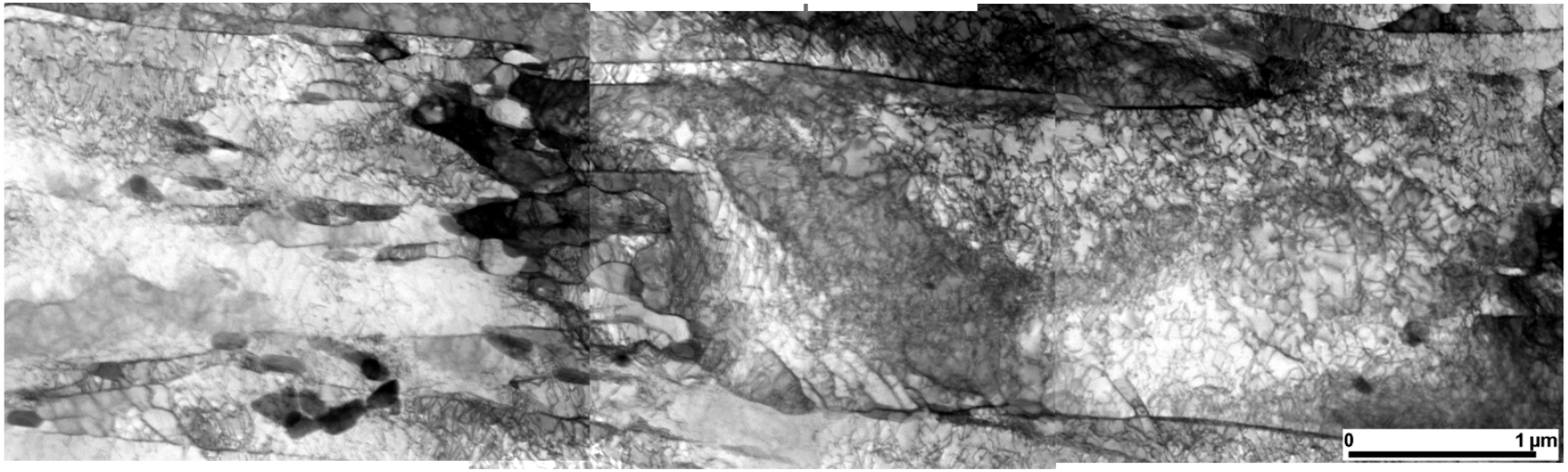

Abbildung 19: 5A microstructure after heat treatment.

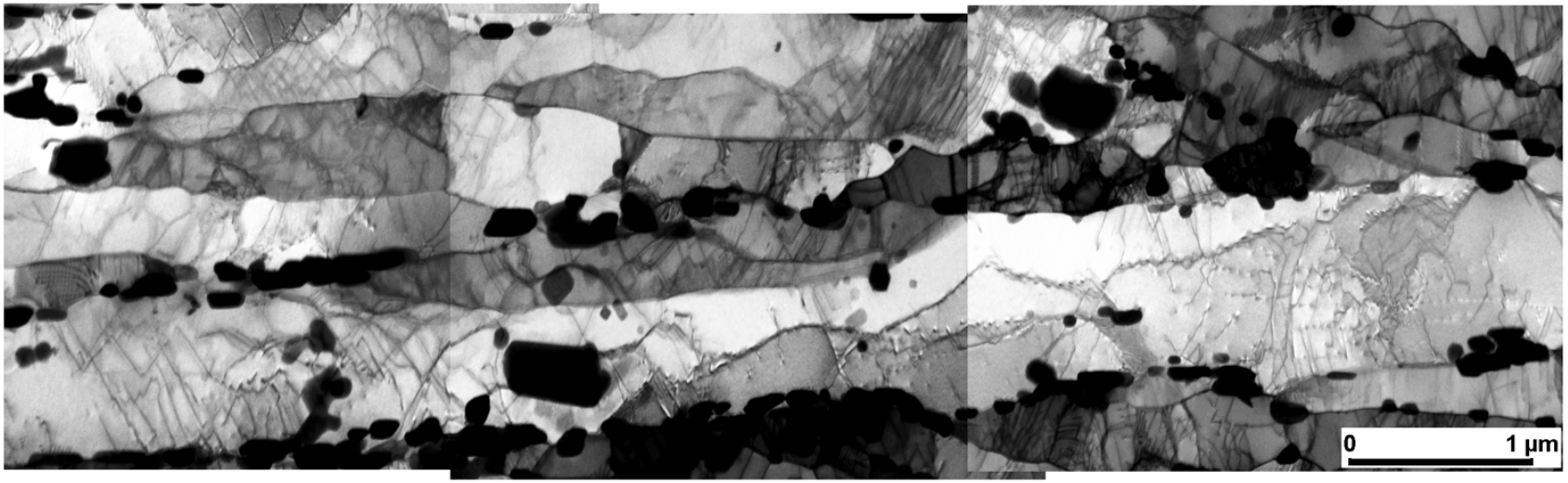

Abbildung 20: 6A microstructure after heat treatment.

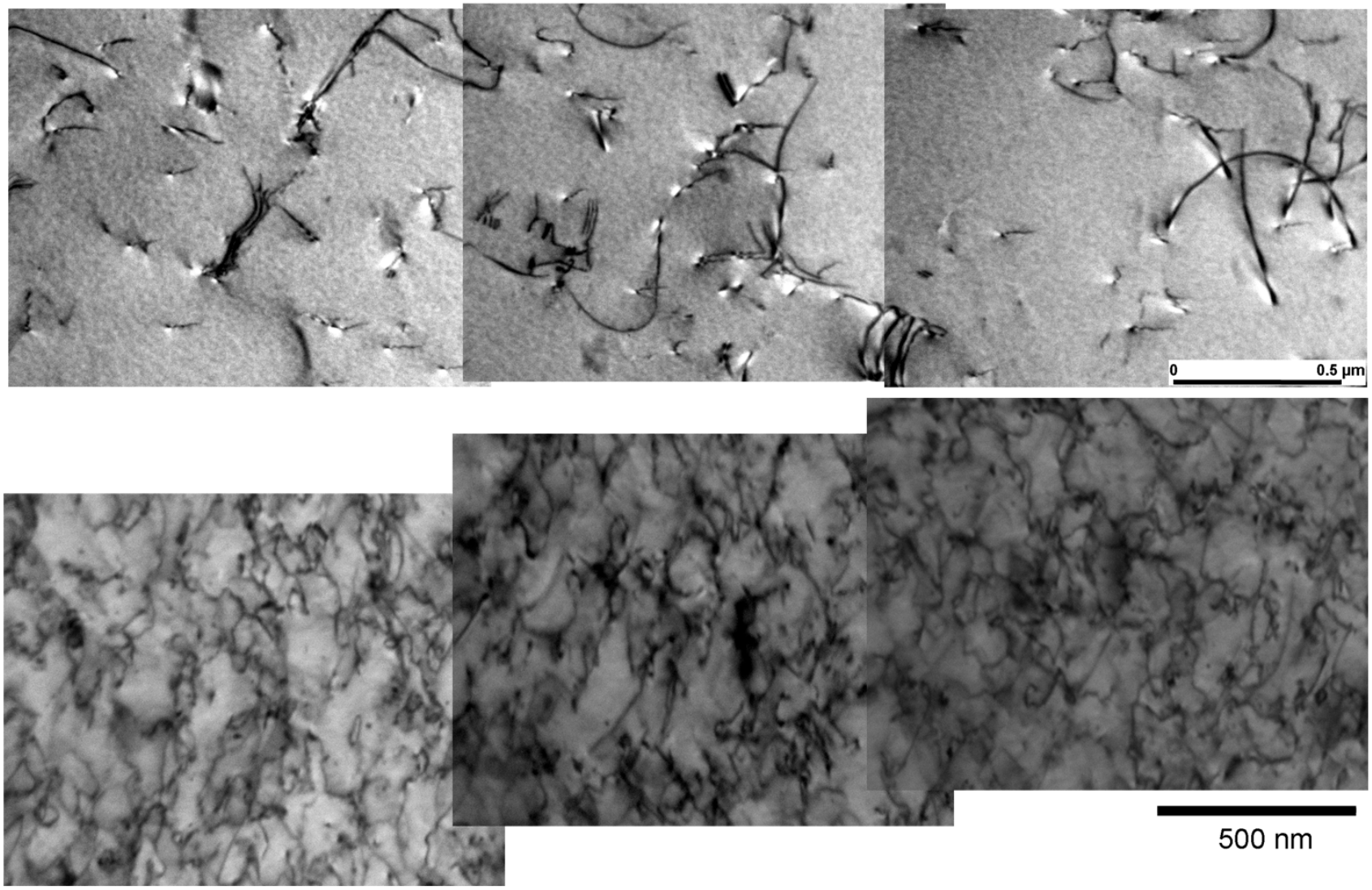

Abbildung 21: 7A microstructures. top: After heat treatment, bottom: crept at 380 MPa at 650 °C.

G.3 Particle structures

G.3.1 1A

Precipitate structure evolution in 1A.

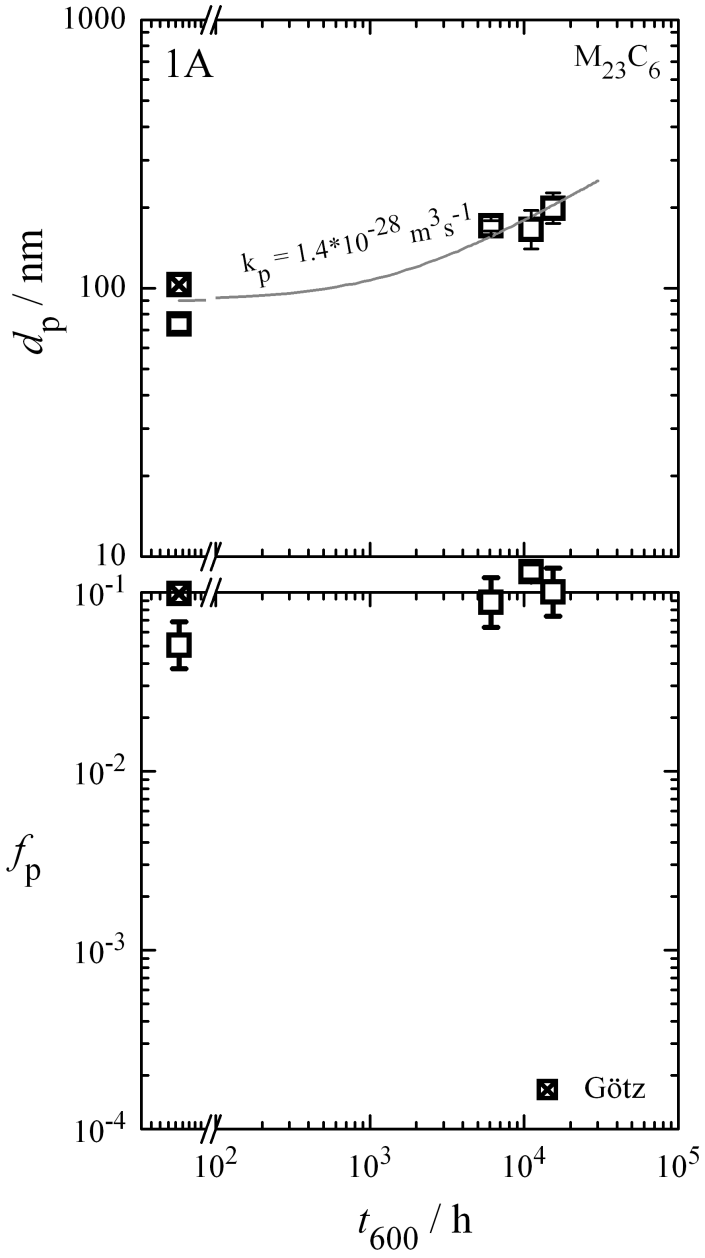

Abbildung 22: 1A $M_{23}C_6$

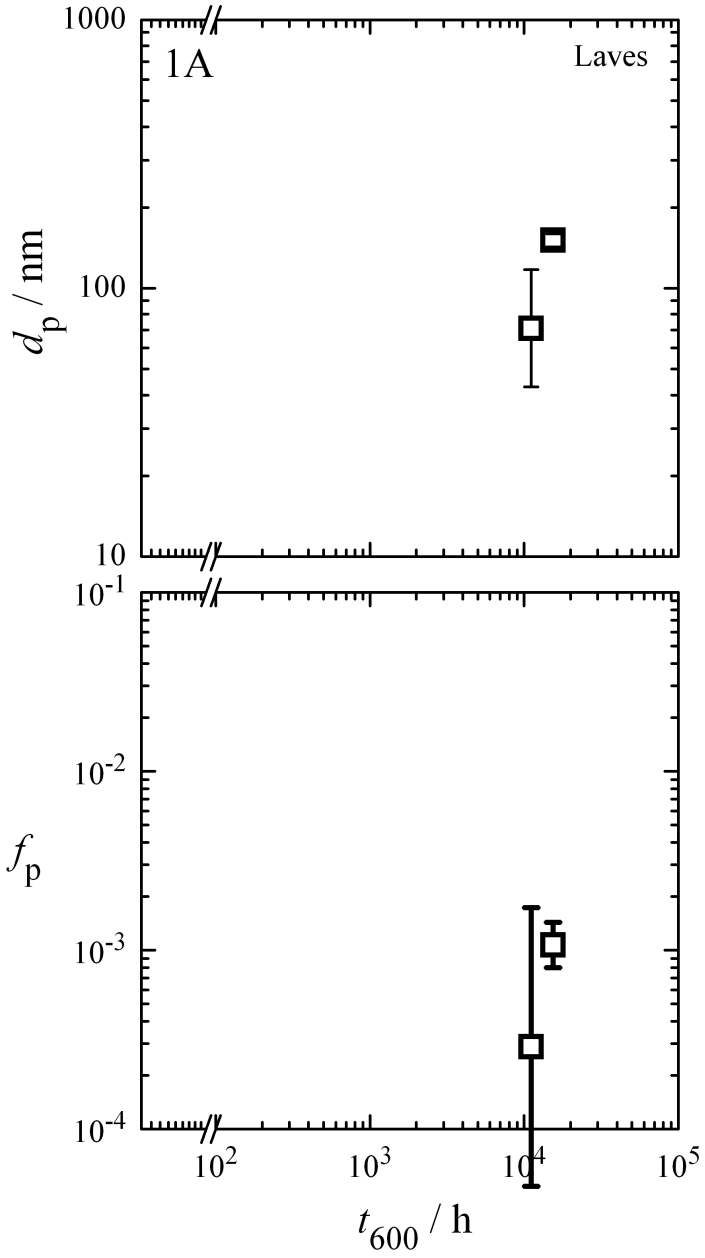

Abbildung 23: 1A Laves phase

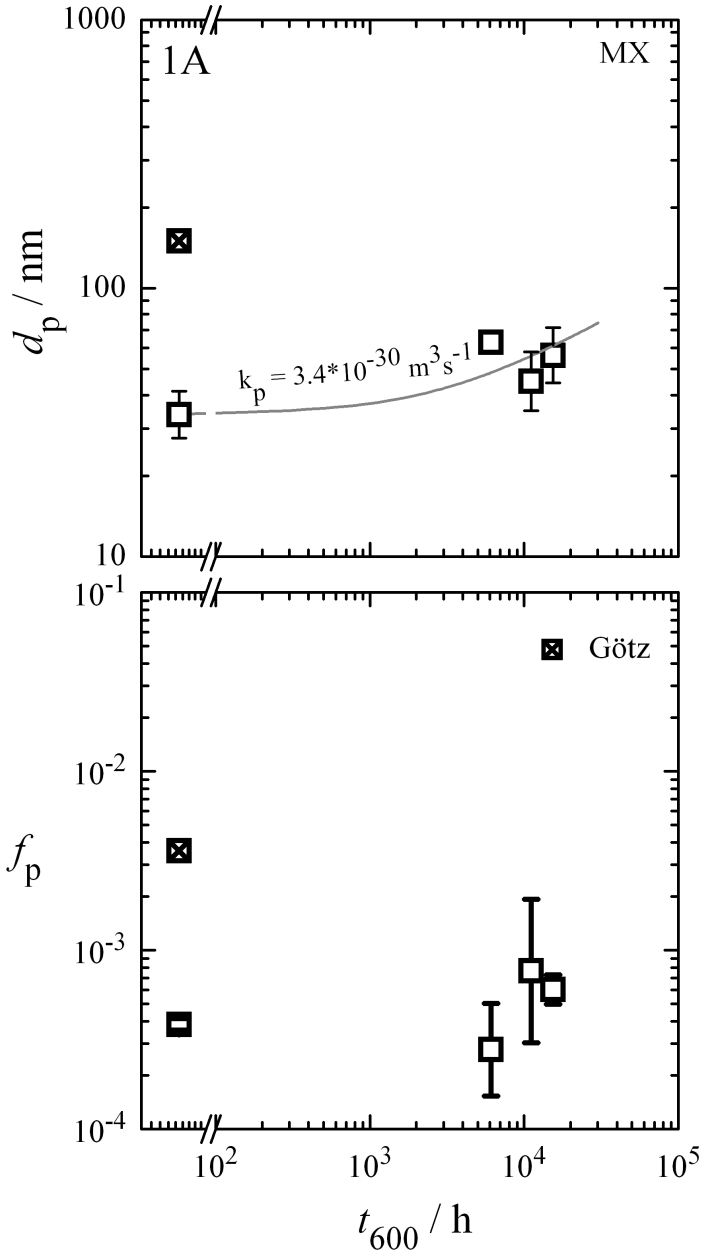

Abbildung 24: 1A MX

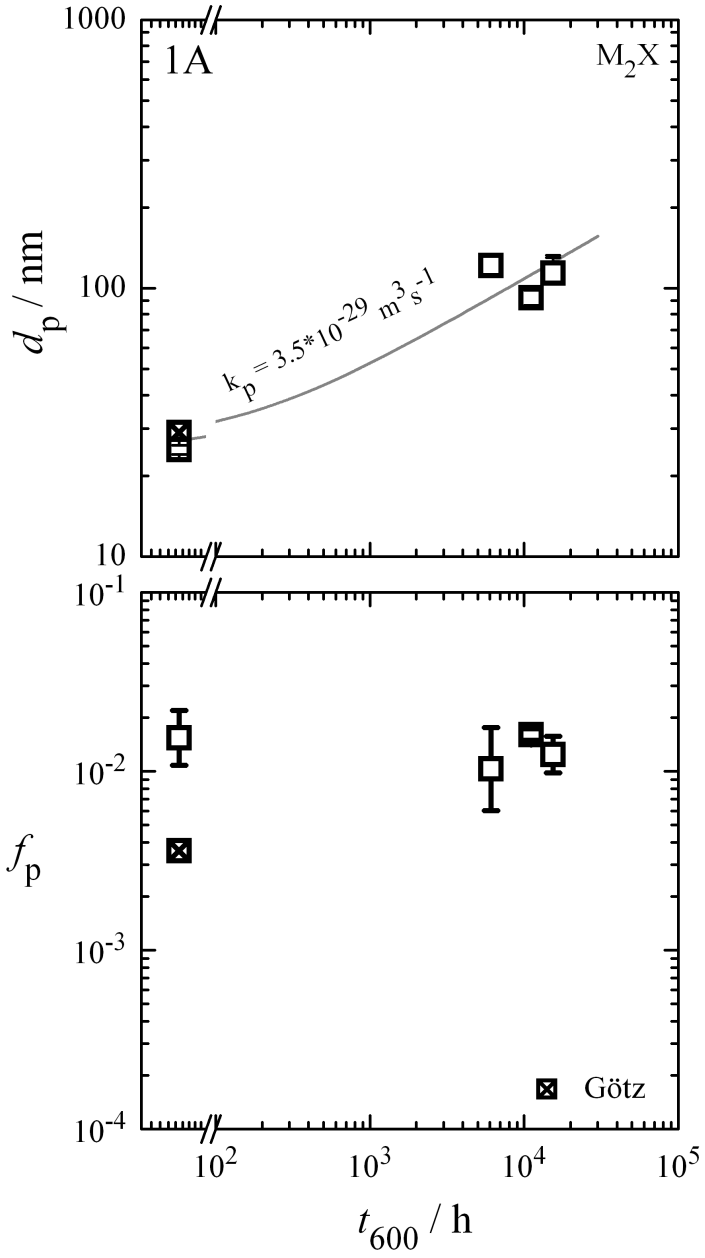

Abbildung 25: 1A M_2X

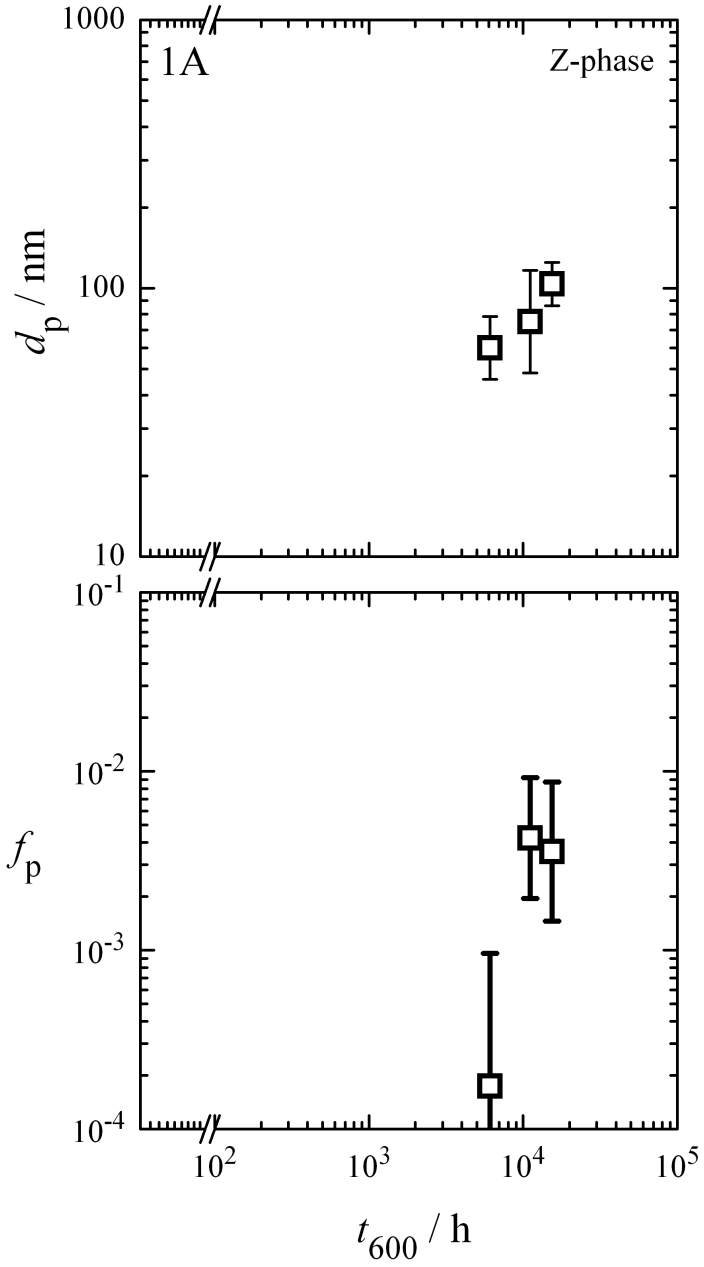

Abbildung 26: 1A Z-phase

G.3.2 3A

Precipitate structure evolution in 3A.

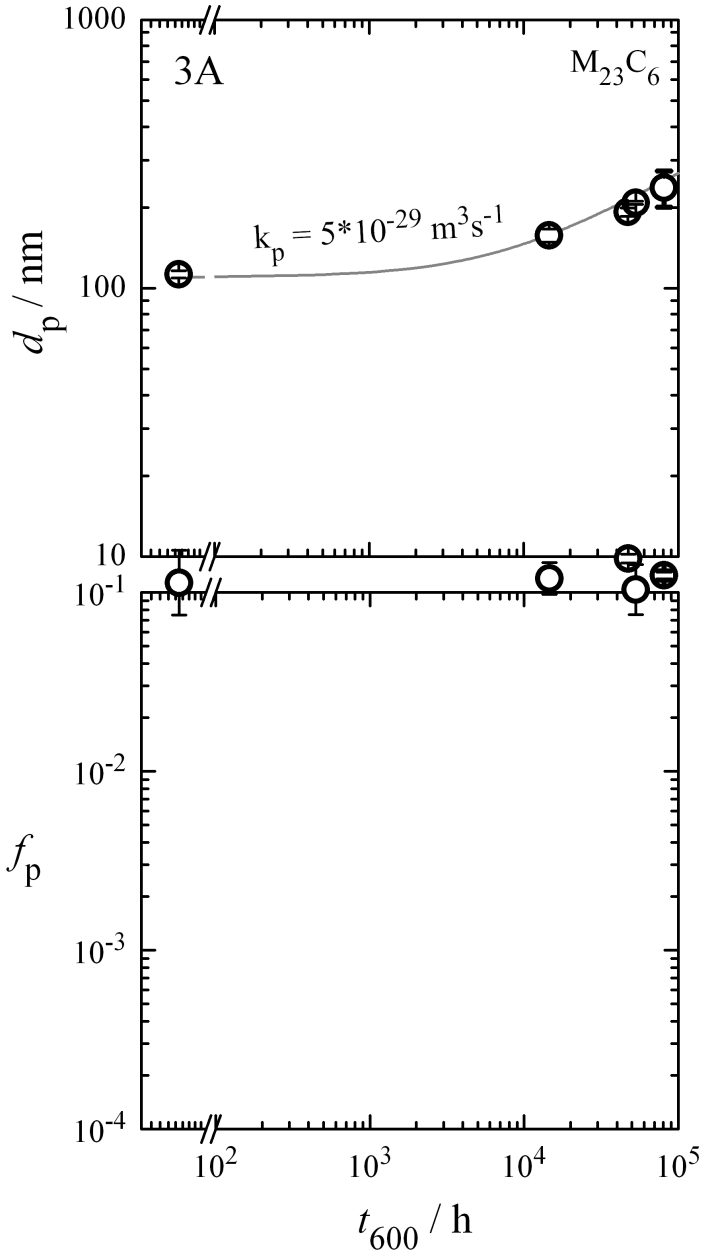

Abbildung 27: 3A $M_{23}C_6$

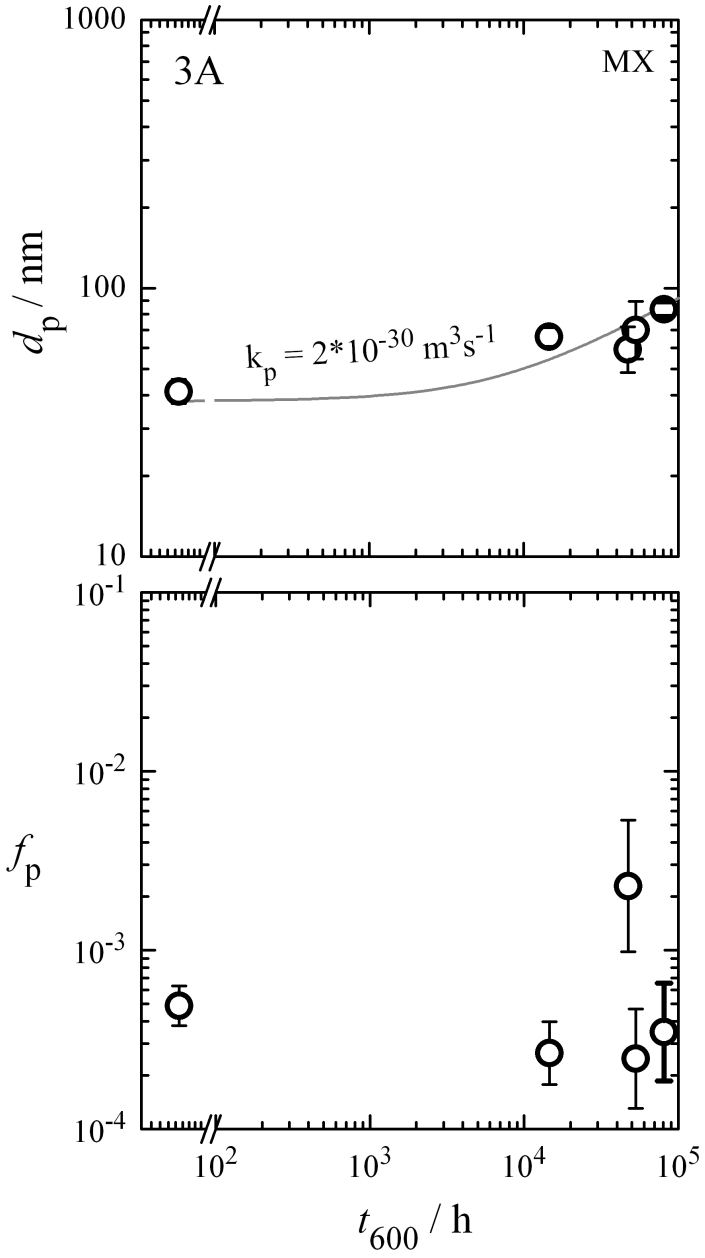

Abbildung 28: 3A MX

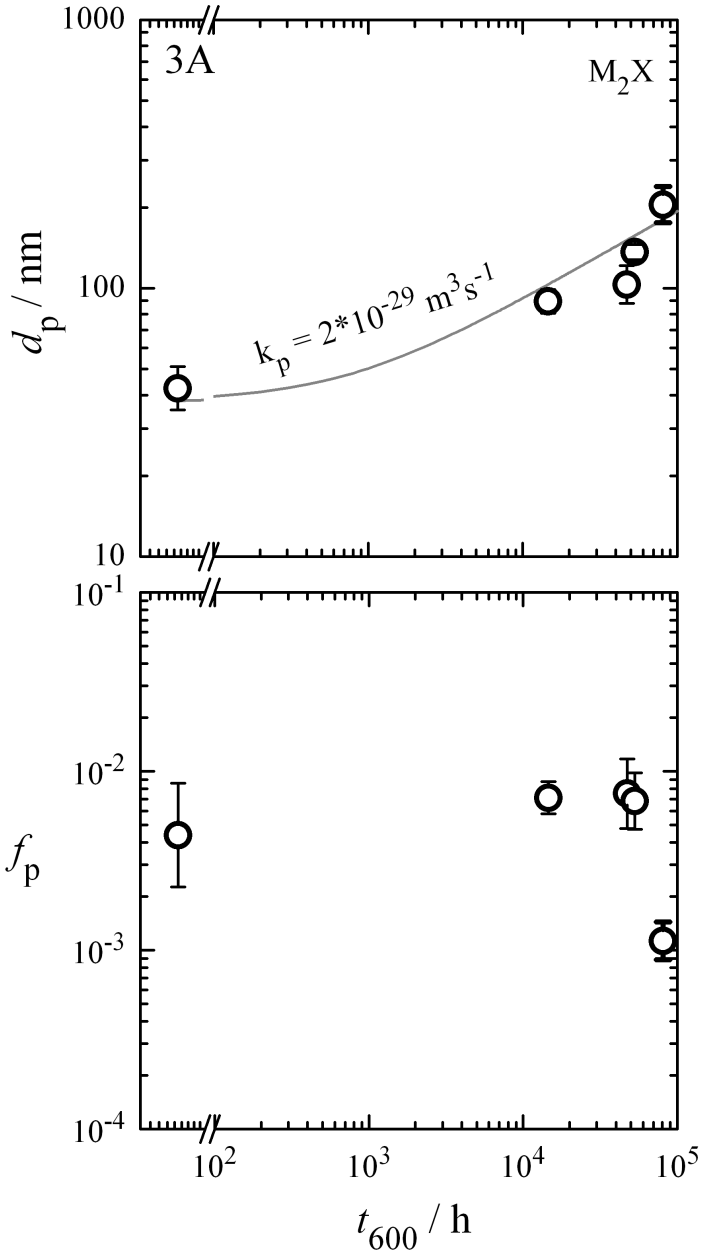

Abbildung 29: 3A M_2X

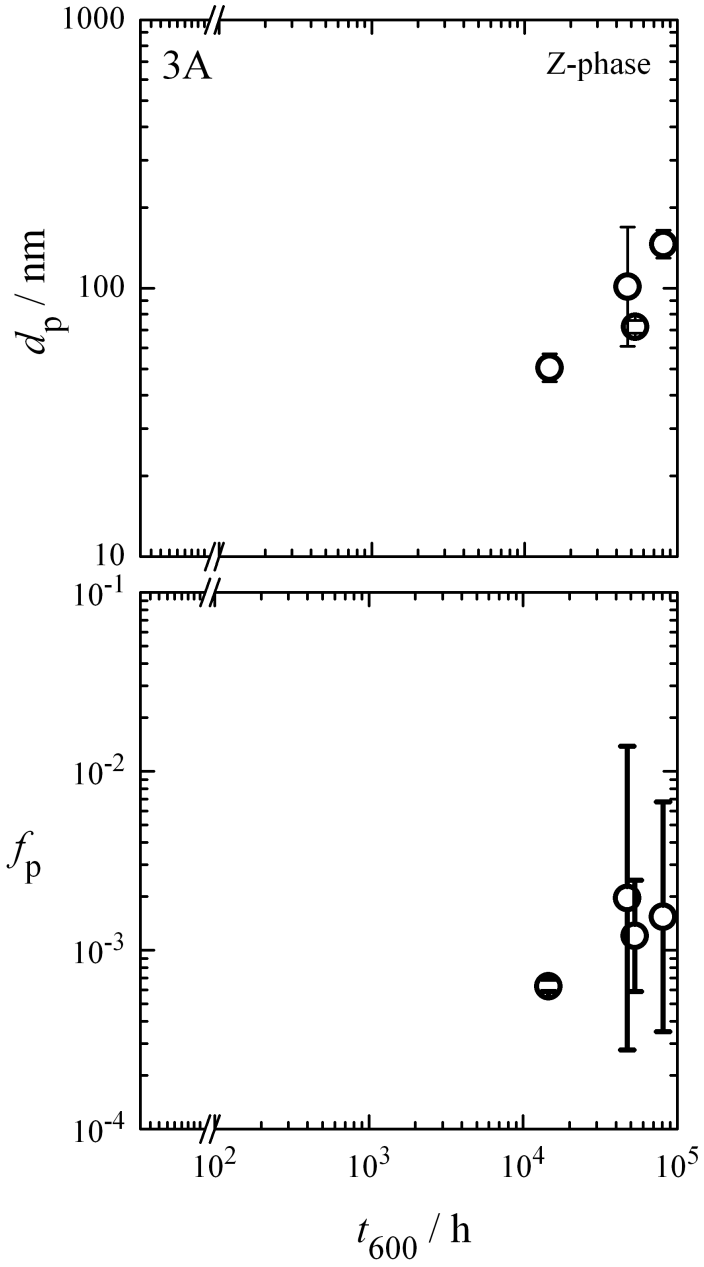

Abbildung 30: 3A Z-phase

G.3.3 4A

Precipitate structure evolution in 4A.

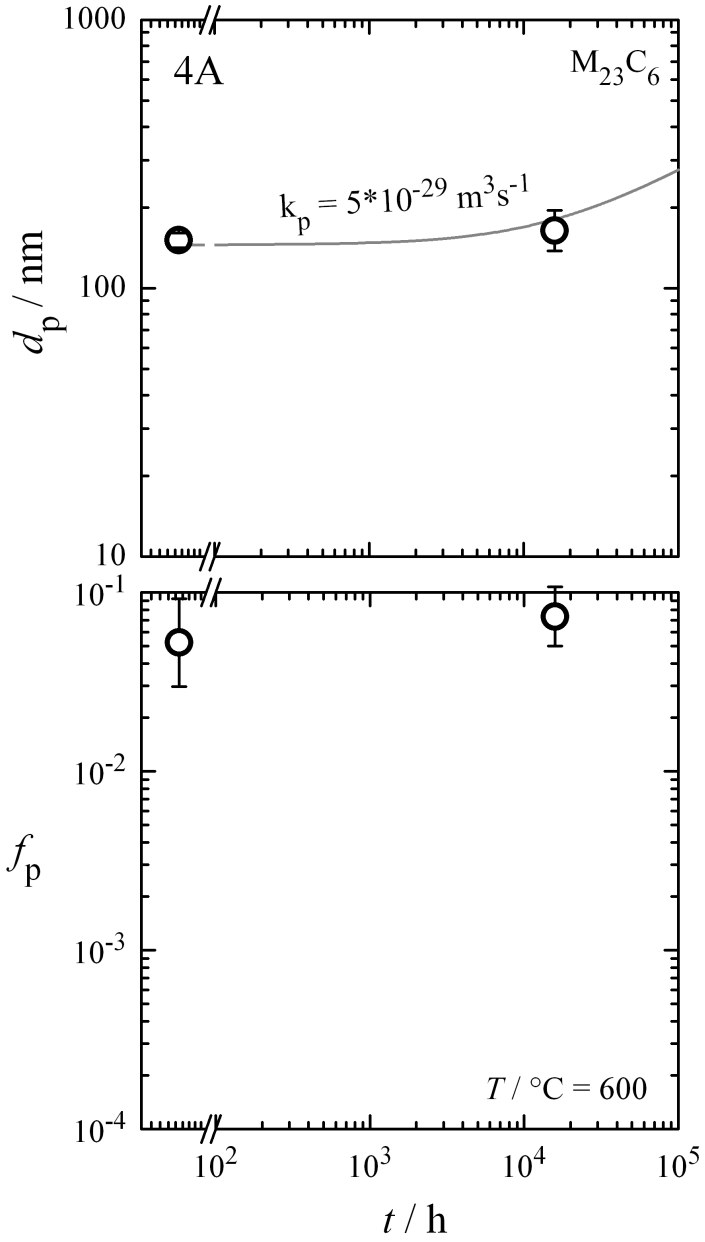

Abbildung 31: 4A $M_{23}C_6$

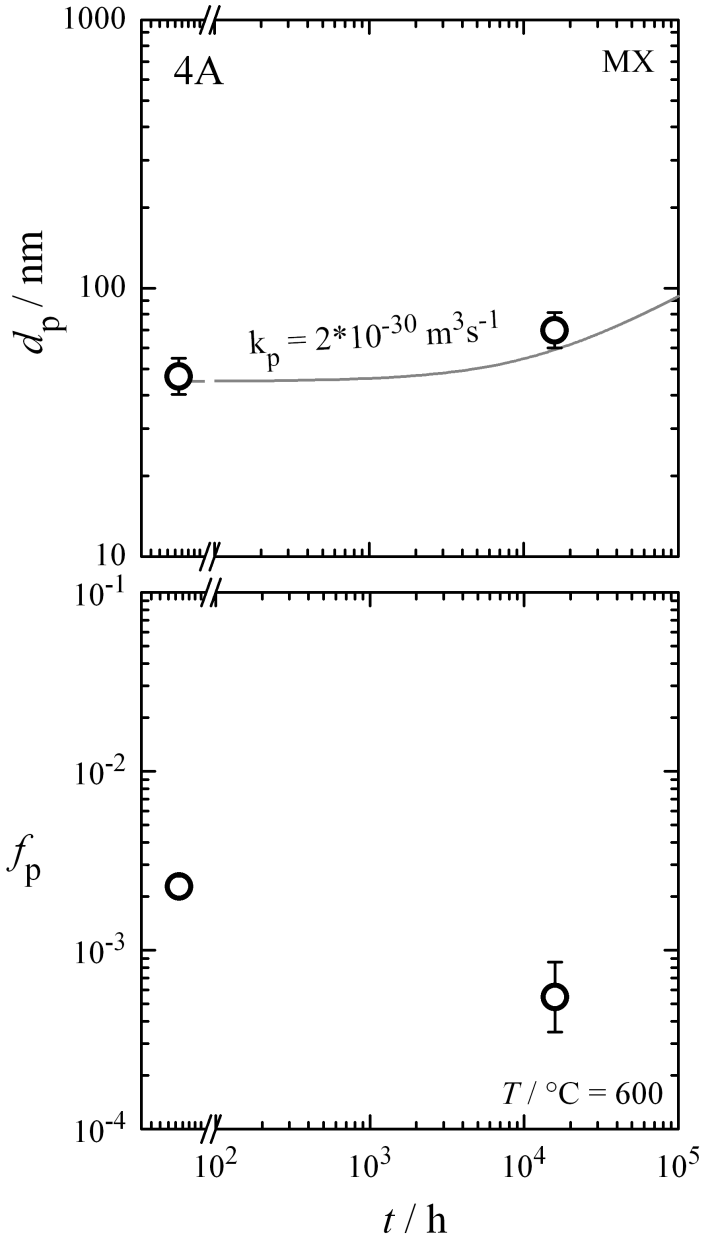

Abbildung 32: 4A MX

G.3.4 5A

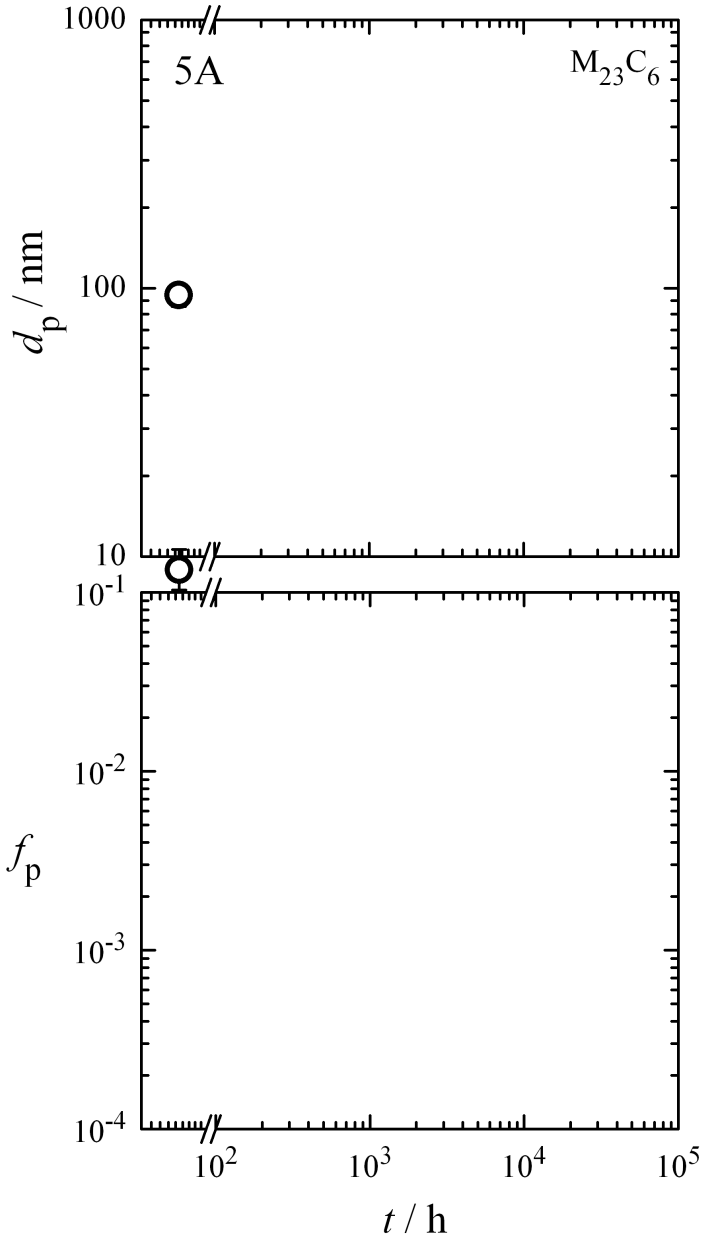

Abbildung 33: 5A $M_{23}C_6$

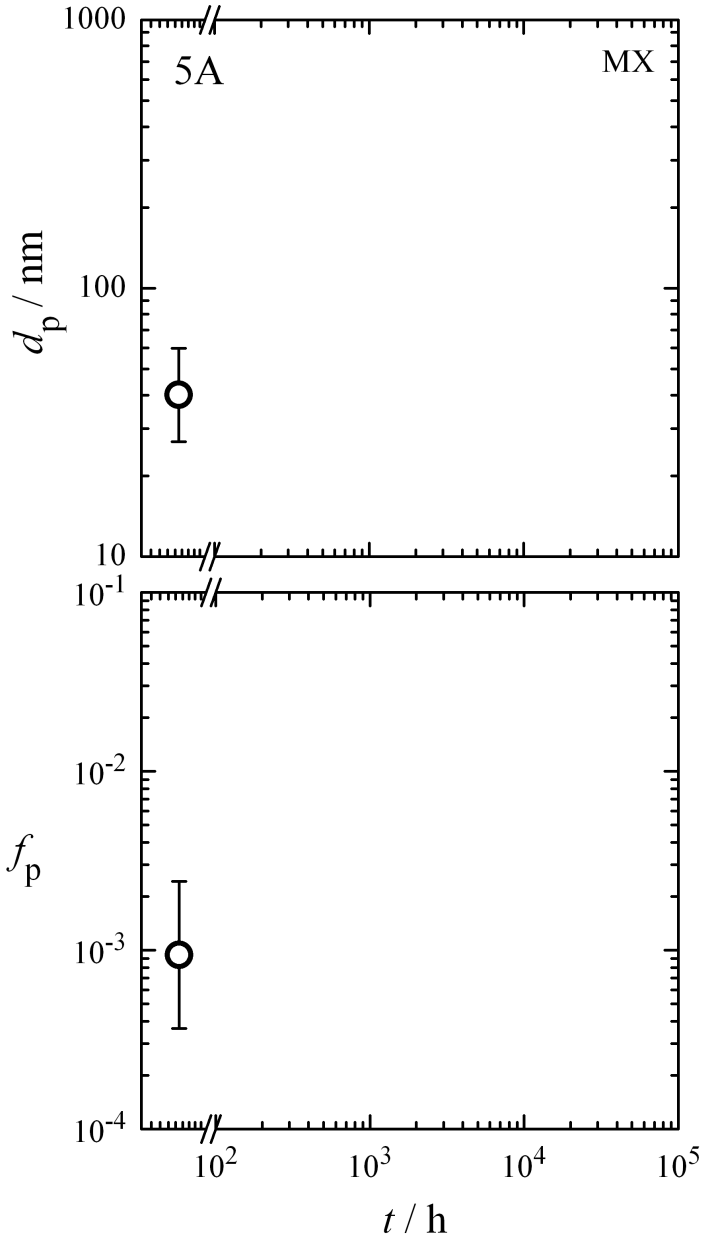

Abbildung 34: 5A MX

G.3.5 6A

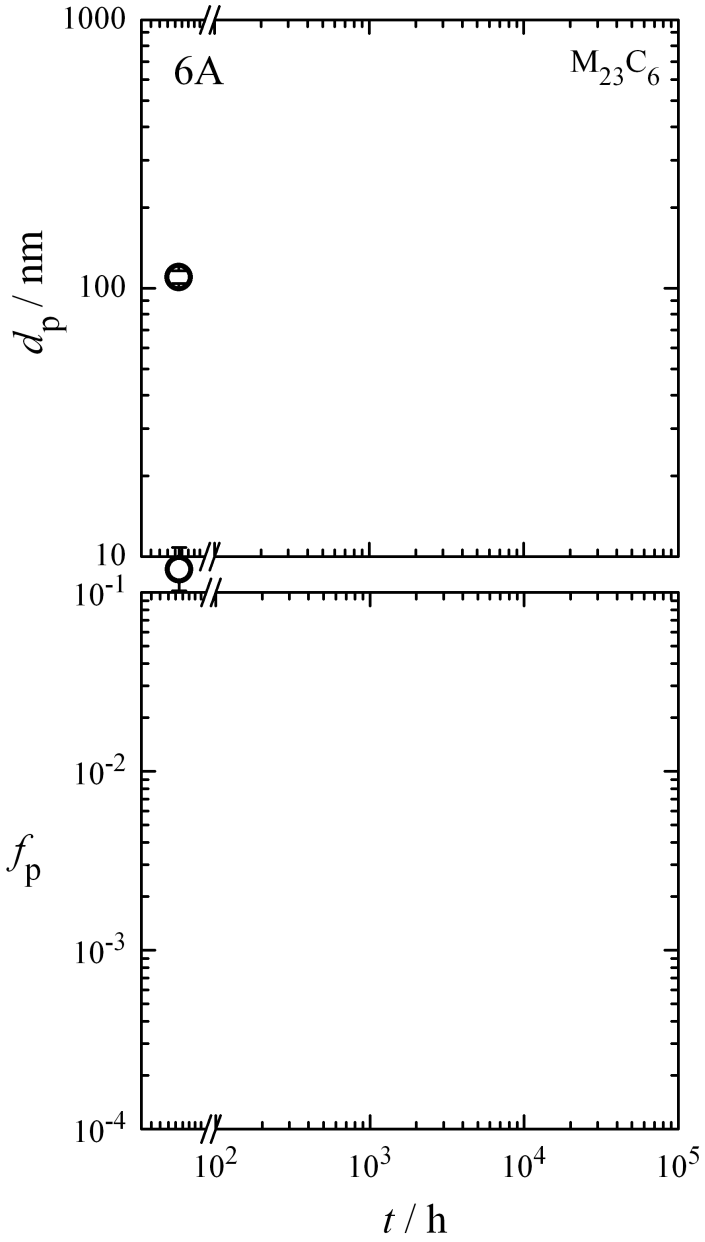

Abbildung 35: 6A $M_{23}C_6$

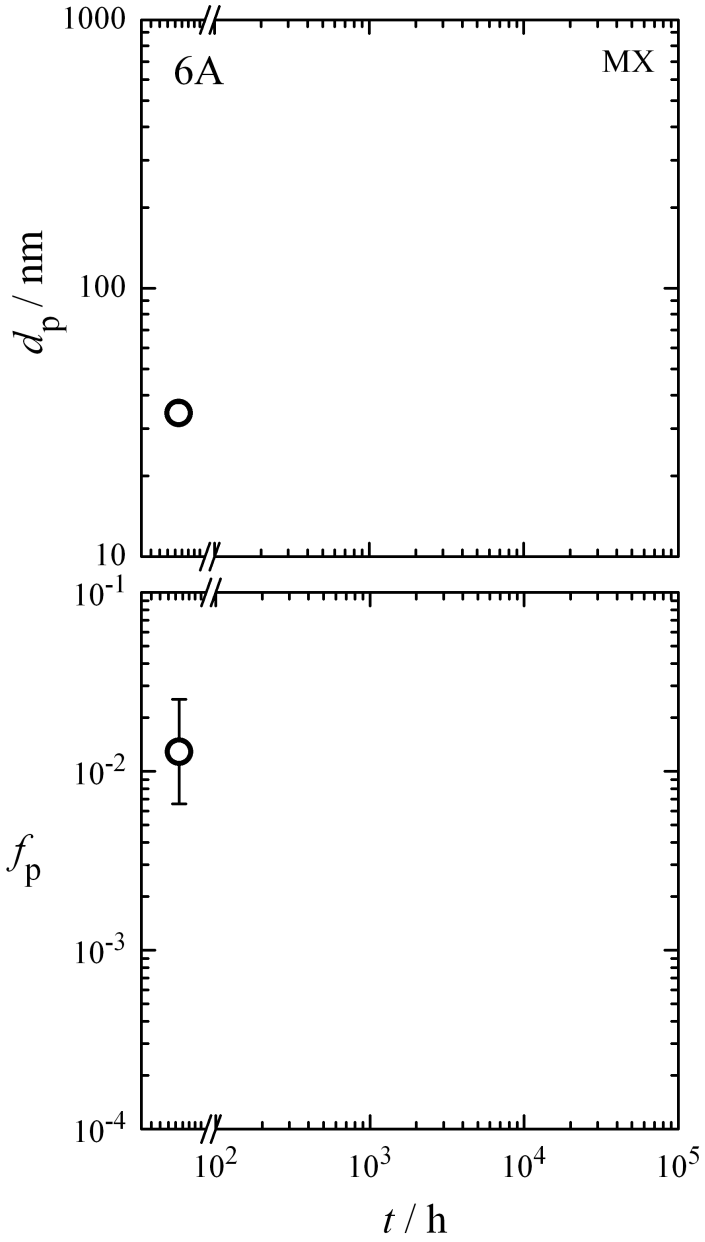

Abbildung 36: 6A MX

H Microstructural model MIKORA

Subgrain strengthening is modeled by treating the material as a composite of

- soft (s) subgrains surrounded by
- hard (h) subgrain boundaries with boundary area per volume $2/w$ and thickness a

subjected to the same mechanical strain so that the local stresses differ [21]:

$$\epsilon_{\mathrm{mech}} = \epsilon_{\mathrm{inel,s}} + \frac{\sigma_{\mathrm{s}}}{E} = \epsilon_{\mathrm{inel,h}} + \frac{\sigma_{\mathrm{h}}}{E} \tag{2}$$

$$\sigma = f_{\mathrm{s}}\,\sigma_{\mathrm{s}} + f_{\mathrm{h}}\,\sigma_{\mathrm{h}}, \qquad f_{\mathrm{s}} = 1 - f_{\mathrm{h}}, \qquad f_{\mathrm{h}} = \frac{2a}{w} \tag{3}$$

The local rate of deformation results from free dislocations of density ρ_{f} moving at velocity v under the action of the thermal stress component (difference between local stress and local athermal stress component):

$$\frac{d\epsilon_{\mathrm{inel}}}{dt} = \frac{b}{M}\,\rho_{\mathrm{f}}\,v \tag{4}$$

$$v_{\mathrm{s}} = A_{\mathrm{s}}\,\exp\left[-\frac{Q_{\mathrm{s}}}{R\,T}\right]\,\sigma_{\mathrm{s}}^{\star}\,\exp((\beta\,\sigma_{\mathrm{s}}^{\star})^{\xi}) \tag{5}$$

$$\sigma_{\mathrm{s}}^{\star} = \sigma_{\mathrm{s}} - \alpha\,M\,b\,G\,\rho_{\mathrm{f}}^{0.5} - C_{\mathrm{p,s}}\,\sigma_{\mathrm{Or,s}} \tag{6}$$

$$\sigma_{\mathrm{Or,s}} = 3.32\,G\,b\,\left(\frac{f_{\mathrm{MX}}^{0.5}}{d_{\mathrm{MX}}} + \frac{f_{\mathrm{M_2X}}^{0.5}}{d_{\mathrm{M_2X}}}\right) \tag{7}$$

$$v_{\mathrm{h}} = A_{\mathrm{h}}\exp\left[-\frac{Q_{\mathrm{h}}}{R\,T}\right]\,\sinh\left(\frac{b^2\,s\,(\sigma_{\mathrm{h}} - \sigma_{\mathrm{p,h}})}{M\,k_{\mathrm{B}}\,T}\right) \tag{8}$$

$$\sigma_{\mathrm{p,h}} = k_1\,\frac{w}{b}\,\left(\frac{f_{\mathrm{M_{23}C_6}}}{d_{\mathrm{M_{23}C_6}}^2} + \frac{f_{\mathrm{Laves}}}{d_{\mathrm{Laves}}^2}\right) \tag{9}$$

f_j is volume fraction and d_j is size of precipitates j. The dislocation interaction parameter α evolves with strain from 0 to 0.25:

$$\frac{d\alpha}{d\epsilon_{\mathrm{inel,s}}} = \frac{0.25 - \alpha}{(b/M)\,\rho_{\mathrm{f}}^{0.5}}, \qquad \alpha = 0 \;\text{ for }\; \epsilon_{\mathrm{inel}} = 0 \tag{10}$$

$C_{\mathrm{p,s}} \leq 1$ is an empirical factor taking into account that the particle strengthening term falls below the Orowan stress $\sigma_{\mathrm{s,Or}}$ due to climb over particles and ensuring $\sigma_{\mathrm{s}}^{\star} > 0$ even for small σ. It was formulated as [22]:

$$C_{\mathrm{p,s}} = \begin{cases} 1 & \sigma_{\mathrm{s}} \geq \sigma_{\mathrm{c}} \\ (1 - \exp(-(\frac{\sigma_{\mathrm{s}}}{0.2\,\sigma_{\mathrm{c}}})^{c_1}))^{1/c_1} & \sigma_{\mathrm{s}} < \sigma_{\mathrm{c}} \end{cases} \tag{11}$$

$$\sigma_{\rm c} = k_2\,[\sigma_{\rm Or,s} + |\sigma_{\rm s} - (k_3\,\sigma_{\rm Or,s})^{c_0}| + (k_3\,\sigma_{\rm Or,s})^{c_0}] \quad (12)$$

$$c_0 = k_4\,[\tanh(k_5\,(\sigma_{\rm Or,s} - k_6))] + k_7 \quad (13)$$

$$c_1 = \begin{cases} 0.2\,\sigma_{\rm Or,s}/\,{\rm MPa} & \sigma_{\rm Or,s} < 50\,{\rm MPa} \\ 10 & \sigma_{\rm Or,s} \geq 50\,{\rm MPa} \end{cases} \quad (14)$$

The characteristic spacings $x = w$, $\rho_{\rm f}^{-0.5} \equiv \delta$, a, s of the dislocation structure evolve from their starting values x_0 towards their steady state values x_∞ with strain at the rate:

$$\frac{d\log x}{d\epsilon_{\rm inel}} = -\frac{\log x - \log x_\infty}{k_x} \quad (15)$$

$$w_\infty = 2.56 \cdot \delta_\infty = 10\,b\,G/\sigma \quad (16)$$

$$s_\infty = 7.6\,{\rm nm} \quad (17)$$

$$f_{\rm h,\infty} = 0.05 \quad (18)$$

$$a_0 = a_\infty = w\,f_{\rm h,\infty}/2 \quad (19)$$

The precipitate parameters evolve with time t from their initial values as:

$$d_{\rm p} = (d_{\rm p,0}^3 + k_{\rm p} \cdot t)^{\frac{1}{3}}, \quad \text{all phases} \quad (20)$$

$$f_{\rm p} = f_{\rm p,0} \quad \text{where p is } M_{23}C_6,\ MX,\ M_2X. \quad (21)$$

$$\frac{f_{\rm Laves} - f_{\rm Laves,0}}{f_{\rm Laves,\infty} - f_{\rm Laves,0}} = 1 - \exp\left(-3.728 \cdot 10^{-3}\ \cdot (t/{\rm s})^{1.5}\right) \quad (22)$$

The starting values of the microstructural parameters serve as serve as input to the model: w_0, $f_{\rm p,0}$ and $d_{\rm p,0}$; δ_0 was set $= 100$ nm [23].

The following constants were used: length of Burgers vector $b = 0.248$ nm, Taylor factor $M = 3$, Young's modulus $E = 165\,{\rm GPa}$, $A_{\rm s} = 3.59 \cdot 10^{15}\,{\rm m\,s^{-1}\,Pa^{-1}}$, $Q_{\rm s} = Q_{\rm h} = 562\,{\rm kJ\,mol^{-1}}$, $A_{\rm h} = 4.39 \cdot 10^{20}\,{\rm m\,s^{-1}}$, $\beta = 0.043\,{\rm MPa^{-1}}$, $\xi = 1.55$ for $\sigma_{\rm s}^\star < 62\,{\rm MPa}$ and $\beta = 0.482\,{\rm MPa^{-1}}$, $\xi = 0.45$ for $\sigma_{\rm s}^\star \geq 62\,{\rm MPa}$, elastic shear modulus $G = 62\,{\rm GPa}$, $k_w = 0.12$, $k_\delta = 0.0005$, $k_a = 0.003$, $k_s = 0.03$, $k_{M_{23}C_6} = 2 \cdot 10^{-28}\,{\rm m^3 s^{-1}}$, $k_{\rm MX} = 4 \cdot 10^{-30}\,{\rm m^3 s^{-1}}$, $k_{M_2X} = 7 \cdot 10^{-29}\,{\rm m^3 s^{-1}}$, $k_{\rm Laves} = 8 \cdot 10^{-28}\,{\rm m^3 s^{-1}}$, $k_1 = 7.7\,{\rm nN}$, $k_2 = 2.4$, $k_3 = 13000\ {\rm MPa^{-1}}$, $k_4 = -0.007$, $k_5 = 0.2$, $k_6 = 107.5\ {\rm MPa^{-1}}$, $k_7 = 0.357$.